DESIGN OF DISPERSION MANAGED SOLITON SYSTEMS

KWAN YUK HA

M. PHIL.

THE HONG KONG POLYTECHNIC UNIVERSITY

2001

Abstract of thesis entitled "Design of Dispersion Managed Soliton Systems" submitted by Kwan Yuk Ha for the degree of Master of Philosophy at the Hong Kong Polytechnic University in July 2000.

One of the factors that limits the maximum transmission rate of an optical fiber communication system is chromatic dispersion. Methods to curtail the pulse broadening effects of dispersion includes propagation at the zero dispersion wavelength, dispersion management, NRZ transmission format, and soliton transmission format. In 1999, a combination of dispersion management, NRZ format, specially made fibers, and wavelength division multiplexing pushed the aggregate bit rate past the 1 tera bits per second mark for error free transmission of 7,300 km [1]. Dispersion management is carried out by concatenation of fiber segments with different dispersion coefficients alternately. The local dispersion is chosen to be large to prevent coupling between the optical signals and the amplifier noises. The average dispersion is kept low to minimize the dispersion effects. The simplest configuration of a dispersion managed system is made of two types of fibers; one with constant anomalous dispersion coefficient and the other with constant normal dispersion coefficient.

Soliton transmission format makes use of the intrinsic Kerr effect of an optical fiber to counter the dispersion effect. Distortionless propagation is possible for some specially shaped pulses if effects such as dissipation and higher order dispersion are neglected. Conventional wisdom has it that soliton transmission systems require fibers with constant anomalous dispersion. However, it was recently discovered that soliton propagation is possible even in dispersion managed systems. These so-called dispersion managed (DM) solitons have a number of advantages over the solitons of constant anomalous dispersion systems. One of the which is energy enhancement, *i.e.,* the energy of a DM soliton is higher than that of a conventional soliton with the same average dispersion and pulse width. Energy enhancement depends on the pulse width as well as the fiber segment lengths and dispersion coefficients of the dispersion map. An empirical formula was obtained for two-step dispersion maps with equal length fibers. In this thesis, we study the effect of the proportion of normal dispersion fiber on energy enhancement in a two-step dispersion map. We find that if the average dispersion is anomalous and the map strength is less than 3, energy enhancement is not affected by the length of the normal dispersion segment. If the map strength is larger than 3, we find that a dispersion map that is made of normal dispersion fibers and a fiber Bragg grating has the maximum energy enhancement. On the other hand, a dispersion map that is made of anomalous dispersion fibers and a FBG has the minimum energy enhancement. The ratio of maximum to minimum energy enhancement can be as large as 2 as the map strength increases. Qualitatively similar results are obtained for zero average dispersion and normal average dispersion systems.

Acknowledgments

I would like to give my special thanks to Dr. P. K. A. Wai, my supervisor, for providing fruitful advice, invaluable discussion, and encouragement.

I wish to thank Dr. W. S. Man for giving valuable discussion on fiber Bragg gratings and sharing his extensive knowledge of the nature and the manufacturing of fiber Bragg gratings.

Thanks also to the staff of the Department of Electronic and Information Engineering, especially Mr. Y. K. Tsang, Dr. C. Y. Li and Mr. Y. M. Wong, for helping me to set up the computer facilities.

I want to thank my family for their solid support and understanding in the period of my study.

Statement of Originality

The following contributions reported in this thesis are claimed to be original.

1 The dependence of dispersion managed soliton energy and pulse width on the proportion of normal dispersion fibers in two-step dispersion maps for average anomalous, average zero, and average normal dispersion systems.

2 The map configurations for the maximum and minimum soliton energy. The pulse width, map length, average dispersion coefficient, and cumulated absolute dispersion are held constant.

Contents

List of Figures

Chapter 1

Dispersion and Nonlinearity

1.1 Introduction

Nowadays, it is a cliché to describe the world as a global village. Advances in telecommunication technology have indeed brought the world closer together, both for individuals and businesses. The author personally has benefited greatly from instant access to the electronic databases on publications in optical communication areas during this thesis work. International corporations rely on telephones, faxes, and e-mails, to ensure that their manufacturing plants and sale offices located thousands miles apart can operate as one. Transoceanic communication systems play an important role in the global networks. In the past, submarine communication systems are slow to adopt new technologies because of the stringent reliability requirements. The mean time to failure is twenty five years for all the components that go into such systems. However, the ever increasing demand for higher transmission capacity and the independence of new systems from installed systems have turned submarine systems into one of the most aggressive in the development and adoption of new technologies.

In 1999, the aggregate bit rate in transoceanic optical communication systems has reached the 1 tera bits per second mark [1]. The achievement is the cumulation of research and development efforts in optical fiber technologies in the last three decades. The main factors limiting the maximum transmission capacity of an optical fiber are the optical gain bandwidth, dispersions, and nonlinear effects. The available gain bandwidth limits the maximum signal bandwidth. Dispersion spreads the optical signals in the time domain [2] and limits the per channel bit rate. Nonlinearity spreads the optical signals in the spectral domain [2] resulting in a decrease in the signal-to-noise ratio. To maintain gain flatness and increase the gain bandwidth is the work of material engineering. The impact of various nonlinearity effects can be alleviated by simply reducing the signal energy. Dispersion effects include polarization mode dispersion [3] and chromatic dispersion [2]. Polarization mode dispersion is the result of the random coupling between the two polarization states of an optical signal [3]. Intensive work are being carried out in this area [4, 5, 6, 7]. There are many methods to control the deleterious effect of chromatic dispersion. The most successful one is dispersion management [3] which consists of concatenating fiber segments with large dispersion coefficients of the opposite signs such that the average dispersion is small to reduce the dispersion effects and the local dispersion is large to reduce the four waves mixing effects [3]. Another ingenious way to control the effect of chromatic dispersion is to use solitons [2]; specially shaped pulses in which the intrinsic Kerr nonlinearity of the optical fibers balances the second order chromatic dispersion. Much work have been carried out since the inception of the idea in 1973 [8]. Recently, it was discovered that solitons can also propagate in dispersion managed systems [9, 10, 11, 12]. These so called dispersion managed solitons have a number of advantages over conventional solitons in which the dispersion coefficient is constant. One of the advantages is called energy enhancement [9], *i.e.*, the energy required to launch a soliton in a dispersion managed (DM) system is higher than that of a conventional soliton system with the same average dispersion and pulse width. The characteristics of dispersion managed solitons depend on the details of the dispersion map used. In this thesis, we study how the energy enhancement [11, 13, 14, 15] varies with the ratio of the length of the normal fiber segment to that of the anomalous fiber segment in a two-step dispersion map. We find that for the same average dispersion and the map strength [11], the energy enhancement is maximum when the length of the anomalous fiber segment is zero and minimum when the length of the normal fiber segment is zero. In the cases of zero length segment, dispersion compensations are carried out by chirped fiber gratings [16, 17, 18, 19]. We then show that similar to the DM systems using dispersion compensating fibers [20, 21], DM systems using fiber Bragg gratings have solitons for zero and normal average dispersion.

In Chapter 1, we study the effect of dispersion on signal propagation and some of the methods proposed to minimize the dispersion effects. In Chapter 2, we discuss dispersion management systems. We use the numerical averaging technique [22] proposed by J. H. B. Nijhof *et al.* to find the soliton solutions of DM systems numerically. Chapter 3 gives the background of fiber Bragg gratings. We verify that soliton can propagate in DM systems using chirped fiber gratings for dispersion compensation. In Chapter 4, we show the variation of the energy enhancement as a function of the length of the normal dispersion segment in a two-step dispersion map. We also give the energy enhancement for grating compensated DM systems having zero and normal average dispersion. We conclude the thesis in Chapter 5.

1.2 Chromatic Dispersion

Glass is a dispersive medium. Different spectral components of an input pulse will accumulate different phase values as the pulse propagates along the fiber. As a result, the pulse will in general be broadened. An initial pulse can be chirped in a such way that it will contract first, but the pulse eventually will be broadened [23]. Figure 1.1 shows the broadening of a Gaussian pulse as it propagates in a dispersive medium. The pulse shapes in the time domain are obtained by measuring the signal intensity at different point along a fiber. Negative values of time represent the past and positive values represent the future.

Chromatic dispersions, also known as group velocity dispersion (GVD), is caused by the variation of the time delay per unit length $\tau_d(\omega) = 1/v_g(\omega)$ with respect to the angular frequency ω, where v_g is the group velocity of the pulse. If the group velocity v_g does not depend on frequency, the medium is non-dispersive. Since the group velocity $v_g = d\omega/d\beta$, the GVD coefficient $\ddot{\beta} \equiv d^2\beta/\, d\omega^2$ measures the rate of change of the time delay per unit length. The propagation constant β equals $2\pi n(\omega)/\lambda$ where λ is the wavelength of pulse and n is the refractive index of fiber. The unit of GVD coefficient is $\mathrm{ps}^2/\mathrm{km}$ [23].

There is an alternate definition of the GVD coefficient $D = d(1/v_g)/\, d\lambda$ which measures the variation of the propagation delay per unit length with respect to the wavelength instead of the angular frequency. The unit of D is ps/(km-nm) [23]. The relation between the two definitions of GVD coefficients is $D = -(2\pi c/\lambda^2)\ddot{\beta}$. The difference in signs between them can lead to confusion because both are called GVD coefficients in the literature.

Positive values of $\ddot{\beta}$, *i.e.*, negative values of D, are called normal dispersion while negative values of $\ddot{\beta}$ or positive values of D are called anomalous dispersion. For standard communication grade fibers, $D = 17$ ps/(km-nm) at 1.55 μm, the wavelength of minimum loss. For dispersion-shifted fibers, $D = 0.1$ ps/(km-nm) at the same wavelength. The loss coefficient in communication fibers is about 0.2 dB/km [3].

The equation governing the evolution of the optical signal in the presence of chromatic dispersion is given by

$$i\frac{\partial q}{\partial z} - \left[\frac{\ddot{\beta}(z)}{2}\right]\frac{\partial^2 q}{\partial t^2} = 0, \tag{1.1}$$

where $q(z,t)$ is the slowly varying envelope of the electric field, z is the normalized distance, t is the normalized time, and $\ddot{\beta}(z)$ is the GVD profile along the fiber. The second term on the left hand side of Eq. (1.1) represents the effect of chromatic dispersion [2]. Eq. (1.1) is a linear partial differential equation and can be solved using the Fourier transform method. The solution of Eq. (1.1) at distance L is [Appendix A.1],

$$q(L,t) = \mathcal{F}^{-1}\{\mathcal{F}[q(0,t)]\exp[i\omega^2\int_0^L \ddot{\beta}(z)\,dz/2]\}, \tag{1.2}$$

where $\mathcal{F}[q]$ is the Fourier transform of a function q defined as

$$\mathcal{F}[q(t)] = \frac{1}{2\pi}\int_{-\infty}^{\infty} q(t)\exp(i\omega t)\,dt. \tag{1.3}$$

1.2.1 The Effect of Dispersion

In this Section, we will study the effect of dispersion analytically using an initial Gaussian pulse as an example. Let the initial pulse $q(z=0,t)$ be given by $A\exp(-t^2/2T_0^2)$ where A is the peak amplitude and $2T_0$ is the pulse width. For convenience, the pulse width for a Gaussian pulse is defined as the width between the two time points at which the pulse intensity drops to exp(−1) of its peak value [2]. We assume that the GVD coefficient $\ddot{\beta}(z)$, does not vary along the fiber.

At a distance $z = L$, the pulse width becomes [Appendix A.2]

$$\tau(z = L) = 2T_0\sqrt{1 + (\ddot{\beta}L/T_0^2)^2}. \tag{1.4}$$

From Eq. (1.4), the pulse width increases as the propagation distance increases [Appendix A.2]. For the same distance and initial pulse width, the pulse broadens faster as the GVD coefficient increases. Also a narrow initial pulse will broaden faster. Thus the straightforward way to increase the transmission rate by decreasing the pulse width has its limits.

At transmission distance $L = T_0^2/|\ddot{\beta}|$, the pulse width is broadened by a factor of $\sqrt{2}$. In general, the dispersion length L_D is defined as $L_D = \tau^2/|\ddot{\beta}|$, where τ is the initial width of the pulse and $\ddot{\beta}$ is the GVD coefficient of the fiber [2, 3]. Figure 1.1 shows the evolution of an initial Gaussian pulse at $z = 0$, $z = L_D$ and $z = 2L_D$ in time domain. The initial shape of the pulse is $\exp(-t^2/2T_0^2)$ and $T_0 = 10$ ps. From Eq. (1.2), the magnitude of the pulse spectrum is unchanged under the dispersion effect, only the phase of the pulse varies. This change in phase of the spectral components of the pulse is the cause of pulse broadening in time domain.

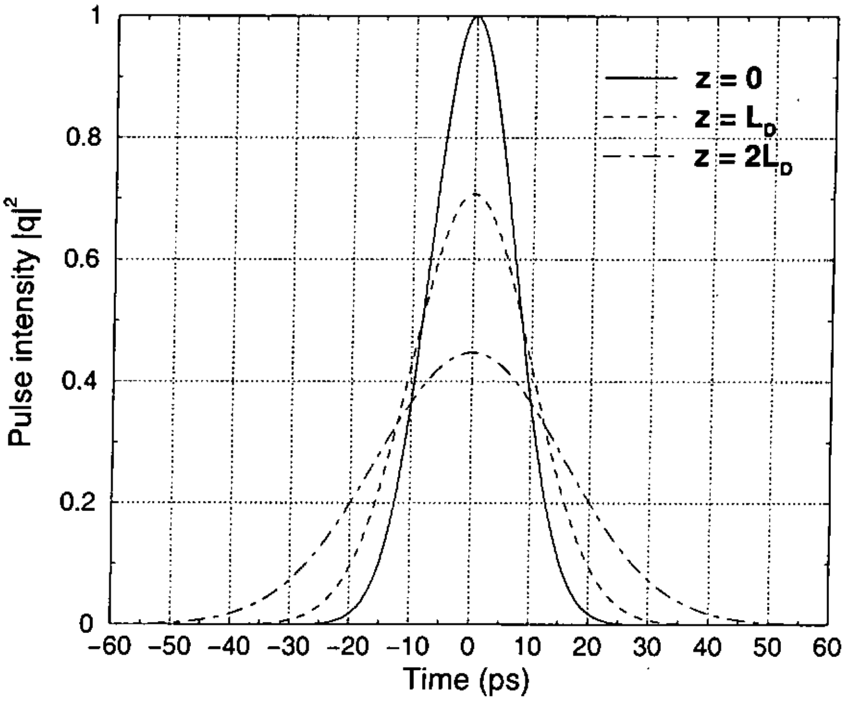

Figure 1.1: The effect of dispersion. The initial pulse shape is $\exp(-t^2/2T_0^2)$. The pulse shape at $z = 0$, $z = L_D$ and $z = 2L_D$ are represented by the solid line, dashed line, and dash-dotted line, respectively. The initial pulse width $2T_0 = 20$ ps.

1.3 Tackling Chromatic Dispersion

1.3.1 The linear way

From Eq. (1.4), the natural ways to alleviate the impact of dispersion are to either increase the initial pulse width T_0 or decrease the dispersion coefficient $\ddot{\beta}$. In the former approach, the largest available pulse width for a given bit period is the bit period itself. Therefore, in the non-return-to-zero (NRZ) transmission format, the whole bit period is filled in the case of a one. For consecutive ones, the pulse intensity will not return to zero at the boundaries of the bit period in order to diminish the dispersive effects of the rising and falling edges of the pulses. The latter approach is to propagate at the so called zero dispersion wavelength (ZDW). In pure silica, $\ddot{\beta} = 0$ at $\lambda_0 = 1.27\ \mu\text{m}$ which is the ZDW [2]. The name is a misnomer because it is only the GVD coefficient which is zero at λ_0, higher order dispersion coefficients such as $\partial^3\beta/\partial\omega^3 \neq 0$. Nevertheless, the overall dispersion effect is much smaller at λ_0. The zero dispersion wavelength depends on the oxide concentration of optical fibers [2] which may vary during the manufacturing process. Also, propagation at the zero dispersion wavelength is not compatible with wavelength division multiplexing systems because only one channel can be at the zero dispersion wavelength.

A combination of the two approaches, *i.e.*, propagation at the zero dispersion wavelength using NRZ format, promises a even higher transmission rate than either approach alone. However, due to pseudo-phase-matching between the signals and the amplified spontaneous emission (ASE) noises introduced by the erbium doped fiber amplifiers at the zero dispersion wavelength, the four-wave mixing effect introduces a large degree of

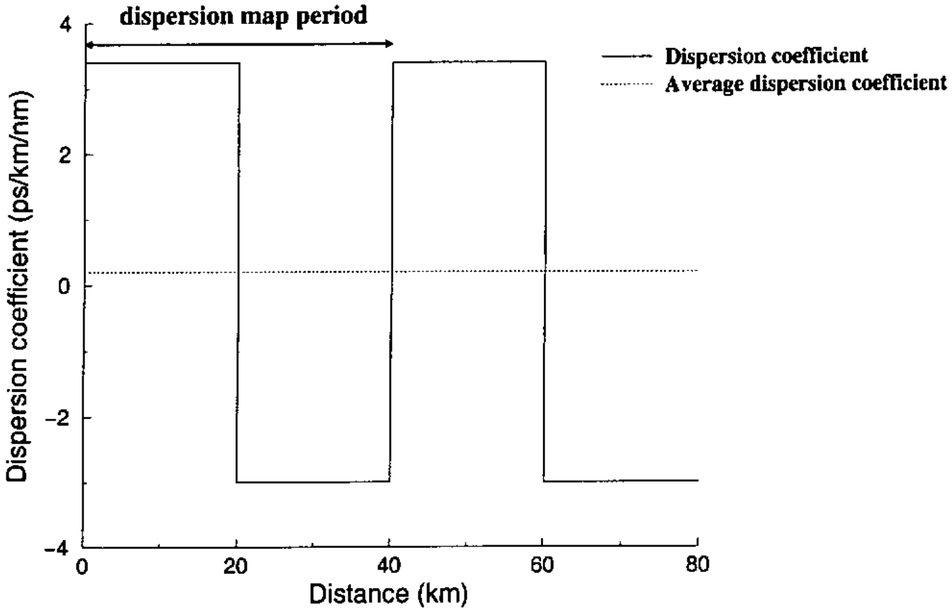

Figure 1.2: An example of dispersion map configuration. The average dispersion is 0.2 ps/(km-nm) and the length of the dispersion map is 40 km.

noise figure in such systems and limits its transmission rate [2, 3].

Another method to increase transmission distance comes from Eq. (1.2). Note that the pulse will not spread if $\int_0^L \ddot{\beta}(z)\, dz = 0$. In other words, only the cumulated dispersion at $z = L$ is important, not the detailed variation of the dispersion coefficient between $z = 0$ and L. One can therefore minimize the dispersion effect by splicing fiber segments with dispersion coefficient of opposite signs together alternately. This technique is called dispersion management [3]. The basic period of the periodically varying dispersion profile is called a dispersion map. Figure 1.2 shows a configuration of dispersion map and the map length is 40 km. The length of the two fiber segments in the map is equal, *i.e.*, 20 km. The dispersion coefficient of the first segment of fiber is 3.4 ps/(km-nm) and that of the second segment is -3 ps/(km-nm). The average dispersion coefficient of the map is 0.2 ps/(km-nm).

The large local dispersion at the fiber segments results in a large phase difference between the signals and the noises. Note that the propagation of noises is similar to that of the signals. The phase differences between the signals and noises are given by $[\ddot{\beta} z(\omega_q^2 - \omega_n^2)]/2$, where ω_q is the angular frequency of signal and ω_n is the angular frequency of the noises. By superposition, if the signals and noises has large phase difference, the coupling between the signals and noises is weak. Thus, large local dispersion avoids the phase matching condition between the signals and noises. We shall discuss dispersion managed systems in details in Chapter 2.

1.3.2 The nonlinear way

Soliton format is another method to control the effect of dispersion. A soliton is a special kind of return-to-zero (RZ). The pulse intensity of an RZ pulse rises from and returns to zero within the bit window in the case of a one. Soliton pulses make use of an intrinsic nonlinearity of fibers, the Kerr effect, to counter the pulse broadening effect of dispersion. For some special pulse shapes, the interaction of the Kerr nonlinearity and anomalous dispersion will result in distortionless propagation if other effects such as loss, higher order dispersion, *etc*, are ignored. Soliton propagation in optical fibers was first proposed by A. Hasegawa and F. D. Tapper in 1973 [8] and was observed experimentally by L. F. Mollenauer, R. H. Stolen, and J. P. Gordon in 1980 [24].

The Kerr effect describes the dependence of the refractive index $n(\omega, I)$ on the light intensity, that is,

$$n(\omega, I) = n_0(\omega) + n_2 I, \tag{1.5}$$

where $n_0(\omega)$ is the frequency dependent component of the fiber refractive index, ω is the angular frequency of light, I is the intensity of the signal, and n_2 is Kerr coefficient which is about 2.6×10^{-20} m^2/W for silica fibers [3]. The nonlinear contribution to the index of refraction results in an additional phase change in the optical signals. The phase change due to the Kerr effect is called self-phase modulation (SPM) [2]. The equation describing light propagation under the influence of SPM alone is given by

$$i\frac{\partial q}{\partial z} + |q|^2 q = 0, \tag{1.6}$$

where q is the normalized electric field of the signal and z is the normalized transmission distance. The second term on left hand side represents the effect of SPM. The solution of Eq. (1.6) after traveling distance L is [Appendix A.4],

$$q(L,t) = q(0,t)\exp(i|q(0,t)|^2 L). \tag{1.7}$$

The effect of SPM is therefore an intensity dependent phase change. In the following, we will describe how the combination of this nonlinear phase change with the "right" type of dispersion will result in distortionless transmission. The additional phase change due to Kerr effect is $\Delta\phi = 2\pi n_2 z I/\lambda$, where λ is the wavelength of the light [2]. Therefore, the instantaneous angular frequency $\Delta\omega = -\partial(\Delta\phi)/\partial t$ is proportional to $-dI/dt$. This shift of angular frequency will lead to a change in the group velocities of different frequency components of the signal [2]. The change in group velocity will depend on the sign of the dispersion coefficient of the optical fiber. From Section 1.2, $\ddot{\beta} = -(1/v_g^2)(dv_g/d\omega)$ [Appendix A.3]. If $\ddot{\beta} < 0$, the group velocity will increase as the angular frequency increases. The effect of SPM in an anomalous dispersion system on the pulse shape is shown in Figure 1.3. The top diagram gives the pulse intensity in time domain. The middle diagram gives the change in the instantenous frequency of the pulse due to the

Kerr nonlinearity. The bottom diagram is the resulting pulse under the combined effects of nonlinearity and anomalous dispersion. In the middle diagram of Figure 1.3, the instantenous frequency in the front part of the pulse decreases while that at the rear part of the pulse increases. As a result, the front part of the pulse slows down while the rear part speeds up, so that the pulse is compressed. For some special pulse shapes, the pulse broadening effects of anomalous dispersion and the compression effect of anomalous dispersion plus Kerr nonlinearity can be balanced resulting in solitons.

1.4 The Nonlinear Schrödinger Equation

The equation governing the evolution of the slowly varying envelope of an optical pulse including the effect of dispersion and Kerr effect is given by

$$i\frac{\partial q}{\partial z} - \left[\frac{\ddot{\beta}(z)}{2}\right]\frac{\partial^2 q}{\partial t^2} + |q|^2 q = 0, \tag{1.8}$$

where $q(z,t)$ is the slowly varying envelope of the electric field, z is the normalized distance, t is the normalized time, and $\ddot{\beta}(z)$ is the normalized group velocity dispersion coefficient. The second term on the left hand side of Eq. (1.8) represents the effect of chromatic dispersion while the third term on the left hand side represents the effect of self-phase modulation (SPM) [2]. In general, the dispersion coefficient is a function of transmission distance. Effects such as loss and higher order dispersion are not included in Eq (1.8). We solve Eq. (1.8) as an initial value problem, *i.e.*, given the initial pulse shape $q(z=0,t) = \psi(t)$, we want to find the pulse shape at $z = L$, *i.e.*, $q(z = L, t)$.

If the dispersion coefficient is constant, Eq. (1.8) is known as the nonlinear Schrödinger (NLS) equation which is shown to be completely integrabled by the inverse scattering

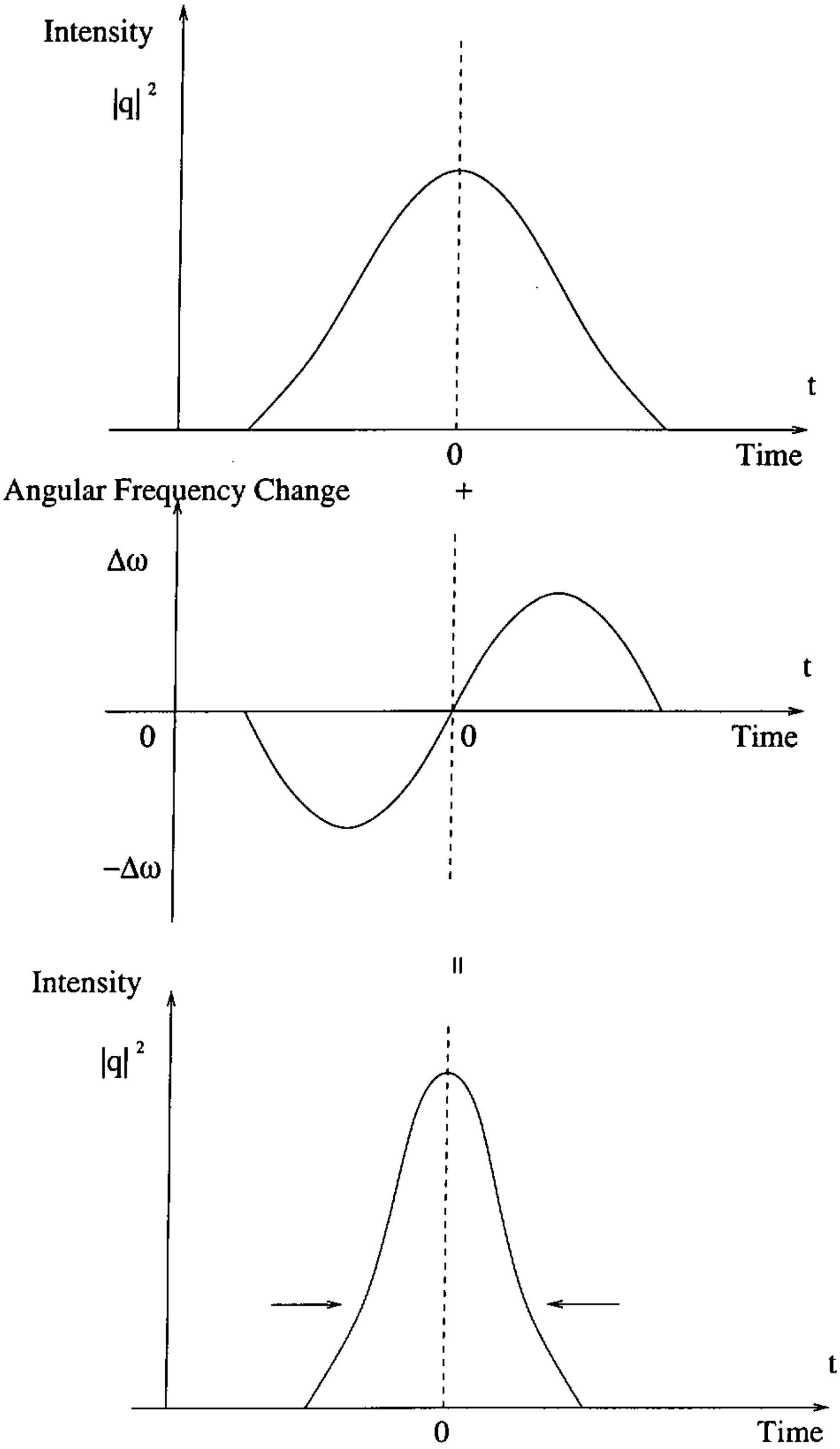

Figure 1.3: Pulse compression due to the combine effects of self-phase modulation and anomalous dispersion.

transform (IST) in 1971 [25]. From IST, soliton solutions exist when $\ddot{\beta}$ is a negative constant corresponding to the anomalous dispersion regime. For $\ddot{\beta} = -1$, the single soliton solution is given by

$$q(z,t) = A\,\mathrm{sech}\left[A\left(t + \nu z - t_0\right)\right]\exp\left[-i\nu t + \frac{i}{2}\left(A^2 - \nu^2\right)z + i\phi_0\right], \tag{1.9}$$

where A is the amplitude, ν is the velocity, t_0 is the initial temporal position, and ϕ_0 is the initial phase of the soliton [26]. From Eq. (1.9), the width of the soliton is inversely proportional to the amplitude of the soliton. That is, if the amplitude of the soliton increases, its width must be decreased in order to retain the soliton shape. This is a manifestation of the nonlinear nature of Eq. (1.8). For comparison, the amplitude and width of a pulse in a linear system are independent parameters. From Eq. (1.9), the soliton does not change its shape as it propagates. Besides distortionless propagation, solitons also emerge from collisions unscathed save for shifts in their initial positions and initial phases [27]. The amplitudes and velocities of the solitons remain unchanged by the collision. This is rather surprising giving the nonlinear nature of the equation. It is the ability of solitons to retain their identities during collisions that give them the name solitons.

Even though the inverse scattering transform solves the NLS equation exactly, it is seldom used in the study of soliton propagation in optical fibers partly because IST is a rather complex method. It is also because of the difficulty in incorporating perturbative effects in the IST formulation. The most important reason, perhaps, is that numerical solutions of Eq. (1.8) can be readily obtained. Instead of the complex analytical method of IST, numerical algorithms are straightforward to implement and perturbative effects can be included readily in the equations. Numerical simulations thus become the tool of choice in the investigations of NLS equation and its various modified versions. Nonetheless, results from the inverse scattering transform are very useful in providing benchmarks for the studies. Two types of numerical methods are commonly used in solving NLS-type equations; they are finite-difference methods and pseudo-spectral methods [2]. Among the different numerical methods, split-step Fourier method, a type of pseudo-spectral method, is the most widely used. In the split-step Fourier method, the equation is split into multiple partial equations each of which contains some of the operators in the original equation [2]. At each propagation step, the partial equations are solved in some chosen order. For example, the NLS equation can be split into the following system of equations,

$$i\frac{\partial q}{\partial z} + \left(\frac{1}{2}\right)\frac{\partial^2 q}{\partial t^2} = 0, \tag{1.10}$$

$$i\frac{\partial q}{\partial z} + |q|^2 q = 0. \tag{1.11}$$

Equation (1.10) contains the effect of chromatic dispersion only while Eq. (1.11) contains the effect of nonlinearity only. The algorithm consists of solving Eqs. (1.10) and (1.11) alternately at each propagation step size Δz. The output of one equation, Eq. (1.10) say, will become the input of the second equation, Eq. (1.11) in this case. For sufficiently small Δz, the iterative solutions of Eqs. (1.10) and (1.11) approximate that of the NLS equation. Note that both Eqs. (1.10) and (1.11) can be solved exactly for an given initial pulse. Since Fourier transform is used to solve Eq. (1.10), the split-step method is sometimes called the split-step Fourier method. The split-step Fourier method for solving the NLS equation is summarized in the following.

I Transform the pulse $q(z,t)$ into the frequency domain $\tilde{q}(z,\omega)$ using a fast Fourier transform (FFT) algorithm, where $q(z,t)$ is the envelope of the electric field and $\tilde{q}(z,\omega)$ is the amplitude of spectrum.

II Propagate the spectral components by, $\tilde{q}(z', \omega) = \tilde{q}(z, \omega) \exp(-i\omega^2 \Delta z/2)$. This is the dispersion step.

III Transform the spectrum $\tilde{q}(z', \omega)$ back to the time domain $q(z', t)$ by the inverse FFT.

IV Propagate the solution by, $q(z + \Delta z, t) = q(z', t) \exp(i|q(z', t)|^2 \Delta z)$. This is the nonlinear step.

V Repeat from Step I to IV. Substitute $q(z, t)$ with $q(z + \Delta z, t)$ and iterate until the accumulated normalized distance step size is equal to the required normalized transmission distance of the optical signal.

Apart from its simplicity, the split-step method given above is unconditionally stable. Stability is an important property of a numerical algorithm. If a numerical method is unstable, the error between successive numerical steps will grow uncontrollably rendering a solution impossible. Since the total energy $I_1 = \int_{-\infty}^{\infty} |q(z, t)|^2 \, dt$ is conserved by both Eqs. (1.10) and (1.11), the total energy is conserved by the split-step procedure. That is, the numerical solution will not grow out of control due to error accumulation.

Order of Accuracy of the Split-Step Fourier Method

The order of accuracy of a numerical algorithm gives the error in the numerical solutions as a function of the numerical parameters; Δz in the NLS equation example. In an n-th order accurate method, the numerical error of the solution made at each step is proportional to the $(n + 1)$-th power of the step size. In general, a numerical algorithm should be at least second order accurate. The rate of convergence towards the true solution is too slow in a first order algorithm. Algorithms with order of accuracy higher than two are not necessary better because the computational effort in each step is typically proportional to the order of the algorithm.

In the split-step Fourier method given by Eqs. (1.10) and (1.11). We approximate the true solution $q(z+\Delta z, t)$ by $\hat{D}(\Delta z)\hat{N}(\Delta z)q(z,t)$ where $\hat{D}(\Delta z)q = \exp[(i\Delta z/2)\partial^2/\partial t^2]q(z,t)$ and $\hat{N}(\Delta z)q = \exp(i\Delta z|q(z,t)|^2)q(z,t)$. The algorithm is only first order accurate, a second order accurate result can be obtained by symmetrizing the algorithm such as using $\hat{D}(\Delta z/2)\hat{N}(\Delta z)\hat{D}(\Delta z/2)$ instead of $\hat{D}(\Delta z)\hat{N}(\Delta z)$. In the following, we show that the symmetrized algorithm is indeed second order accurate.

The exact solution $q(z+\Delta z, t)$ of Eq. (1.8), can be obtained by using Taylor series expansion of $q(z,t)$ at z,

$$q(z+\Delta z, t) = q + \Delta z q_z + \left[\frac{(\Delta z)^2}{2!}\right] q_{zz} + \left[\frac{(\Delta z)^3}{3!}\right] q_{zzz} + \cdots,$$

where q_z represents $\partial q/\partial z$ at z, q_{zz} represents $\partial^2 q/\partial z^2$ at z, and so on. Using Eq (1.8) and set $\ddot{\beta}(z) = -1$, we have

$$\begin{aligned}
q_z &= i\left(\frac{1}{2}q_{tt} + |q|^2 q\right), \\
q_{zz} &= -\left(\frac{1}{4}q_{tttt} + 2|q|^2 q_{tt} + 2|q_t|^2 q + q_t^2 q^* + |q|^4 q\right), \\
q_{zzz} &= -i\left[\frac{1}{8}q_{tttttt} + \frac{5}{2}q^* q_{tt}^2 + 3q^* q_t q_{ttt} + 7|q_t|^2 q_{tt} + \frac{5}{2}q_t^2 q_{tt}^* + 2q|q_{tt}|^2 + 3qq_t^* q_{ttt} + qq_t q_{ttt}^*\right. \\
&\quad + |q|^6 q + 5|q|^2 q^* q_t^2 + \frac{11}{2}|q|^4 q_{tt} + \frac{3}{2}|q|^2 q_{tttt} + 12|q|^2 q|q_t|^2 + 2q^3\left(q_t^*\right)^2 + |q|^2 q^2 q_{tt}^* \\
&\quad \left. + \frac{1}{4}q^2 q_{tttt}^*\right],
\end{aligned}$$

where q_t represents $\partial q/\partial t$ at z, q_{tt} represents $\partial^2 q/\partial t^2$, *etc*, and q^* is the complex conjugate of $q(z,t)$. The derivation of q_{zz} and q_{zzz} is shown in Appendix A.5.

Evaluation of the numerical algorithm $\hat{D}(\Delta z/2)\hat{N}(\Delta z)\hat{D}(\Delta z/2)$, up to $(\Delta z)^2$ gives

$$
\begin{aligned}
\hat{D}\left(\frac{\Delta z}{2}\right) q &= \exp\left[i\left(\frac{\Delta z}{4}\right)\frac{\partial^2}{\partial t^2}\right] q, \\
&= \left[1 + i\frac{\Delta z}{4}\frac{\partial^2}{\partial t^2} - \frac{(\Delta z)^2}{32}\frac{\partial^4}{\partial t^4}\right] q, \\
\hat{N}(\Delta z)\hat{D}\left(\frac{\Delta z}{2}\right) q &= q + i\Delta z\left(|q|^2 q + \frac{1}{4}q_{tt}\right) - (\Delta z)^2\left(\frac{1}{32}q_{tttt}\right. \\
&\left. + \frac{1}{2}q_{tt}|q|^2 - \frac{1}{4}q_{tt}^* q^2 + \frac{1}{2}|q|^4 q\right) + \cdots, \\
\hat{D}\left(\frac{\Delta z}{2}\right)\hat{N}(\Delta z)\hat{D}\left(\frac{\Delta z}{2}\right) q &= q + i\Delta z\left(|q|^2 q + \frac{1}{2}q_{tt}\right) - (\Delta z)^2\left(\frac{1}{8}q_{tttt}\right. \\
&\left. + |q|^2 q_{tt} + |q_t|^2 q + \frac{1}{2}q_t^2 q^* + \frac{1}{2}|q|^4 q\right) \\
&- i(\Delta z)^3\left[\frac{1}{48}q_{tttttt} + \frac{1}{4}q|q_{tt}|^2 + \frac{1}{4}|q|^2 q_{tttt}\right. \\
&+ \frac{3}{8}q^* q_{tt}^2 + \frac{3}{4}|q|^4 q_{tt} + \frac{1}{6}|q|^8 q + \frac{1}{4}q_t^2 q_{tt}^* \\
&+ |q_t|^2 q_{tt} + \frac{1}{2}q^* q_t q_{ttt} + \frac{1}{2}q q_t^* q_{ttt} \\
&\left. + \frac{3}{4}|q|^2 q^* q_t^2 + \frac{3}{2}|q|^2 q|q_t|^2 + \frac{1}{4}q^3(q_t^*)^2\right] + \cdots. \qquad (1.12)
\end{aligned}
$$

The derivation is shown in Appendix A.6.

From Eq. (1.12), the coefficients of the Δz and $(\Delta z)^2$ terms are the same as that of the true solution, the deviation is proportional to $(\Delta z)^3$. Therefore, the accuracy of split-step Fourier method is second-order accurate. The difference between the exact solution and numerical solution at $(\Delta z)^3$ is

$$
\begin{aligned}
q_{\text{exact}} - q_{\text{app}} &= -i\left[\frac{1}{24}q^* q_{tt}^2 + \frac{1}{6}|q_t|^2 q_{tt} + \frac{1}{6}q_t^2 q_{tt}^* + \frac{1}{12}q|q_{tt}|^2 + \frac{1}{6}q q_t q_{ttt}^* + \frac{1}{12}|q|^2 q^* q_t^2\right. \\
&+ \frac{1}{6}|q|^4 q_{tt} + \frac{1}{2}|q|^2 q|q_t|^2 + \frac{1}{12}q^3(q_t^*)^2 + \frac{1}{6}|q|^2 q^2 q_{tt}^* + \frac{1}{24}q^2 q_{tttt}^* + \frac{1}{6}|q|^6 q \\
&\left. - \frac{1}{6}|q|^8 q\right]. \qquad (1.13)
\end{aligned}
$$

In Figure 1.4, we plot the magnitude of Eq. (1.13) for a fundamental soliton solution of Eq. (1.8); $q(z,t) = \text{sech}(t)\exp(iz/2)$. The maximum difference is about 0.100423 at

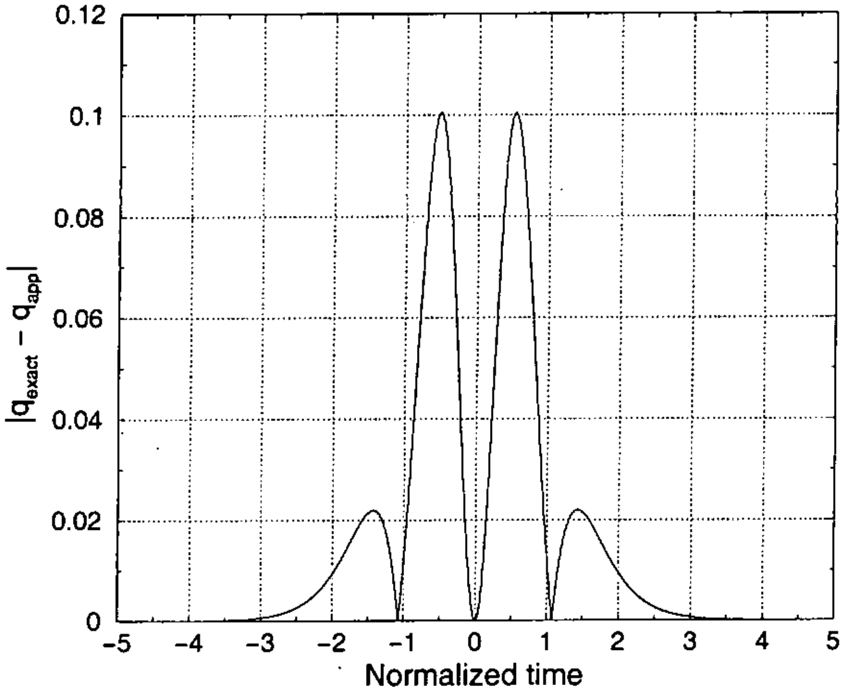

Figure 1.4: The coefficient leading order (Δz^3) error term in a symmetrized split-step Fourier algorithm. The simple soliton solution $q(z,t) = \mathrm{sech}(t)\exp(iz/2)$ is used.

$t = \pm 0.52$ with $\Delta t = 0.01$. Figure 1.4 is obtained by using Maple. The procedures are shown in Appendix A.7. The FFT and inverse FFT are the most computational intensive parts of the split-step Fourier algorithm. For each step in the second order algorithm $q(\Delta z, t) = \hat{D}(\Delta z/2)\hat{N}(\Delta z)\hat{D}(\Delta z/2)q(0,t)$, four FFTs are required; two for the forward transform and two for the backward transform. It therefore appears that $4n$ FFTs are required for a distance $z = n\Delta z$. Actually, because

$$\begin{aligned} q(z = n\Delta z, t) &= [\hat{D}(\Delta z/2)\hat{N}(\Delta z)\hat{D}(\Delta z/2)]^n q(0,t), && (1.14) \\ &= \hat{D}^{-1}(\Delta z/2)[\hat{D}(\Delta z)\hat{N}(\Delta z)]^n \hat{D}(\Delta z/2) q(0,t), && (1.15) \end{aligned}$$

the number of FFTs required is only $2n + 4$.

Comparison of Eqs. (1.14) and (1.15) shows that with simple pre-processing and post-processing, the results from the first order algorithm can be second order accurate.

Chapter 2

Dispersion Managed Systems

Dispersion managed (DM) systems are optical fiber transmission systems in which the dispersion coefficients vary periodically as a function of the propagation distance. Dispersion management allows one to minimize the effect of dispersion by maintaining a low average dispersion and at the same time reduce the coupling between the optical signals and the amplifier noises by maintaining a large local dispersion. A common dispersion map consists of two segments of fibers with large constant dispersion coefficients of opposite signs such that the average dispersion is close to zero. Dispersion management technique has been widely used in NRZ transmission format for several years.

For soliton systems, dispersion management is first proposed by K. Tajima in 1987 [28]. He suggested to tailor the dispersion profile in the fiber between two amplifiers to match the exponentially decreasing nonlinear effect. In a real system, the soliton power decreases exponentially as it propagates because of loss. Since the pulse width of a soliton is inversely proportional to the amplitude of the soliton, the power loss will lead to an exponential increase in the pulse width if the fiber dispersion is kept constant. If the fiber dispersion also decreases exponentially matching the decrease in power, the balance between the dispersion and nonlinearity is restored. The pulse width will then remain unchanged. However, a fiber with exponentially decreasing dispersion profile is difficult to manufacture especially when the length of the fiber segment becomes long. An alternative is to approximate the exponentially decreasing function by step functions [10, 29].

Conventional wisdom has it that solitons require constant anomalous dispersion [2], but it is discovered that solitons can propagate even in DM systems [30] if the length of dispersion map is much shorter than the soliton period of conventional soliton systems having the same average dispersion coefficient and pulse width of the DM systems. The periodic dispersion fluctuation over long transmission distance can then be averaged out. The long term evolution of the optical signal is again described by the NLS equation. The resulting DM solitons vary periodically along the fiber instead of remaining unchange as in the case of conventional solitons. It is shown that a two-step dispersion map in which the two fiber segments have the same length is characterized by two parameters; the map strength and the map depth [11]. The map strength $S = l\Delta\ddot{\beta}/\tau^2$ measures the cumulated absolute dispersion in one dispersion map with segment length l. The parameter τ is the minimum full width at half maximum intensity (FWHM) of the DM solitons and $\Delta\ddot{\beta}$ is the sum of the absolute dispersion coefficients between the two fiber segments. The map depth is given by $\delta = \Delta\ddot{\beta}/\ddot{\beta}_{\mathrm{av}}$ where $\ddot{\beta}_{\mathrm{av}}$ is the average dispersion coefficient. DM soliton systems have many advantages over conventional soliton systems. We shall discuss them in the next Section.

2.1 Advantages of Dispersion Managed Systems

2.1.1 Reduction of Collision-induced Timing Jitter

Dispersion managed soliton systems can reduce the collision-induced frequency shift in Wavelength Division Multiplexing (WDM) systems [10, 31, 32, 33]. In soliton WDM systems, one of the major concerns is collision-induced timing jitters. Even for ideal conventional solitons, collisions between solitons at different wavelength channels will result in timing jitters [34]. Although the amplitudes and velocities of the solitons remain unchange after a collision between conventional solitons, both the phases and the positions of the solitons will be shifted. The pulses arrive at the receivers either earlier or later than expected without the collision. After several collisions, the pulse may be shifted beyond the bit slot assigned for each pulse, thus leading to errors in detection.

In real systems with fiber loss and amplifiers, the situation worsens because even the central frequencies of the pulses could be shifted after a collision. The fluctuation of the pulse intensity during a gain/loss cycle could lead to serious asymmetric frequency shifts during collisions [27]. The dissipation of the soliton energy during the first half of the collision may be larger than that during the second half of the collision. Note that first half of collision starts when the solitons overlap at the half-power point to when the solitons completely overlap. The second half of the collision starts at the point of complete overlap to where the solitons overlaps at the next half-power points. Since the frequency shift during a collision is a nonlinear phenomenon, it depends on the energy of the pulse. The frequency shift in the first half of the collision therefore cannot compensate that of the second half of the collision [27]. The resulting frequency shift will lead to a change in

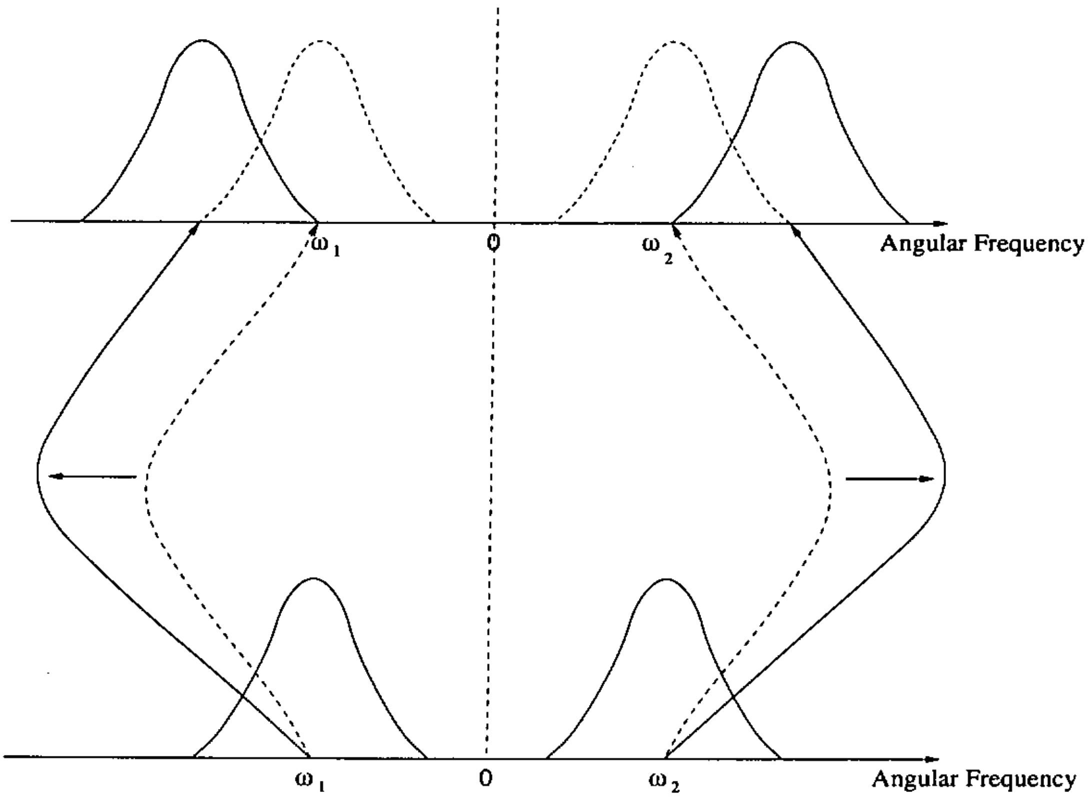

Figure 2.1: Frequency shift during a soliton collision. Dashed line represents a collision in a lossless system. Solid line represents a collision in a system with loss.

the group velocity of the pulse and thus a change in the transmission delay of the channel. Figure 2.1 shows the frequency shifts of two solitons during a collision. The dashed line is the evolution of the carrier frequencies of the solitons during a collision in a lossless system. The carrier frequencies return to their initial values after the collision. The solid line gives the evolution of the carrier frequencies of the solitons in a system with loss. The carrier frequencies do not return to its initial values after the collision.

In a DM system, the large local dispersion within a dispersion map results in a shorter collision length. The collision length is given by $2\tau/D\Delta\lambda$ [27] which is the distance in which the pulses overlap at their half power points, where τ is the pulse width, D is the dispersion coefficient, and $\Delta\lambda$ is the wavelength difference between the two colliding pulses. The reduction in the collision length also reduces the degree of asymmetry in the frequency shift when compared to that in uniform anomalous dispersion systems [11]. For the same tolerance in timing jitter, the maximum transmission distance of DM soliton system is then longer than that of conventional soliton system. It is shown that the larger the map strength and the map depth, the larger the reduction in the collision-induced timing jitter [31]. By using dispersion management technique, G. Vareille *et al.* achieved 34 × 10 Gb/s straight-line transmission over transatlantic distance, 6,380 km [35]. Y. Yamada *et al.* also succeed to have 100 × 10 Gb/s transmission over 7,300 km in a loop experiment [1]. Both experiments used RZ transmission format.

2.1.2 Increase in the Signal-to-Noise Ratio

Dispersion managed solitons have higher signal-to-noise ratio than the conventional solitons because of the energy enhancement effect in DM solitons [9, 11]. Energy enhancement is the increase in the energy of DM solitons when compared to the soliton energy in conventional systems having the same average dispersion and pulse width. In conventional systems, the solution of Eq. (1.8) is $A\,\mathrm{sech}(At/\sqrt{|\ddot{\beta}_{\mathrm{av}}|})\exp(-iA^2z/2)$ assuming that $\ddot{\beta}(z) = \ddot{\beta}_{\mathrm{av}}$ is a negative constant, where A is pulse amplitude. The total energy of the fundamental soliton is given by $2(1.763)|\ddot{\beta}_{av}|/\tau$, where τ is the FWHM of the pulse. In determining the energy enhancement, the minimum width in a DM soliton period is used for the pulse width of the conventional solitons. The energy enhancement of a two-step dispersion map with equal fiber length segments is proportional to the map strength and map depth [11].

Since noise power is nearly constant, an increase in signal strength will improve the signal-to-noise ratio which in turn will increase the maximum transmission distance for the same average dispersion and transmission bit rate.

2.1.3 Reduction of Gordon-Haus Timing Jitter

Gordon-Haus timing jitter is the result of the coupling between solitons and amplification spontaneous emission (ASE) noises of the Erbium-Doped fiber amplifiers [36]. The central frequency of the soliton varies randomly and leads to random variation of the transmission delay. The Gordon-Haus timing jitter is inversely proportional to the total energy of the soliton. Because DM solitons have higher energy than conventional solitons with the same average dispersion and pulse width, Gordon-Haus timing jitter is reduced in DM soliton systems [12, 37, 38]. Strong dispersion maps have larger energy enhancement, thus a larger reduction of the Gordon-Haus timing jitter.

2.1.4 Reduction of Third-order Dispersion in WDM systems

Another advantage of DM systems is the reduction of the third-order dispersion effect in WDM systems [11]. In communication grade fibers, the group velocity dispersion coefficients increase as the wavelength increases. Therefore, in a WDM system using conventional solitons, the channel power increases as the wavelength of the channel increases because of the increase in dispersion effects. The transmission distance is then limited by the detection of the channel which has the lowest power.

In DM soliton systems, the energy enhancement is proportional to the map depth, $\Delta\ddot{\beta}/|\ddot{\beta}_{\mathrm{av}}|$, of the dispersion map where $\ddot{\beta}_{\mathrm{av}}$ is the average dispersion coefficient and $\Delta\ddot{\beta}$ is the absolute sum of the dispersion coefficients in the two fiber segments of the dispersion map. As the channel wavelength increases, the average dispersion in the DM system increases. The depth of the dispersion map thus reduces. The energy enhancement then decreases. The variation of channel power due to third order dispersion will then be reduced [11].

2.2 Solutions of Dispersion Managed solitons

The equation governing pulse evolution in a dispersion managed system is given by

$$i\frac{\partial q}{\partial z} - \left[\frac{\ddot{\beta}(z)}{2}\right]\frac{\partial^2 q}{\partial t^2} + |q|^2 q = 0, \tag{2.1}$$

where $q(z,t)$ is the slowly varying envelope of the electric field, z is the normalized distance, t is the normalized time, and $\ddot{\beta}(z)$ is the dispersion map configuration. For a simple two-step dispersion map, $\ddot{\beta}(z)$ is given by

$$\ddot{\beta}(z) = \begin{cases} \ddot{\beta}_1 & 0 < z - L\lfloor z/L \rfloor < l_1/2, \\ \ddot{\beta}_2 & l_1/2 < z - L\lfloor z/L \rfloor < l_1/2 + l_2, \\ \ddot{\beta}_1 & l_1/2 + l_2 < z - L\lfloor z/L \rfloor < L, \end{cases} \tag{2.2}$$

where $L = l_1 + l_2$ is the map length, l_i and $\ddot{\beta}_i$, $i = 1, 2$, are the lengths and dispersion coefficients of the fiber segments. Eq. (2.2) is an example of a symmetric map. At the beginning and the end of each map, the soliton solution is chirp free [20].

In principle, Eqs. (2.1) and (2.2) can be solved exactly, *i.e.*, for any input pulse profile to the DM system the pulse evolution can be solved analytically. The reason is that $\ddot{\beta}(z)$ is a piecewise constant function, the pulse evolution in each fiber segment can be solved using the inverse scattering transform. The output waveform from one fiber segment will become the initial waveform for the next fiber segment. This procedure however cannot determine the steady state or periodic solutions of DM systems. J. H. B. Nijhof *et al.* [22] propose a numerical procedure that can find periodic solutions of DM systems. A numerical solution is of course not a mathematical proof that an analytical solution actually exists. Numerical solutions at best can only be the exact solutions of the discrete map which constitutes the numerical algorithm utilized to solve Eqs. (2.1) and (2.2). The truncation errors of the computers make even this claim questionable. Whether exact analytic solutions exist for Eqs. (2.1) and (2.2) is not critical for communication systems, however. Given all the perturbations in a fiber that are ignored in the derivation of Eqs. (2.1) and (2.2), the real pulse will not be an exact soliton even if soliton solutions actually exist for the equations. We shall therefore interpret the existence of numerical periodic solutions as a strong indication that solitary waves may propagate in the DM systems modeled by Eqs. (2.1) and (2.2).

2.2.1 Numerical Averaging Technique

The most successful numerical technique used to find the solutions of DM systems is the averaging method proposed by J. H. B. Nijhof *et al.* [22]. The procedure of the averaging technique in lossless cases is described below.

1. Propagate an initial pulse with an amplitude obtained from the approximate equation of energy enhancement given in [13, 14].

2. Record the pulse width at the same point of each dispersion map. Store the pulse profile if the pulse width fluctuation is at a local maximum or minimum point. Those points are found by comparing the current pulse width with recorded pulse widths from previous numerical steps.

3. When there are two extremas, the two stored pulses will be dechirped and then averaged. The dechirping process is to subtract the phase value at the peak amplitude from the whole pulse. Then the phases of both pulses at their peak amplitude will be zero. If the maximum amplitude of the pulse is at $t = t_{\max}$, then the dechirping procedure is represented by

$$q_{\rm av}(z,t) = q(z,t) \times \left[\frac{q^*(z,t_{\max})}{|q(z,t_{\max})|}\right],$$

   where $q_{\rm av}$ is the dechirped pulse. One should ensure that the centers of mass of the two pulses are aligned when one performs the averaging.

4. After averaging, the total energy of the averaged pulse must be rescaled to the initial value to maintain conservation of energy, *i.e.*, $q_{\rm rescale}(z,t) = q_{\rm av}(z,t) \times \sqrt{E_0/E_{\rm av}}$, where $q_{\rm rescale}(z,t)$ is the rescaled pulse, $q_{\rm av}$ is the averaged pulse in Step 3, E_0 is the total energy of the initial pulse, and $E_{\rm av} = \int_{-\infty}^{\infty} |q_{\rm av}(z,t)|^2\, dt$ is the total energy of the averaged pulse. The rescaled pulse is then launched into the next space step of the system.

5. Repeat from Step 2 to 4 until the accumulated distance is equal to the required transmission distance.

A key to successful implementation of the averaging method is that periodic boundary conditions should be used for the time variable. If absorbing boundary condition is used at the edges of the timing window to simulate infinite time axe, standing waves pattern will be formed from the outgoing dispersion waves shed by the input pulses and their reflection at the absorbers. The error floor of the intensity-time plot will then appear at 10^{-12} or 10^{-13} at best, instead of at 10^{-22} or 10^{-24} as reported by J. H. B. Nijhof *et al.*.

Normally periodic boundary condition should not be used for the time variable because of the aliasing effect. The dispersion waves leaving from one side of the computation window will appear at the opposite side of the window and eventually affect the region of interest at the center. However, in numerical averaging method, it is this aliasing effect together with the rescaling of the energy that are important in reshaping pulse.

To understand how the procedure works, we assume that the initial pulse contains a DM soliton and linear dispersive waves. We also assume that the phase of a DM soliton at any point in a dispersion map is given by $\phi(z,t) = g(z,t) + f(z)$, where $g(z,t)$ is a periodic function of z. The period equals a map length and $f(z)$ is a function of z only. For conventional solitons, $g(z,t) = 0$. The waxing and waning of the signal is due to linear superposition of the DM soliton and the dispersive waves. The dechirping procedure aligns the phases of the DM solitons at two different locations such that they will be added constructively in the averaging process. As for the linear dispersive waves at the two z-locations, in general they are out of phase only at the peak amplitude position. But since the dispersive waves at the two z-locations are not coherent, the averaging process will reduce the strength of the dispersive waves. As an illustration of how the averaging process works, let the DM soliton at a chosen point of a dispersion map be given by $|q_{\mathrm{s}}(z,t)| \exp\left[ig(z,t) + if(z)\right]$. Without loss of generality, we assume that the maximum of $|q(z,t)|$ at a given z occurs at $t = 0$. Also, we assume $g(z,0) = \phi(z)$. If the DM soliton is mixed with a sinusoidal wave given by $\epsilon \exp\left[i(\beta z - \omega t)\right]$, where β is the propagation constant and ω is the angular frequency, the total electric field is

$$q_{\mathrm{T}}(z,t) = |q_{\mathrm{s}}(z,t)| \exp\left[ig(z,t) + if(z)\right] + \epsilon \exp\left[i(\beta z - \omega t)\right]. \tag{2.3}$$

At $t = 0$, $q_{\mathrm{T}}(z,0) = \left\{|q_s(z,0)| + \epsilon \exp\left[i\beta z - i\bar{f}(z)\right]\right\} \exp\left[i\bar{f}(z)\right]$, where $\bar{f}(z) = f(z) + \phi(z)$. The pulse intensity reaches the maximum when $\beta z - \bar{f}(z) = 2n\pi$, where n is an integer. The pulse intensity reaches the minimum when $\beta z - \bar{f}(z) = (2n+1)\pi$. Averaging the two dechirped pulse shapes at the maximum and the minimum amplitudes z-locations removes the sinusoidal wave completely.

2.2.2 Simulation Results

We apply the numerical averaging technique described in the previous Section to solve Eqs. (2.1) and (2.2) using different input pulse energies. The initial pulse profile does not affect the outcome of the averaging procedure. We find that periodic solutions exist for different input pulse energies and dispersion map configurations. As an example, we choose a dispersion map with dispersion coefficients of the two fiber segments given by 4.9 $\mathrm{ps}^2/\mathrm{km}$ and -5.1 $\mathrm{ps}^2/\mathrm{km}$. The length of both fiber segments are 100 km. The initial pulse shape is $4.15\exp(-t^2/2T_0^2)$. The full width at half intensity (FWHM) of the initial pulse is 20 ps. The computation window in the time domain is 850 ps, the number of time steps is $2,048$, and the normalized distance step size is 2.5×10^{-4}.

The variation in the pulse width and amplitude for $200,000$ km, *i.e.*, 1,000 dispersion maps is shown in Figures 2.2 and 2.3, respectively. We observe that the pulse width and pulse amplitude reach constant values after about $25,000$ km which is 125 dispersion maps. At the end of $200,000$ km, the variation of the pulse width and pulse amplitude within a dispersion map are shown in Figures 2.4 and 2.5, respectively. Similar to conventional solitons, the peak amplitudes of DM solitons are inversely proportional to their widths. The pulse width varies periodically within a dispersion map and it reaches a

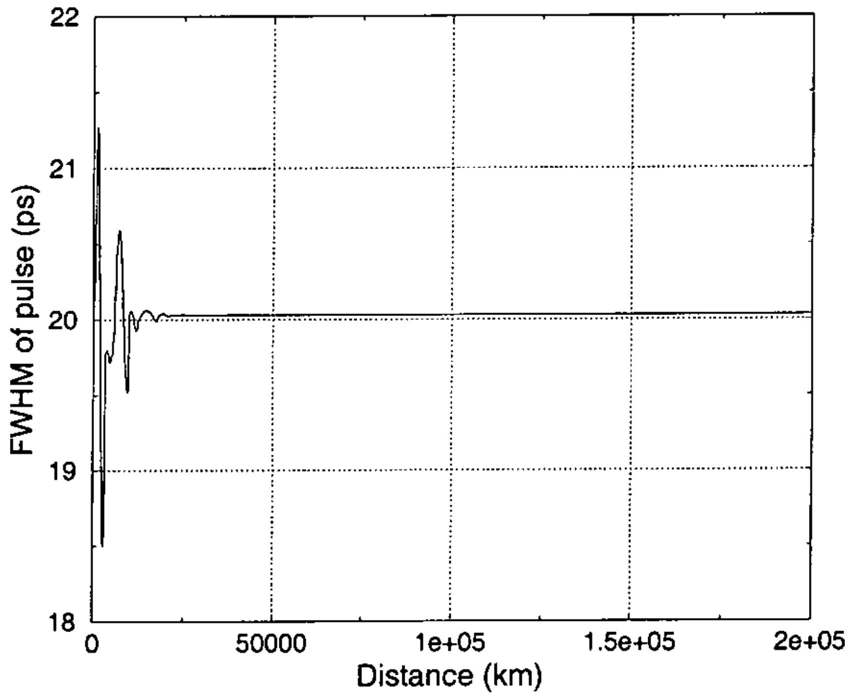

Figure 2.2: FWHM at the end of each map as a function of distance. The initial pulse is $4.15\exp(-t^2/2T_0^2)$. The initial pulse width is 20 ps. The dispersion map consists of two fiber segments of 100 km each. The map begins at the mid-point of the anomalous dispersion fiber. The GVD coefficients are 4.9 ps^2/km and -5.1 ps^2/km. The averaging distance is 1,000 dispersion maps.

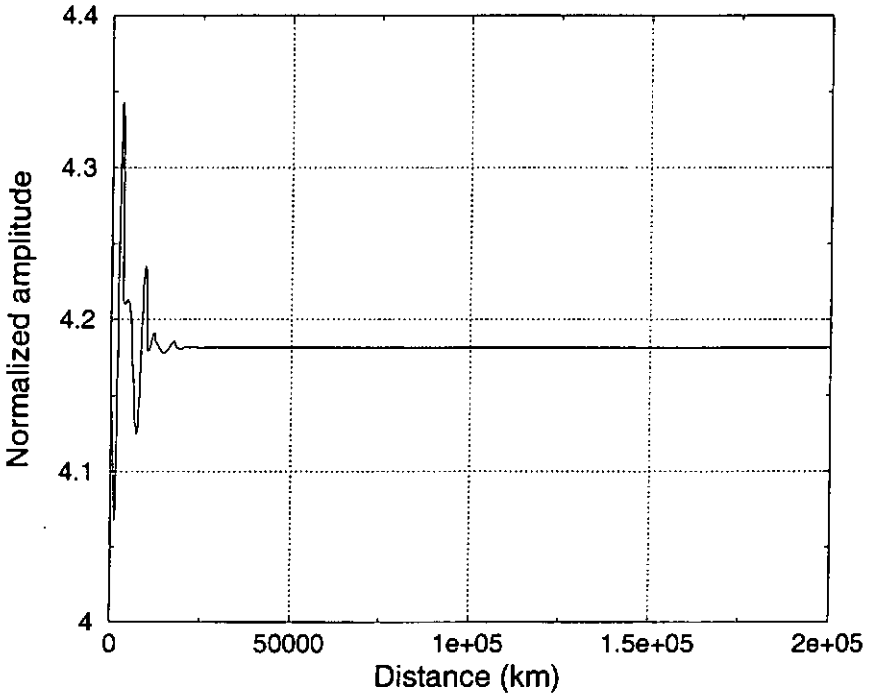

Figure 2.3: Normalized amplitude at the end of each map as a function of distance. The parameters are the same as that in Figure 2.2.

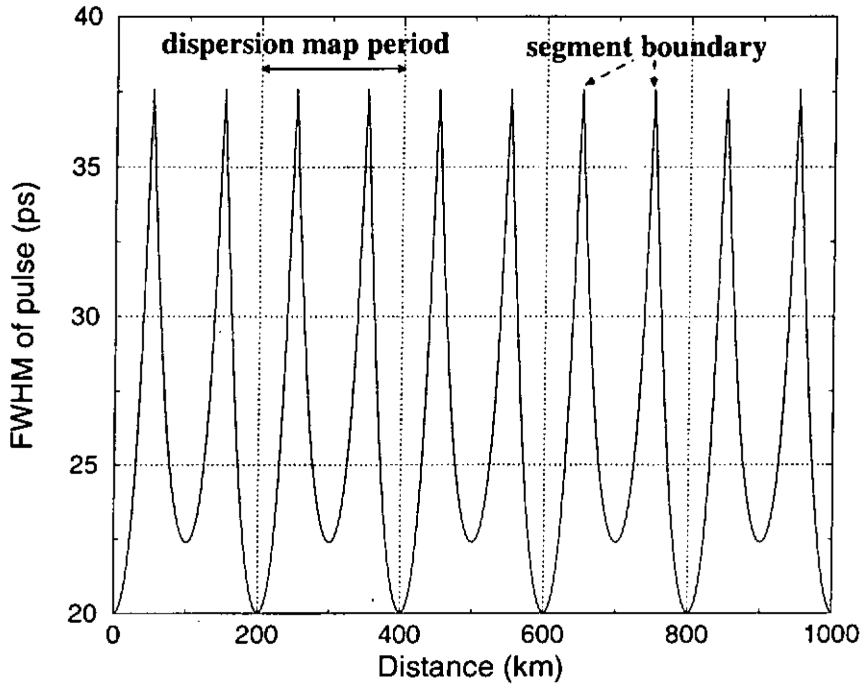

Figure 2.4: Evolution of the FWHM of a DM soliton in 5 dispersion maps. The parameters are the same as that in Figure 2.2.

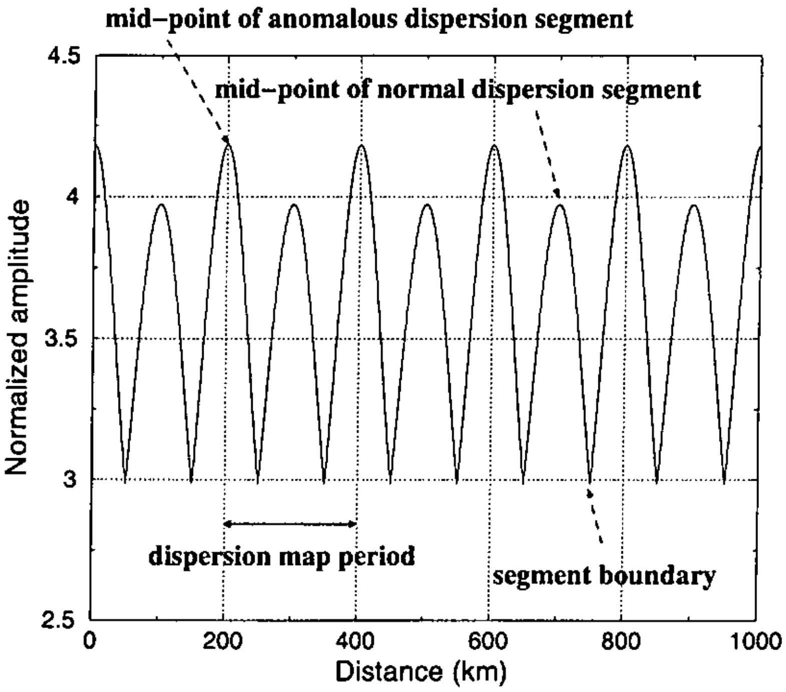

Figure 2.5: Evolution of the normalized amplitude of a DM soliton in 5 dispersion maps. The parameters are the same as that in Figure 2.2.

local minimum at the mid-point of each fiber segment. The pulse width at the mid-point of the anomalous dispersion fiber is smaller than that of the normal dispersion fiber. The maximum pulse width occurs where different fiber segments are concatenated together.

Figure 2.6 gives the intensity-time plot of the DM soliton at the mid-point of the anomalous dispersion fiber (solid line) and segment boundary (dotted line). At the mid-point of the anomalous dispersion fiber, the pulse consists of a main central peak and many sidelobes at successively lower amplitudes. The main peak is Gaussian in shape while the amplitudes of the sidelobes decrease exponentially with time. At the segment boundary, the pulse broadens and resembles a hyperbolic secant pulse. Figure 2.7 shows the spectra of the DM soliton at the mid-point of the anomalous dispersion fiber (solid line) and the segment boundary (dotted line). At the mid-point of the anomalous dispersion fiber, the central peak is Gaussian. There is no sidelobe and the spectrum decays exponentially. At

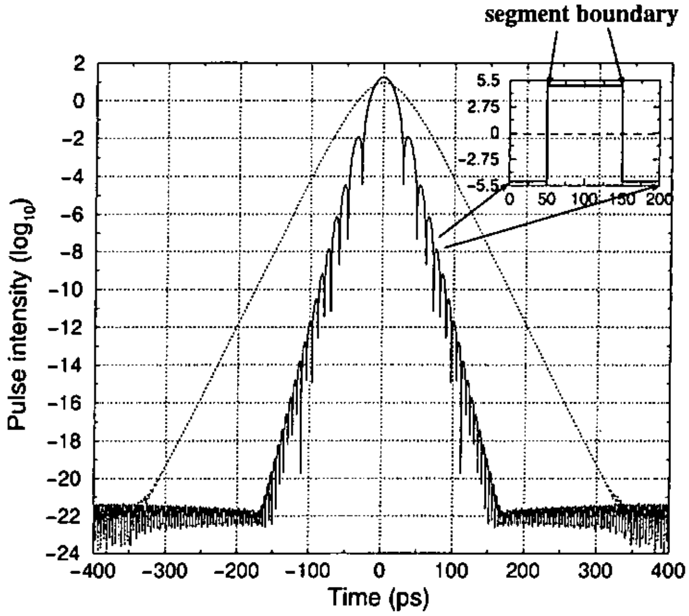

Figure 2.6: Intensity-time plots of a DM soliton at the mid-point of the anomalous dispersion fiber segment (solid line) and the segment boundary (dotted line). The parameters are the same as that in Figure 2.2.

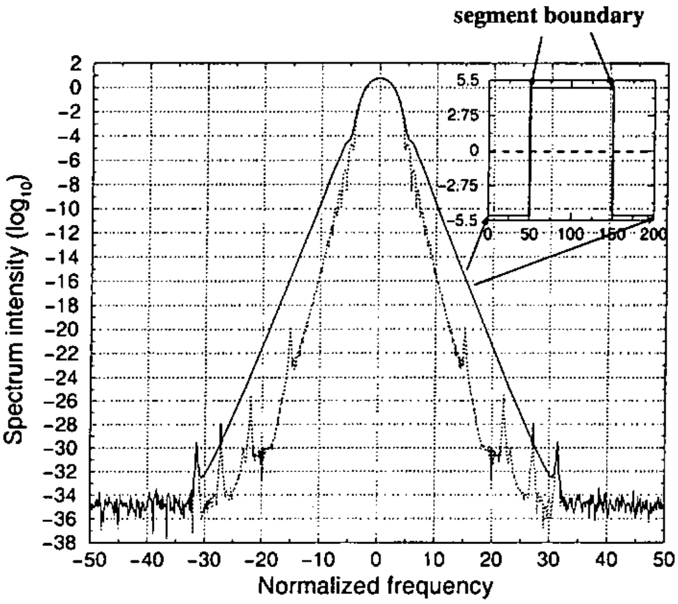

Figure 2.7: DM soliton spectra at the mid-point of the anomalous dispersion segment (solid line) and the segment boundary (dotted line). The parameters are the same as that in Figure 2.2.

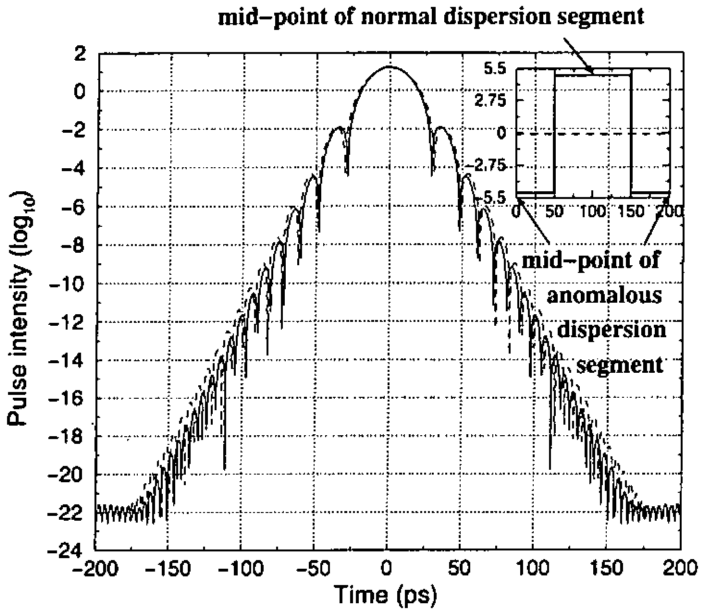

Figure 2.8: Intensity-time plots at the mid-point of the anomalous dispersion fiber (solid line) and the normal dispersion fiber (dashed line). The parameters are the same as that in Figure 2.2.

the segment boundary, the spectrum has a central peak that resembles a Gaussian shape and sidelobes. The spikes in Figure 2.7 are due to numerical error [39]. Decreasing the step size Δz will decrease the amplitudes of the spikes. Figure 2.8 shows the intensity-time plot of the DM soliton at the mid-point of the anomalous dispersion fiber (solid line) and the mid-point of the normal dispersion fiber (dashed line). The pulse shapes resembles each other, *i.e.*, a central Gaussian peak and sidelobes of exponentially decreasing amplitudes. Figure 2.9 gives the spectra of the DM soliton at the mid-point of the anomalous dispersion fiber (solid line) and the normal dispersion fiber (dashed line). We observe that the spectrum of the soliton at the mid-point of the normal dispersion fiber also contains sidelobes.

The error floor of the results has an normalized intensity of 10^{-22} in the time domain. The simulations are carried in a PIII 500 MHz personal computer using 32 bits to represent

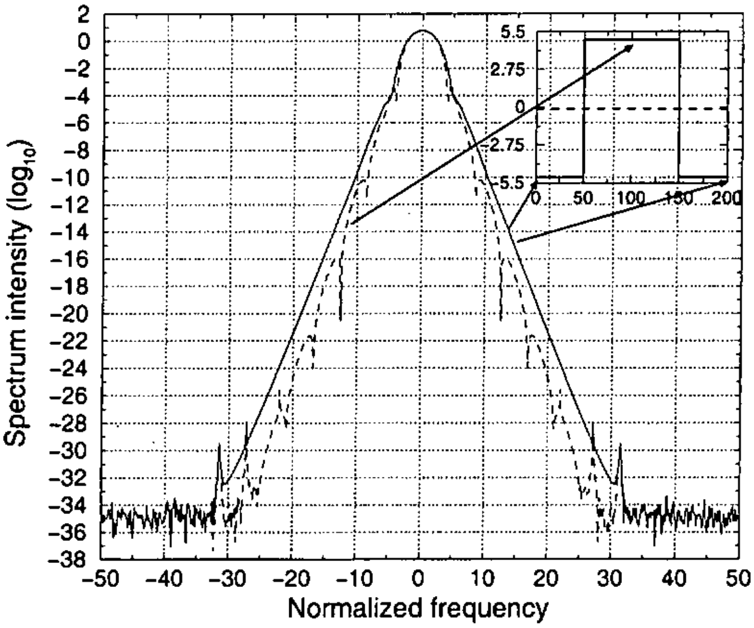

Figure 2.9: DM soliton spectra at the mid-point of the anomalous dispersion (solid line) and the normal dispersion (dashed line) segment. The parameters are the same as that in Figure 2.2.

a floating point number. Long double precision is used. The truncation error for the calculation of the field amplitude is about 16 decimal point. The normalized z step size is 2.5×10^{-4}. The algorithmic error in the calculation of the field amplitude in a single step is on the order of 10^{-11}. The solution given in Figure 2.6 is therefore at the accuracy limit of the algorithm used to solve Eq. (2.1). From Figure 2.6, the tails of the pulse at large t in both position of the map is approximately a straight line indicating an exponential decay.

The dynamics on the chirp-width plane is a good way to study the evolution of DM solitons. The chirp of a pulse is the variation of the instantaneous frequency across the pulse. Here we assume that the chirp is linear or equivalently the phase of the soliton

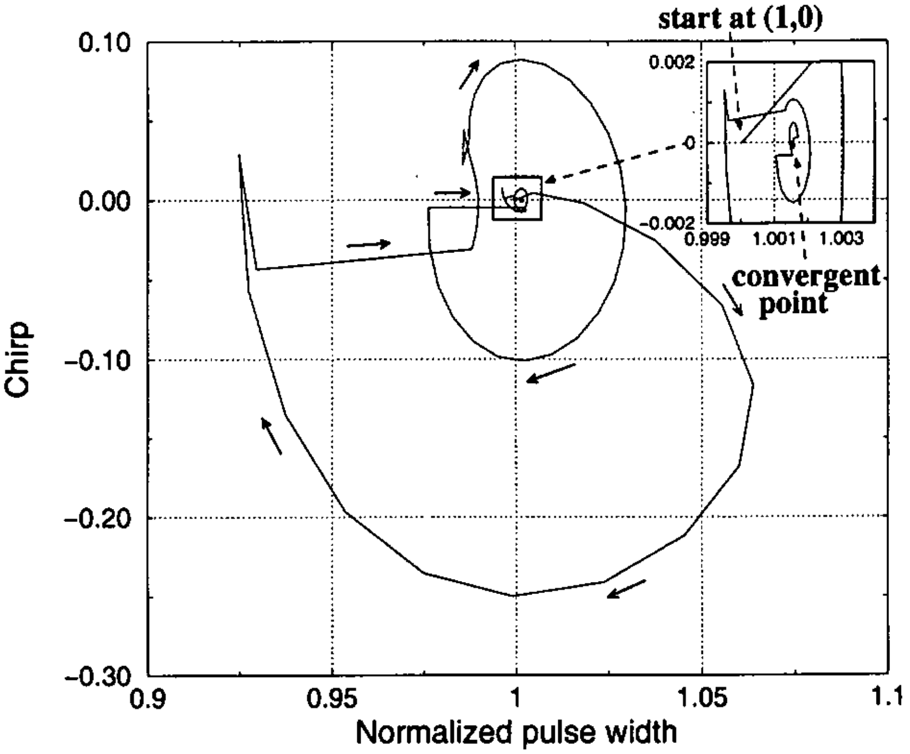

Figure 2.10: Chirp as a function of normalized pulse width at the end of each dispersion map during the averaging process. The variation starts at the point (1,0). The parameters are the same as that in Figure 2.2.

varies quadratically in time. The weighted chirp coefficient [22] is defined as

$$C = \frac{\operatorname{Im}\left\{\int_{-\infty}^{\infty} q^2(z,t)[q_t^*(z,t)]^2\,dt\right\}}{\int_{-\infty}^{\infty} |q(z,t)|^4\,dt},$$

where $q(z,t)$ is the envelope of the pulse, and $q_t^*(z,t)$ is the complex conjugate of $\partial q/\partial t$.

One can use the evolution in the chirp-width plane to monitor the progress of the averaging process. If a periodic solution exists, the curve will converge to a fixed point. Figure 2.10 shows such a evolution. Initially, the chirp parameter is zero and the normalized pulse width is one. After some wandering, the curve converges back to a point with zero chirp and a normalized pulse width of 1.0015593. This shows that the energy enhancement chosen for the initial pulse is approximately correct. The kinks in the chirp-

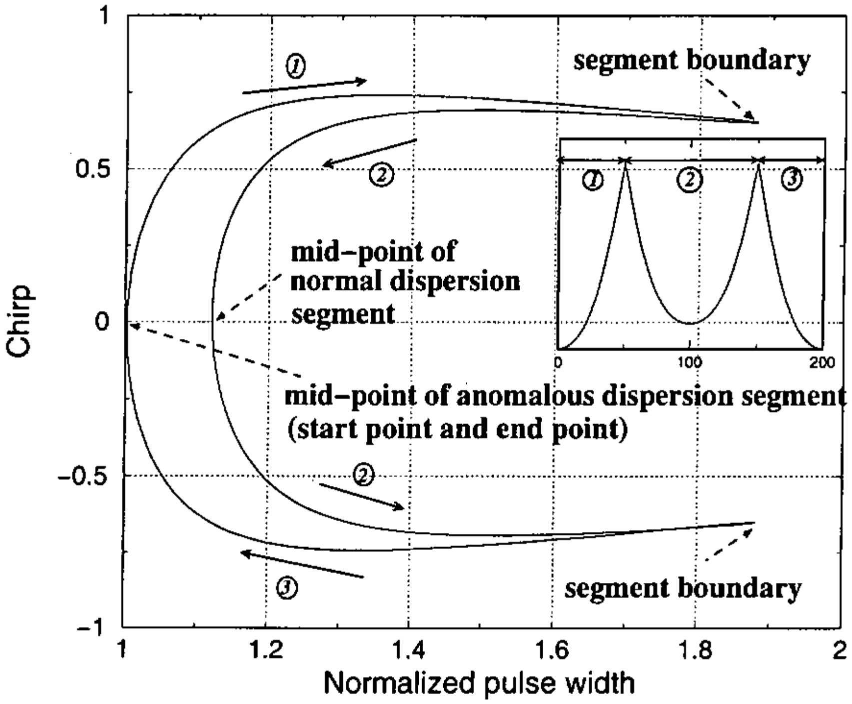

Figure 2.11: Chirp versus normalized pulse width within a dispersion map. The inset diagram shows the pulse width variation along the dispersion map. Region 1, 2, and 3 represent the three fiber segments in the dispersion map. The parameters are the same as that in Figure 2.2.

width curves are due to the numerical averaging processes. In Figure 2.11, we plot the the chirp-width dynamics of a DM soliton within a dispersion map. We start from the mid-point of the anomalous dispersion fiber segment. The DM soliton is chirp free there. As the soliton propagates, both the chirp and the pulse width increases until the soliton enters the normal dispersion fiber. Then, both the chirp and the pulse width decreases but they do not retrace the previous trajectory. The pulse width reaches the minimum at the mid-point of the normal dispersion fiber segment at which the soliton becomes chirp free again. Then as the soliton continues to propagate along the normal dispersion fiber, its width begin to increase and the chirp becomes more negative. Eventually, when the soliton emerges from the normal dispersion fiber, its pulse width is at its maximum which is the same as that when it enters the normal dispersion fiber. The magnitude of the chirp is also the same but the sign is reversed. When the soliton enters the anomalous dispersion fiber, the pulse width decreases while the chirp increases such that the soliton returns to the initial chirp free point when it reaches the mid-point of the anomalous dispersion fiber. For convention soliton systems, bright solitons are possible only for anomalous dispersion fibers. However, it has been shown that DM solitons also exist in zero and normal average dispersion [20].

Chapter 3

Fiber Bragg Gratings

Fiber Bragg gratings have emerged as important components in a variety of lightwave applications [40]. Their unique filtering properties and versatility as in-fiber devices are illustrated by their use in wavelength-stabilized lasers, fiber lasers, remotely pump amplifiers, Raman amplifiers, phase conjugators, wavelength converters, passive optical networks, wavelength division multiplexers/demultiplexers, add/drop multiplexers, dispersion compensators, and gain equalizers. Some applications of fiber grating technology are vital to the current success of long haul dense wavelength division multiplexing (DWDM) systems. For example, without gain equalization filters, the usable bandwidth of EDFA available for transmission will be significantly less than the generally accepted range of 35 nm (1530 to 1565 nm). In gain equalization, long period fiber grating filters are designed to approximate the inverse characteristics of the combination of EDFA and a fiber span [41].

Chirped fiber gratings are effective solutions for dispersion compensation in dense, high bit-rate WDM systems because of the high bandwidth dispersion product, figure of merit

[16], the capability to compensate high order dispersion, low insertion loss, and the absence of nonlinear effects [42]. Recent improvements in broadband grating fabrication technique have led to a number of DWDM demonstrations for 1.5 μm systems using conventional single mode fibers. Examples include an 8×10 Gb/s, 100 km system with a single 10 nm bandwidth grating, a 16×10 Gb/s, 840 km system using eleven 6.5 nm gratings, and an 8×20 Gb/s, 315 km system using four 6.5 nm gratings [43]. The use of chirped fiber Bragg gratings for dispersion compensation in high bit-rate, single-wavelength fiber-optic communication systems has been proved to be very effective.

In this Chapter, we will discuss the characteristics of fiber Bragg gratings (FBG). In Section 3.1, we give a brief background of FBGs and the couple mode equations that are used to study the properties of FBGs. In Section 3.2, we study the basic properties of uniform and non-uniform FBGs. In Section 3.3, we give the numerical solutions of a DM system using an ideal grating for dispersion compensation.

3.1 Modeling Fiber Bragg Gratings

3.1.1 Background

A fiber Bragg grating is a piece of fiber in which the refractive index of the fiber core varies. The fluctuation is induced by the interference of two diffracted ultraviolet (UV) beams from a phase mask. A phase mask is a lens with grooves on the surface. The fabrication of fiber gratings is shown in Figure 3.1. The UV beam, usually with wavelength around 248 nm or 193 nm, is perpendicularly incidented into the phase mask, which has a period of a range between half to one wavelength of the incident UV beam. The interference between

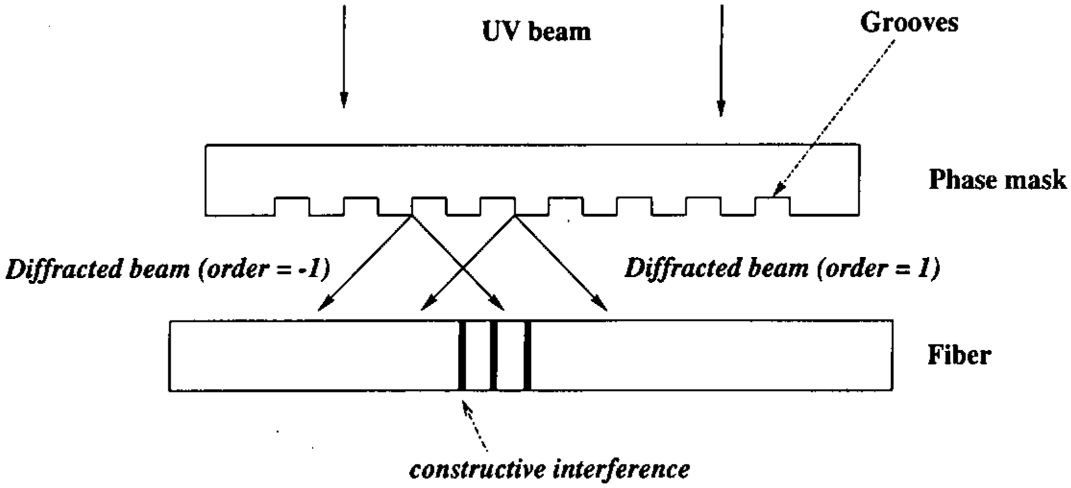

Figure 3.1: Fabrication of fiber Bragg gratings by scanning UV beam along an optical fiber.

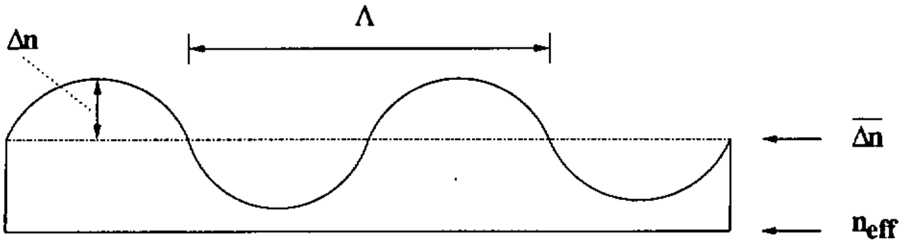

Figure 3.2: The refractive index variation of fiber Bragg gratings. The parameters Λ is the period, Δn is the amplitude, and $\overline{\Delta n}$ is the mean of the variation while n_{eff} is the effective refractive index.

the diffracted beams will result in an uneven distribution of temperature in the fiber. An increase in temperature increases the refractive index of the fiber because of interference effect. The variation of the refractive index is a periodic function [16]. Figure 3.2 shows a typical variation of the refractive index, where Λ is the period of the variation, $\overline{\Delta n}$ is the average value of the refractive index, Δn is the maximum amplitude of variation, and n_{eff} is the effective refractive index of the fiber. The variation of the refractive index can be modeled by a periodic function $\delta n(z)$ given by [16],

$$\delta n(z) = \overline{\Delta n}\left\{1 + \nu \cos\left[\left(\frac{2\pi N}{\Lambda}\right) z + \phi(z)\right]\right\},$$

where $\nu\overline{\Delta n} = \Delta n$, ν is the visibility of the fringes on the grating, N is the order of the diffracted UV beam, $\phi(z)$ is the phase change of grating, and z is the position on the grating.

There are two types of fiber gratings: transmission gratings and reflection gratings. Chirped reflection gratings can induce different time delay to different spectral components of a pulse for dispersion-compensating purpose. In the following, we limit our studies to reflection gratings only.

3.1.2 Couple Mode Equations

Wave propagation in optical fibers can be analyzed by solving the Maxwell's equation with appropriate boundary conditions. The weak guidance of fibers allows the decomposition of the propagation modes into an orthogonal set of polarized modes. If the fiber is free of any perturbations, these guided modes propagate along the fiber independently. If the fibers have imperfections, such as a periodic variation in the refractive index, the perturbations couple the guided modes of the fiber among each other. Power will be transferred from one propagation mode into another. When the perturbation is weak, one can assume that the mode fields of the guided modes are unchanged [16]. A set of first-order differential equations results which give the change of the amplitude of the mode fields along the fiber. This technique is called the coupled-mode theory. It is commonly used to study the behavior of fiber Bragg gratings because of its simplicity and its accuracy in modeling the properties of most fiber gratings.

The couple mode equations have been derived by many authors. Thus the derivation will not be repeated here. It is suffice to note that for significant transfer of energy between two mode fields, the two modes should remain in phase over a significant distance. A simple way to satisfy this phase-matching condition is the interaction between a forward-propagating mode and an identical backward-propagating mode [16].

Let the forward propagating mode be $R(z,t) = A(z)\exp[i(\Delta\beta)z/2 - i\omega t - \phi(z)]$ and the backward propagating mode be $S(z,t) = B(z)\exp[-i(\Delta\beta)z/2 - i\omega t + \phi(z)]$, where $A(z)$ and $B(z)$ are the amplitude of the forward and backward modes, t is the normalized time, z is the normalized propagating distance, $\Delta\beta$ is the difference between the propagation constant of the forward and backward propagating modes, ω is the normalized angular frequency of pulse, and $\phi(z)$ is the phase change within the grating.

The equations coupling the two modes are given by [16]

$$\frac{dR}{dz} - i\left[\kappa_{\mathrm{dc}} + \frac{1}{2}\left(\Delta\beta - \frac{d\phi(z)}{dz}\right)\right] R = i\kappa_{\mathrm{ac}} S, \tag{3.1}$$

$$\frac{dS}{dz} + i\left[\kappa_{\mathrm{dc}} + \frac{1}{2}\left(\Delta\beta - \frac{d\phi(z)}{dz}\right)\right] S = -i\kappa_{\mathrm{ac}}^{*} R, \tag{3.2}$$

where κ_{dc} is the dc coupling constant which is a function of the average refractive index $\overline{\Delta n}$ of the grating, and κ_{ac} is the ac coupling constant which is a function of the amplitude Δn of the refractive index variation of the grating. The parameters κ_{dc}, κ_{ac}, and $\Delta\beta$ are defined as

$$\kappa_{\mathrm{dc}} = n\omega\varepsilon_0 \int_{-\infty}^{\infty}\int_{-\infty}^{\infty} \overline{\Delta n}\,\xi_{\mathrm{Rt}}^{*}\xi_{\mathrm{St}}\,dx\,dy, \tag{3.3}$$

$$\begin{aligned} \kappa_{\mathrm{ac}} &= n\omega\varepsilon_0 \int_{-\infty}^{\infty}\int_{-\infty}^{\infty} \frac{\Delta n}{2}\xi_{\mathrm{Rt}}\xi_{\mathrm{St}}^{*}\,dx\,dy, \\ &= \nu\kappa_{\mathrm{dc}}/2, \end{aligned} \tag{3.4}$$

$$\Delta\beta = \beta_{\mathrm{R}} + \beta_{\mathrm{S}} - 2\pi N/\Lambda, \tag{3.5}$$

where n is the refractive index of the fiber, ε_0 is the dielectric constant, ξ_{Rt} and ξ_{St} are the radial transverse field distributions for the forward and backward propagating modes.

In Bragg gratings, the forward and backward propagating modes in the fiber core are the same. Therefore, the overlap integral in Eqs. (3.3) and (3.4) can be approximated by one [16]. The visibility of the fringes in the grating represents the depth of the refractive index variation. If the visibility is equal to one, the amplitude of refractive index variation is maximum. The parameters β_{R} and β_{S} are the propagating constants of the forward and backward propagating modes and N is the order of diffracted UV beam in grating fabrication, which is usually equal to one [16].

In uniform Bragg gratings, the peak amplitude of the refractive index variation Δn, the average refractive index $\overline{\Delta n}$, the period length Λ, and the phase $\phi(z)$ are unchanged over the entire length of the fiber grating. Consequently, $d\phi(z)/dz$ is zero, and the ac and dc coupling coefficients are constant. In such cases, the coupled-mode equations can be solved analytically [Appendix A.8]. The complex reflectivity ρ for a uniform Bragg grating is

$$\rho = \frac{i\kappa_{\mathrm{ac}}^{*}\sinh(\alpha L)}{\alpha\cosh(\alpha L) - i\delta\sinh(\alpha L)}, \tag{3.6}$$

where $\alpha = \sqrt{|\kappa_{\mathrm{ac}}|^2 - \delta^2}$ and $\delta = \kappa_{\mathrm{dc}} + \Delta\beta/2$.

In a non-uniform fiber grating, for example, apodized or chirped fiber grating, the coefficients in the coupled-mode equations vary over the length of the fiber grating. The coupled-mode equations in general cannot be solved analytically. One has to resort to numerical methods.

3.1.3 Numerical Methods

There are many techniques that solve the couple mode equations. Direct numerical integration of the equations is the most straightforward but it is not necessary the fastest.

One of the few that offers complete control of the spatial variation of the refractive index profile is the Rouard's method [44]. It is commonly used in the design of thin-film coatings, but it has been extended by L. A. Weller-Brophy and D. G. Hall [45] for the analysis of diffraction gratings in waveguides. In this method, the waveguide is segmented into subwavelength thin films so that standard thin-film techniques for calculating the transmitted and reflected electric fields can be applied. The Rouard's method can be applied to all grating structure types including linearly and quadratically chirped gratings. The obvious disadvantage of the Rouard's method is that the method is computationally intensive. The computational time is directly proportional to the number of grating elements. It can become very large for long gratings [16].

If the reflective index of a grating is a slowly varying function of the grating length, as in most gratings of interest, a fast and accurate technique called the transfer matrix method [46, 47] can be applied. In the transfer matrix method, one divides a grating into many small segments. The length of each segment can be different. Within each segment, the grating parameters are assumed to be constant but the parameters for different segments are a function of the grating length. In other words, we approximate the continuous variation of the grating parameters with grating length by a piecewise constant function. The approximation for a linearly varying κ_{ac} is shown in Figure 3.3. For each segment, the coupled-mode equations, Eqs. (3.1) and (3.2), are solved analytically. The solutions relate the right going electric fields $R(z)$ to the left going electric fields $S(z)$ through the transfer matrix $[T]$ as given by

$$\begin{bmatrix} R(0) \\ S(0) \end{bmatrix} = [T] \begin{bmatrix} R(L) \\ S(L) \end{bmatrix}, \tag{3.7}$$

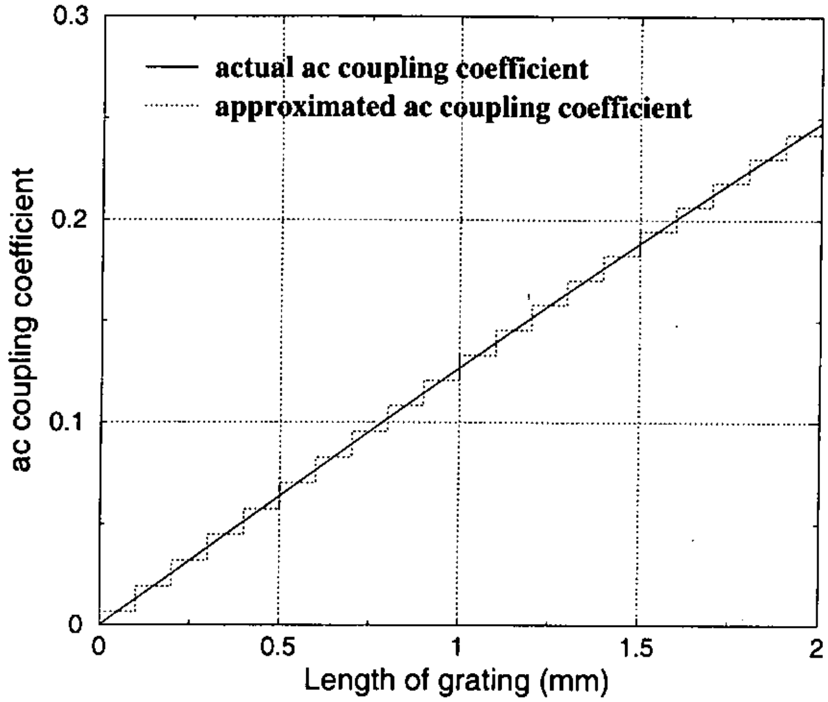

Figure 3.3: Approximation of the ac coupling coefficient in transfer matrix method. The length of each segment is 100 μm.

where

$$
\begin{aligned}
[T(L)] &= \begin{bmatrix} T_{11} & T_{12} \\ T_{21} & T_{22} \end{bmatrix}, \\
&= \begin{bmatrix} \cosh(\alpha L) - i\delta \sinh(\alpha L)/\alpha & i\kappa_{\rm ac} \sinh(\alpha L)/\alpha \\ -i\kappa_{\rm ac}^{*} \sinh(\alpha L)/\alpha & \cosh(\alpha L) + i\delta \sinh(\alpha L)/\alpha \end{bmatrix}, \qquad (3.8)
\end{aligned}
$$

$R(0)$ is the input electric field entering the grating from the left, $S(0)$ is the output field going to the left, $R(L)$ is the output field going to the right, and $S(L)$ is the left going wave entering the grating. The parameter L is the length of grating, $\delta = \kappa_{\rm dc} + (1/2)[\Delta\beta - d\phi(z)/dz]$, $\alpha = \sqrt{|\kappa_{\rm ac}|^2 - \delta^2}$, $\kappa_{\rm dc}$ is dc coupling coefficient, $\Delta\beta$ is the difference between the propagating constants of the forward and backward propagating modes and is given by Eq. (3.5), $\phi(z)$ is the phase change within the grating as a function of the normalized distance z, and κ_{ac} is the ac coupling coefficient. The transfer matrix $[T]$ represents the grating amplitude and phase response. The derivation of the transfer matrix is given in Appendix A.8.

Without loss of generality, the input field from the left can be set to unity, *i.e.*, $R(0) = 1$. Since there is no left going wave entering the grating from the right, we set $S(L) = 0$. The complex reflectivity is therefore given by T_{21}/T_{11} and the complex transmissivity is given by $1/T_{11}$. For uniform Bragg gratings, the result from the transfer matrix method is equivalent to the analytical answer for any length of the grating because $[T(L_1)][T(L_2)] = [T(L_1 + L_2)]$, where $[T(L_1)]$, $[T(L_2)]$, and $[T(L_1 + L_2)]$ are the transfer matrices of the same grating but with length L_1, L_2, and $L_1 + L_2$ respectively [Appendix A.9].

For non-uniform fiber gratings, some precautions are necessary in the application of the transfer matrix method. First, the length of segment δl should be much larger than the period Λ of refractive index variation, *i.e.*, $\delta l \gg \Lambda$ [48], because the transfer matrix method is based on the assumption of slow variation of the mode field over the wavelength of light [16]. On the other hand, the number of segments cannot be too small, otherwise the error due to approximating a continuous function with a piecewise constant function will be large. The minimum number of segments in modeling chirped fiber gratings is given by $2n_{\mathrm{eff}}\Delta\lambda L/\pi\lambda_{\mathrm{B}}^2$ [16], where n_{eff} is the effective index of the fiber core, $\Delta\lambda$ is the reflectivity bandwidth of the chirped fiber grating, L is the length of the grating, and λ_B is the central Bragg wavelength. Finally, the number of the period of refractive index variation within a segment is required to be an integer to maintain the continuity of the refractive index variation over the fiber grating. The transfer matrix $[T(L)]$ in a non-uniform fiber grating is given by

$$\begin{bmatrix} R(0) \\ S(0) \end{bmatrix} = [T] \begin{bmatrix} R(L) \\ S(L) \end{bmatrix}, \tag{3.9}$$

where $[T] = [T_M][T_{M-1}]\cdots[T_1]$, $[T_M]$ is the transfer matrix of the Mth segment counting from the end of grating, and L is the length of the grating.

3.2 Properties of Fiber Bragg Gratings

We focus our study on reflection gratings. The quantity that characterizes a reflection grating is its reflectivity spectrum which determines the reflected power of different spectral components of an input pulse. The wavelength of maximum reflectivity is called the Bragg wavelength at which the forward propagating mode and the backward propagating mode are phase matched [16]. The reflectivity bandwidth is defined as the bandwidth between the first zeroes of the reflectivity spectrum. The phase ϕ of the reflectivity spectrum determines the time delay and the dispersion induced by the reflection grating. Time delay τ for the reflected wave is defined as $d\phi/d\omega$ [48], where ω is the angular frequency. This is analogous to the time delay definition for a forward continuous wave with phase $\phi = \beta z - \omega\tau$ if the Fourier transform is defined as Eq. (1.3), where β is the propagating constant and z is the distance. The dispersion coefficient $D = d\tau/d\lambda$ is the change of time delay among different wavelength λ. In the following, we shall use the transfer matrix method to study the properties of both uniform and non-uniform fiber gratings.

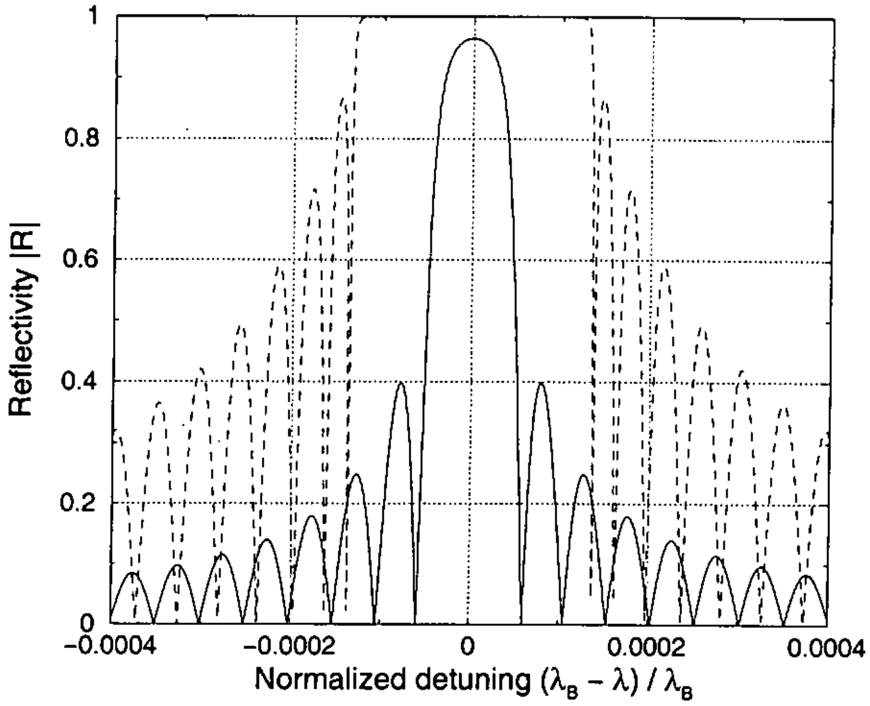

Figure 3.4: Magnitude of the reflectivity versus normalized detuning [16]. Solid line represents a weak grating ($\kappa_{\mathrm{ac}}L = 2$) while dashed line represents a strong grating ($\kappa_{\mathrm{ac}}L = 8$). The effective refractive index is 1.55, the Bragg wavelength is 1.55 μm, and the grating length is 10 mm.

3.2.1 Uniform Bragg Gratings

The simplest type of fiber Bragg gratings is uniform gratings. The parameters of the refractive index variation, such as the period, amplitude, and average refractive index, are constant along the length of the gratings. In this case, the couple mode equations can be solved exactly. Figure 3.4 shows the reflectivity spectra of a strong, $\kappa_{\mathrm{ac}}L = 8$, (dashed line) and a weak, $\kappa_{\mathrm{ac}}L = 2$, (solid line) uniform Bragg gratings. Both of them are 10 mm long. The parameters $\kappa_{\mathrm{ac}} = \pi\Delta n/\lambda_{\mathrm{B}}$ [49] is the ac coupling constant, where Δn is the amplitude of the refractive index variation, L is the grating length, λ_{B} is the Bragg wavelength, and λ is the wavelength of the optical signal. The Bragg wavelength for the

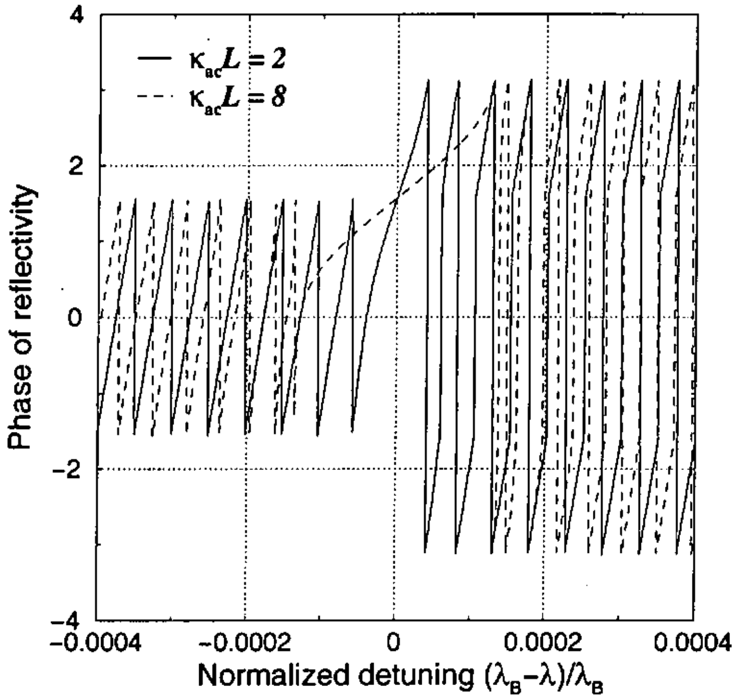

Figure 3.5: Phase of the reflectivity versus normalized detuning. The notation and parameters are the same as that in Figure 3.4.

gratings is 1.55 μm which is slightly smaller than the wavelength at maximum reflectivity, about 1.550395 μm. The shift in the wavelength of the maximum reflectivity is due to the change in the average refractive index. The sidelobes of the reflectivity spectra are caused by the sudden and sharp changes in refractive indices at the beginning and the end of the fiber gratings. From Figure 3.4, a stronger grating has a larger reflectivity bandwidth and higher reflectivity magnitude at the Bragg wavelength. It can be shown that the reflectivity bandwidth narrows as the grating length increases if κ_{ac} is kept unchanged.

In Figure 3.5, we plot the phase of the reflectivity spectra of the same gratings studied in Figure 3.4. The notation is the same as that in Figure 3.4. The phase variation is almost linear near the Bragg wavelength. The discontinuities occur at the zeroes of the reflectivity spectra and also when the phase extends beyond the principle period. The time delay and dispersion characteristics of the two gratings are shown in Figures 3.6 and

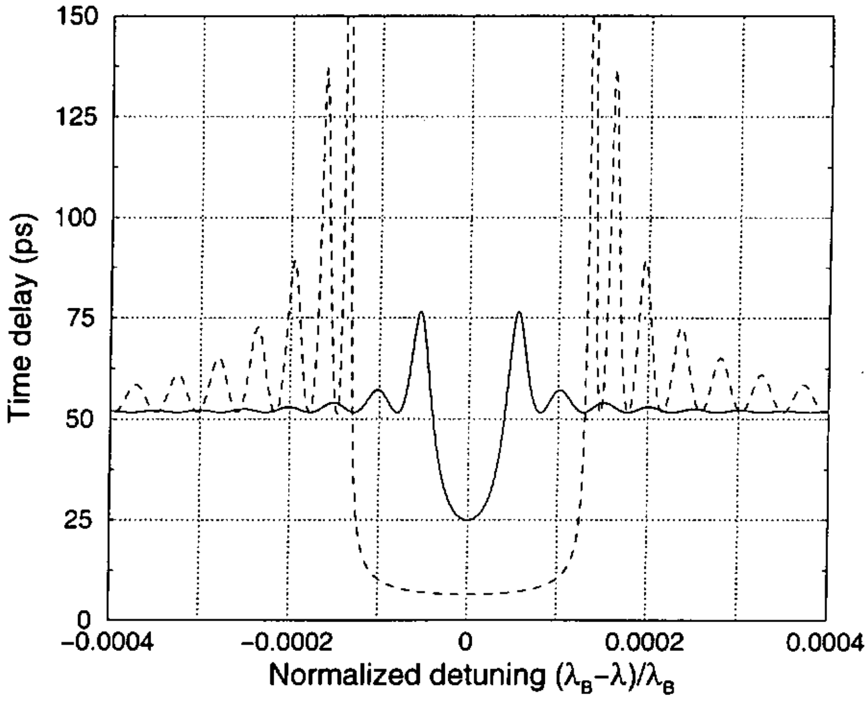

Figure 3.6: Time delay of uniform fiber gratings versus normalized detuning. The notation and parameters are the same as that in Figure 3.4.

3.7 respectively. The time delay τ is given by $-(\lambda^2/2\pi c)d\phi/d\lambda$, where c is the speed of light. From Figure 3.7, the dispersion at the Bragg wavelength is zero and is significant only at the edges of the central reflectivity band. The dispersion values fluctuate inside the sidelobes. From Figure 3.7, the magnitude of the out-of-band dispersion fluctuation is larger for stronger gratings.

Obviously, uniform Bragg gratings in reflection mode are not good dispersion compensating devices. The usable bandwidth of dispersion compensation is very narrow and the third-order dispersion is large. The sidelobes can induce crosstalk between adjacent channels of WDM systems.

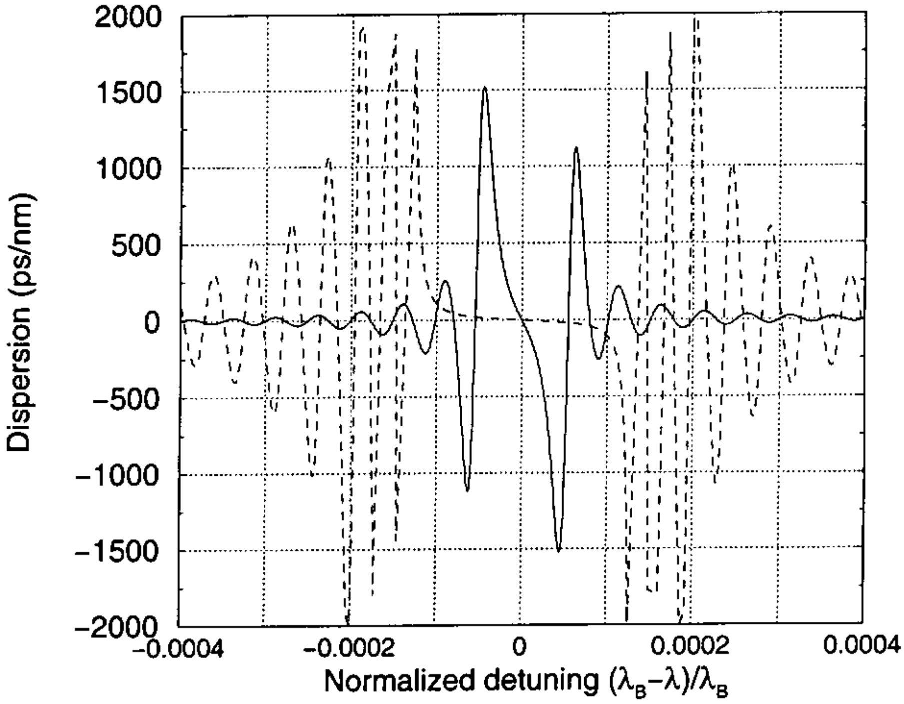

Figure 3.7: Lumped dispersion of uniform fiber gratings versus normalized detuning. The notation and parameters are the same as that in Figure 3.4.

3.2.2 Non-uniform Bragg Gratings

In non-uniform Bragg gratings, the amplitude and/or period of the refractive index fluctuation vary along the length of the fiber gratings, or the phase shifts abruptly in a refractive index variation cycle. Fiber gratings in which the refractive index amplitudes fluctuate are called apodized fiber gratings. Those in which the period of the refractive index fluctuations vary are called chirped fiber gratings.

Apodization [16] is a process that can reduce the sidelobes of the reflectivity spectrum. This process is very important in communication applications of gratings because the sidelobes will induce frequency mixing between the out-of-band frequencies and the central frequency through four-wave mixing. The sidelobes induced crosstalk will limit the channel spacing in DWDM systems.

As the sidelobes are the results of sudden changes in the refractive index at both ends of a grating, a straightforward way to reduce the sidelobes is to smooth the change of the refractive index. One smoothing method is to reduce the power of UV beam at both ends of a grating during fabrication. The key is to ensure that the tail of the refractive index profile at both ends is close to the effective index of the fiber core. The consequence of the unevenly distributed UV power is that sidelobes still appear at one side of the reflectivity spectrum. The Bragg wavelength is also slightly shifted owing to the changing in the average refractive index within the refractive index cycle along the grating.

Alternatively, the remaining sidelobes on one side of the reflectivity spectrum can be removed by exposing the grating twice to diffracted UV beam [16]. After exposing the grating to an apodization profile of UV light as described in the previous paragraph, we expose the grating to UV light again using a lens that has an inversion of the apodization profile used at the first exposure. As a result, the average refractive index along the apodized fiber grating is constant. Only the envelope of the refractive index amplitude is changing as shown in Figure 3.8. This process can remove all the sidelobes beyond the reflectivity bandwidth. Similar to uniform gratings, apodized gratings induce different time delay at different spectral components and the dispersion at the carrier frequency is zero. While apodization can remove sidelobes in the reflectivity spectrum, it does not affect the dispersion property of the gratings.

Chirped Fiber Gratings

In a chirped fiber grating, the period of the refractive index varies along the length of the grating [16]. Consequently, a range of Bragg wavelengths can be reflected. Recall

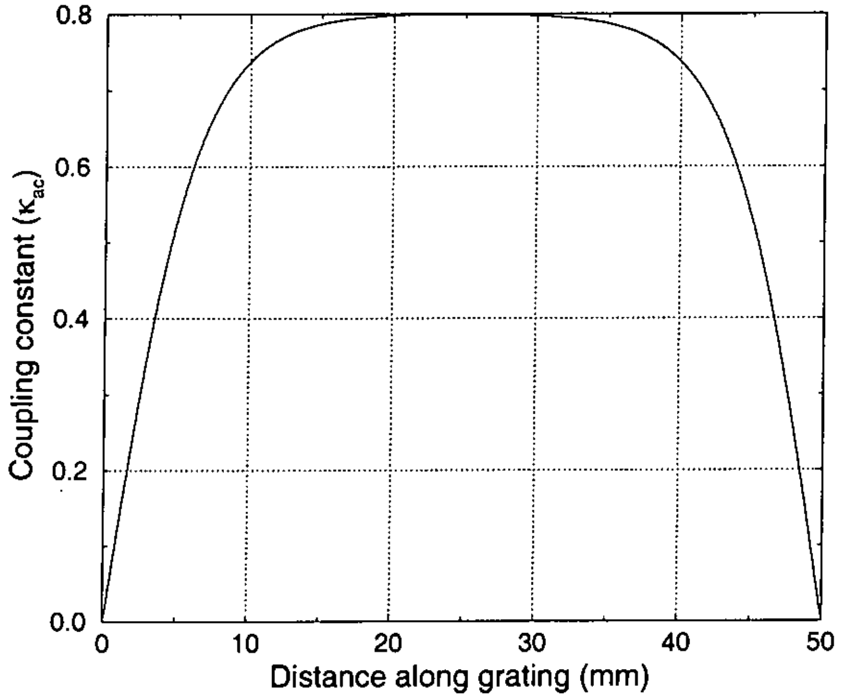

Figure 3.8: Apodization profile of a positive hyperbolic tangent function, $\kappa_{ac}(z) = \check{\kappa}_{ac}\tanh(8|z|/L)$ for $z \leq L/2$ and $\kappa_{ac}(z) = \check{\kappa}_{ac}\tanh(8|L-z|/L)$ for $z > L/2$, where $\check{\kappa}_{ac} = 0.8$ is maximum coupling coefficient of apodization profile and L=50 mm is grating length. The coupling coefficient κ_{ac} is proportional to the amplitude of refractive index fluctuation.

that the Bragg wavelength is proportional to the period of the refractive index in the grating. The variation in the reflective index period allows different Bragg wavelengths to be reflected at different locations of the grating. Thus the different Bragg wavelengths have different time delay. Pulse compression can be achieved by giving more time delay to shorter wavelength and less time delay to longer wavelength for propagation in normal dispersion fiber. So, decreasing the period of refractive index in the grating at the pulse input end will result in a large lumped normal dispersion. The reflectivity, time delay and dispersion of an unapodized chirped fiber grating are shown in Figures 3.9, 3.10 and 3.11 respectively. The length of the chirped grating is 50 mm. The rate of change of the period [48] is given by

$$\frac{d\phi}{dz} = 2F\left(\frac{z - L/2}{L^2}\right),$$

where ϕ is the phase of refractive index fluctuation, and z is the distance from the pulse input end of the grating. We let $z = 0$ at the pulse input end and $z = L$ at the other end of the grating. The parameter F is called the chirp parameter and $F = 600$ in the Figures 3.9, 3.10, and 3.11. The Bragg wavelength at the mid-point of the grating is 1.55 μm and the shift of maximum reflectivity wavelength is the same as that in uniform Bragg gratings. The maximum wavelength of reflectivity is obtained by setting $\kappa_{\mathrm{dc}} = -\Delta\beta/2$, where $\Delta\beta = 2\beta - 2\pi/\Lambda$ is the difference in the propagation constants between the forward propagating wave and the reflected wave. In the phase matching case, $\kappa_{\mathrm{dc}} = 2\kappa_{\mathrm{ac}} = 2n\Delta n/\lambda_{\mathrm{B}}$. The value of $\kappa_{\mathrm{dc}} = 1.6$, $n_{\mathrm{eff}} = 1.55$, and $\Lambda = \lambda_{\mathrm{B}}/2n_{\mathrm{eff}} = 5 \times 10^{-4}$ mm. The wavelength of maximum reflectivity is 1.5504 μm.

The fluctuation of the reflectivity outside the main reflection band is due to the sudden change of the refractive index at both ends of the grating. The change in the refractive

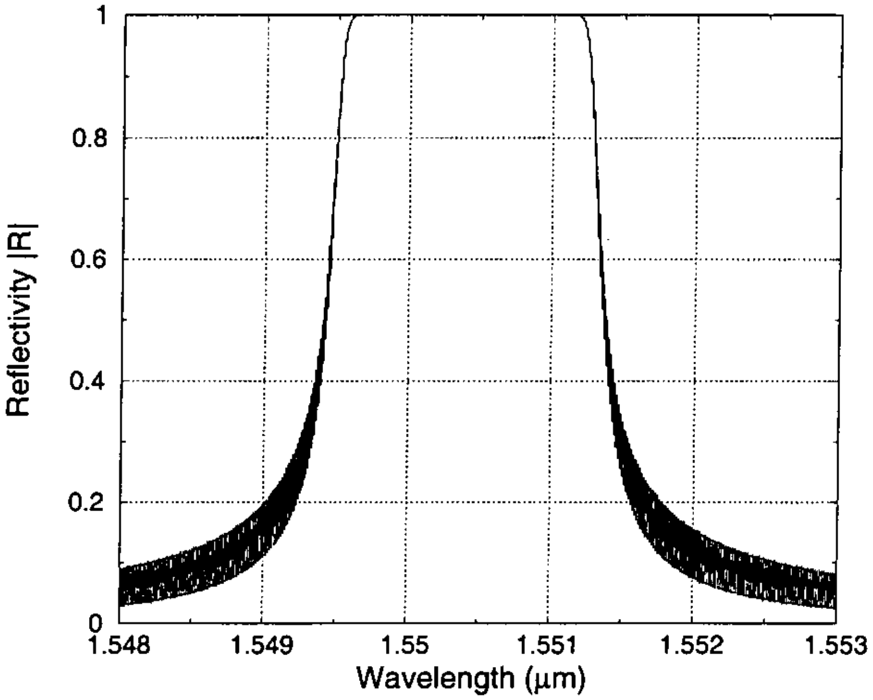

Figure 3.9: Reflectivity spectrum versus the wavelength of the signal in an unapodized chirped fiber grating. The grating length is 50 mm. The chirp parameter F is 600, the effective index is 1.55, the dc coupling coefficient is 1.6, and the period of refractive index fluctuation is 5×10^{-4} mm. The Bragg wavelength is shifted from 1.55 μm to near 1.5504 μm due to the change in average refractive index $\overline{\Delta n}$. The segment length used in the transfer matrix method is 0.1 mm.

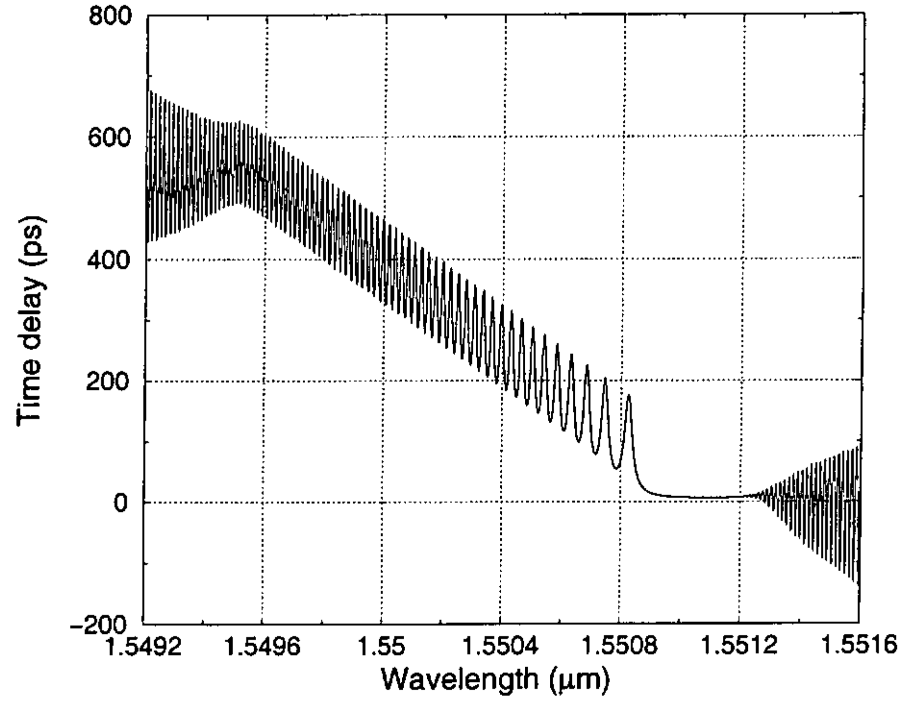

Figure 3.10: Time delay in an unapodized chirped fiber grating as a function of wavelength. The parameters are the same as that in Figure 3.9.

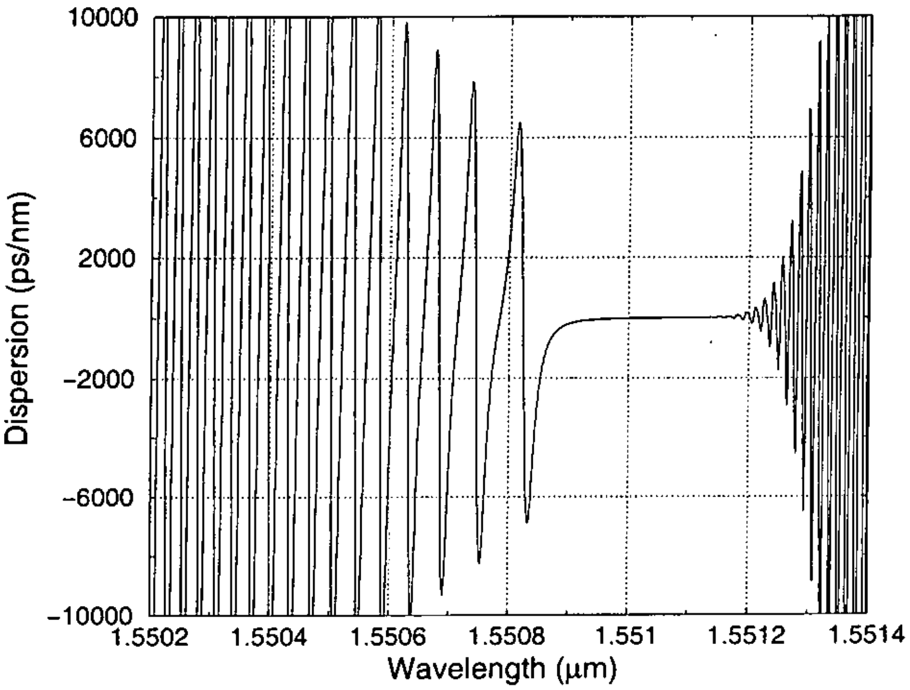

Figure 3.11: Lumped dispersion in an unapodized chirped fiber grating as a function of wavelength. The parameters are the same as that in Figure 3.9.

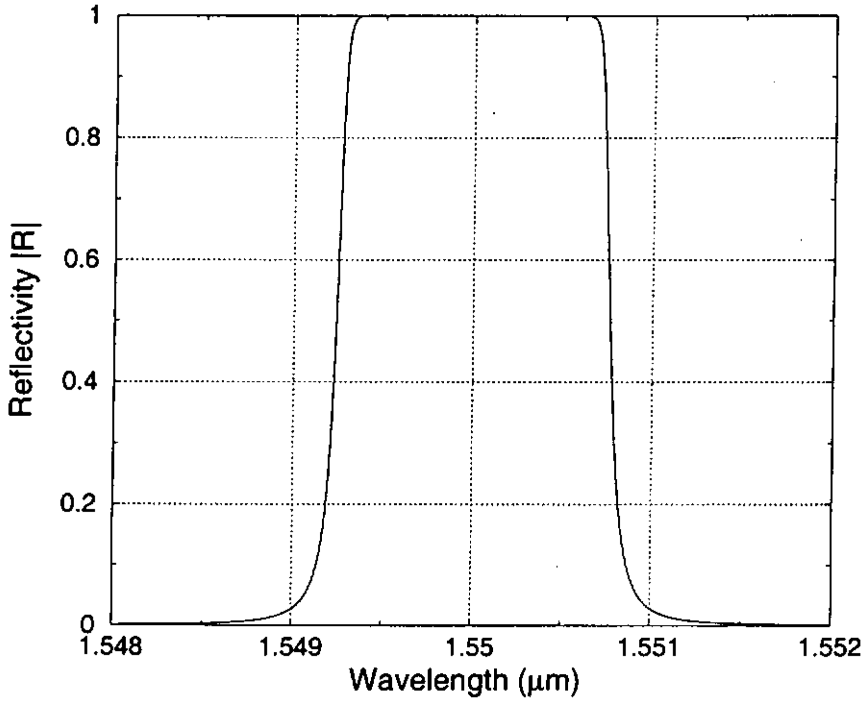

Figure 3.12: Reflectivity versus wavelength in a chirped fiber grating which use a positive hyperbolic tangent apodization profile. The segment length used in the transfer matrix method is 0.1 mm. The parameters are the same as that in Figure 3.9.

index at both ends also induces fluctuation in the time delay because of the multiple reflections within the grating [16]. The large magnitude of time delay variation will result in large magnitude of dispersion variation which can significantly affect the signal spectrum [51, 52]. Apodization and long grating length can solve the problems of chirped fiber gratings. Figures 3.12, 3.13, and 3.14 show the reflectivity, time delay, and dispersion spectrum of a chirped fiber grating. The parameters of the chirped grating is the same as that used in Figures 3.9, 3.10, and 3.11, except that the grating is now apodized by the profile function shown in Figure 3.8. The average refractive index is equal to the effective index of the fiber core. There are substantial improvements in the reflectivity spectrum and time delay ripples. The average dispersion value within the wavelength range from 1.54968 μm to 1.55032 μm is -378.959 ps/nm. The amplitude of dispersion fluctuation

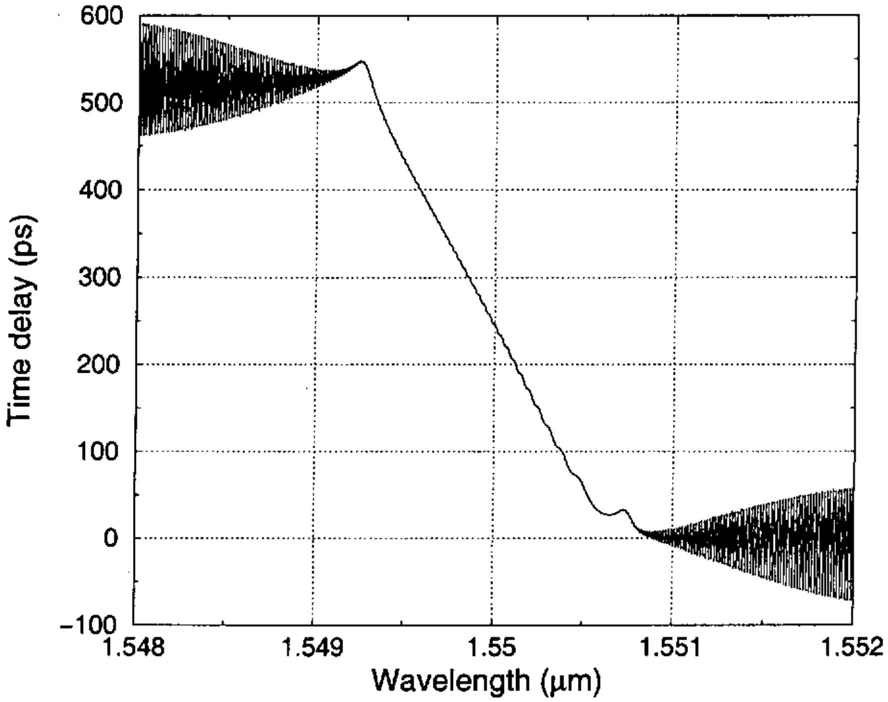

Figure 3.13: Time delay variation in an apodized chirped fiber grating as a function of wavelength. The parameters are the same as that in Figure 3.12.

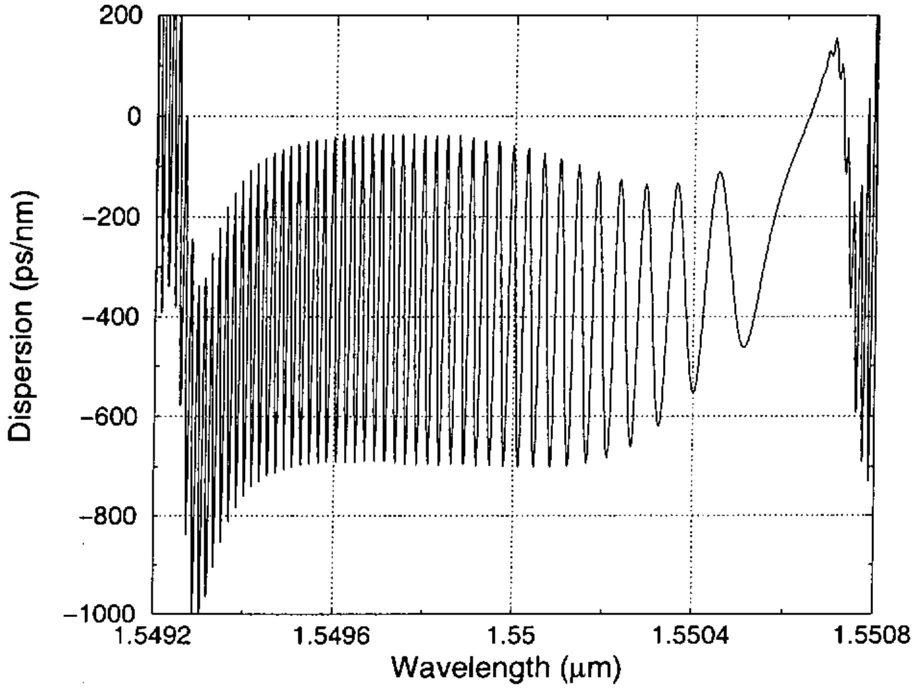

Figure 3.14: Lumped dispersion in an apodized chirped fiber grating as a function of wavelength. The average dispersion is about −378.959 ps/nm. The parameters are the same as that in Figure 3.12.

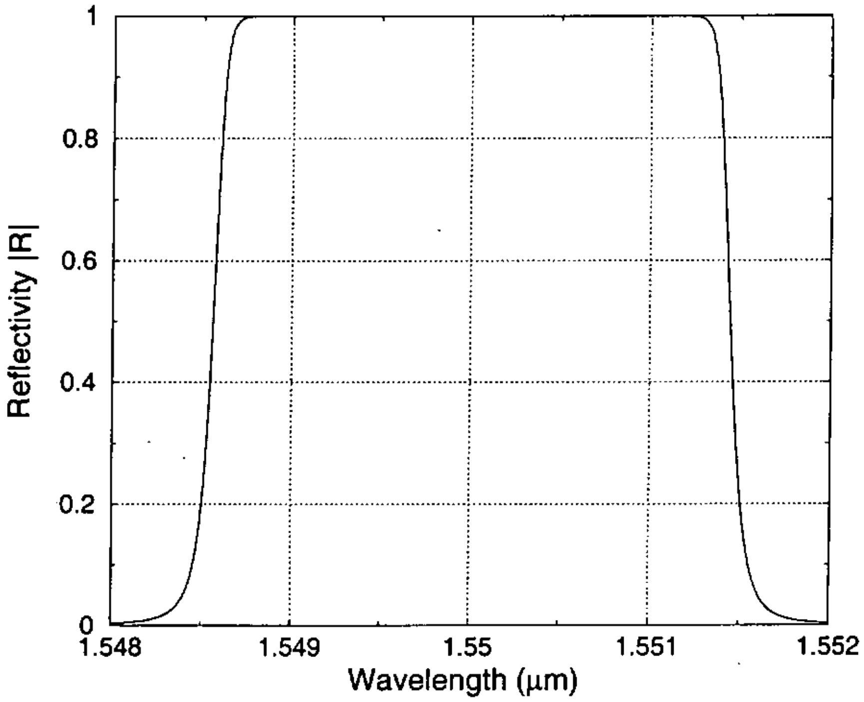

Figure 3.15: Reflectivity versus wavelength of a chirped fiber grating. The grating length is 100 mm, the chirp parameter F is 2,400, and the maximum κ_{ac} is 0.8. The segment length used in the transfer matrix method is 0.1 mm.

is about 320 ps/nm at the central frequency.

The amplitude of the time delay ripples and dispersion fluctuation can be reduced by increasing the length of the apodized gratings. A long grating will have the additional benefit of a broader reflectivity bandwidth. The reflectivity spectrum of a grating with twice the length, *i.e.*, 100 mm, is shown in Figure 3.15. The chirp parameter F is chosen to be 2,400 because the chirp parameter is approximately proportional to the square of the grating length [49]. The time delay and dispersion spectrum of the grating is shown in Figures 3.16 and 3.17 respectively. The reflection bandwidth is double and the amplitude of the time delay ripples is smaller when compared to that of Figure 3.13. The mean amplitude of the dispersion fluctuation over the reflectivity bandwidth is reduced to about 150 ps/nm from about 320 ps/nm.

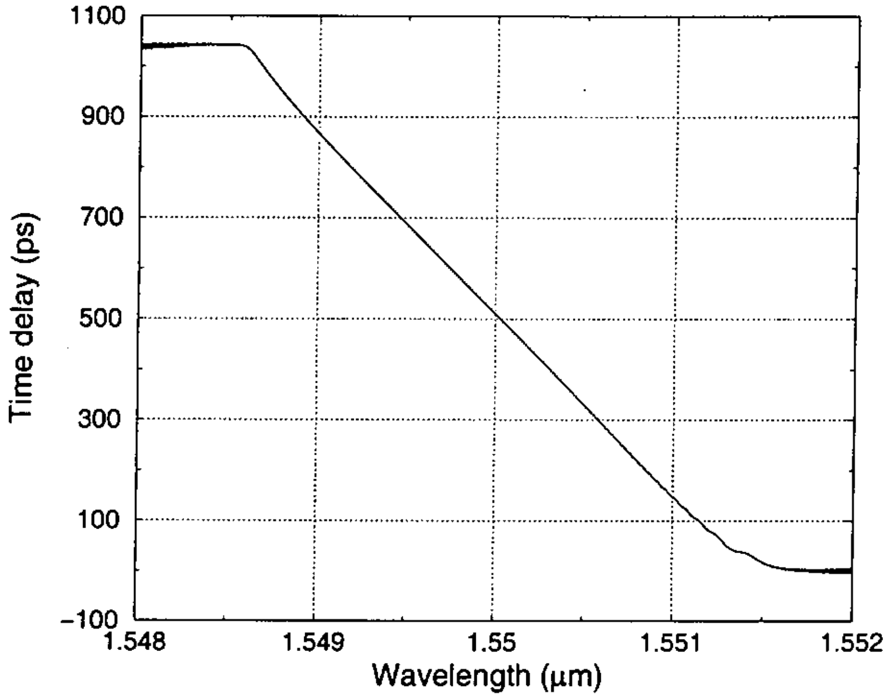

Figure 3.16: Time delay versus wavelength of the grating discussed in Figure 3.15.

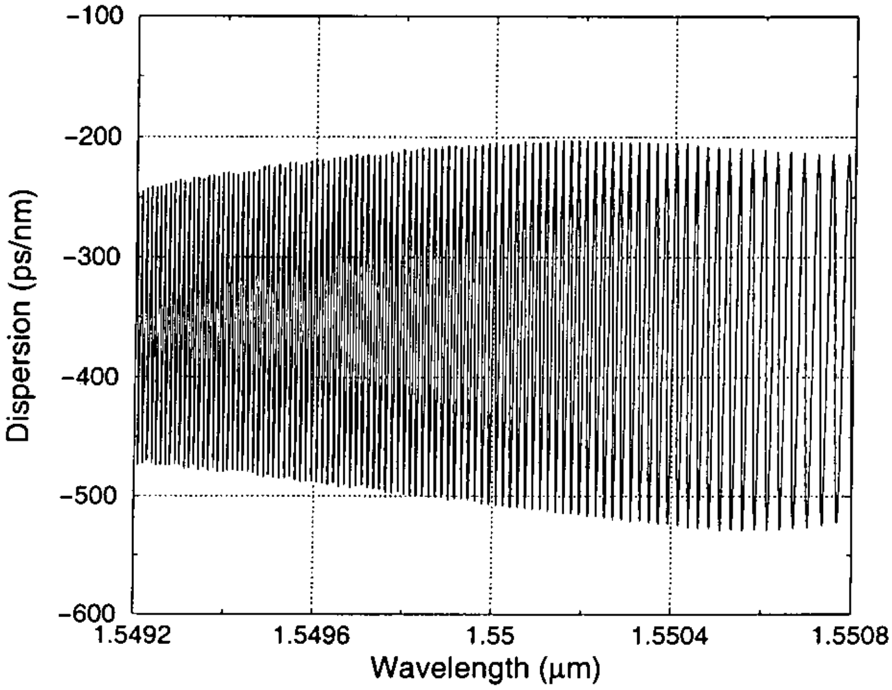

Figure 3.17: Lumped dispersion versus wavelength of the grating discussed in Figure 3.15. The mean lumped dispersion is about −320 ps/nm.

By increasing the grating length, the dispersion of the chirped gratings can be made nearly constant and thus can be used to compensate for the dispersion of optical fibers. Chirped fiber gratings can also compensate third-order dispersion by combining a parabolic shape of time delay on a slanted straight line [19, 50]. This results in a linear dispersion variation across the reflectivity bandwidth.

The length of a grating is negligible when compared to that of dispersion-compensating fibers (DCF), a feature that makes modifications to system configurations and storage of system devices much easier. An additional advantage of gratings over DCFs as dispersion compensation devices is that the reflectivity spectrum can be used as a filter to remove crosstalk in WDM systems. Chirped fiber gratings are not without drawbacks, however. The dispersion outside of the reflectivity bandwidth is large in amplitude and rapidly fluctuating which will affect the performance of DWDM systems using cascaded chirped fiber gratings for dispersion compensation.

3.3 Solitons in Dispersion Managed Systems using Ideal Gratings

In this Section, we study dispersion managed systems using chirped fiber gratings for dispersion compensation. We assume that the grating is an ideal compensator such that there is no dispersion fluctuation and the reflectivity bandwidth of the grating is much larger than the signal bandwidth. The grating is then modeled by Eq. (1.1). The effect of the grating on an input pulse is given by

$$\tilde{q}_{\rm out}(z,\omega) = \tilde{q}_{\rm in}(z,\omega)\exp(iD_{\rm g}\omega^2/2), \tag{3.10}$$

where $\tilde{q}_{\text{out}}(z,\omega)$ is spectrum of the output from the chirped fiber grating, $\tilde{q}_{\text{in}}(z,\omega)$ is the spectrum of the input pulse, and D_g is the lumped dispersion of the grating. The derivation of the above equation is based on the solutions of Eq. (1.1).

The equation governing the pulse propagation in a dispersion managed systems utilizing fiber Bragg gratings for dispersion compensation is given in normalized units by

$$i\frac{\partial q}{\partial z} - \left[\frac{f(z)}{2}\right]\frac{\partial^2 q}{\partial t^2} + |q|^2 q = 0, \tag{3.11}$$

where $f(z)$ is a constant with periodic compensation carried out as described in Eq. (3.10). We apply the numerical averaging method discussed in Chapter 2 and find that periodic numerical solutions indeed exist in grating compensated dispersion managed systems.

We choose a dispersion map in which the normalized dispersion coefficient of the anomalous fiber is −81 which corresponds to −8.1 ps^2/km. The normalized fiber length is 0.0777 which corresponds to 100 km when the average dispersion is −0.1 ps^2/km and the time normalization constant is (20/1.763) ps. The dispersion length is 1,287.3 km. The normalized lumped grating dispersion is 6.216 which corresponds to 800 ps^2 in real world units.

The DM system starts from the mid-point of the anomalous fiber segment. Figures 3.18 and 3.19 show the chirp-width dynamics and the pulse width at the end of each map as a function of distance. The initial pulse is $3.5\,\text{sech}(t)$. In the chirp-width plane, the motion converges to a fixed point indicating the existence of a periodic solution. Figure 3.19 shows that the pulse width is constant after $z = 20$. Similar to DM systems using DCF, the pulse at the mid-point of the anomalous dispersion fiber is chirp free. The chirp is the largest just before and just after the grating. The minimum normalized pulse width of the DM soliton is 1.93 at the mid-point of the anomalous dispersion fiber. The maximum

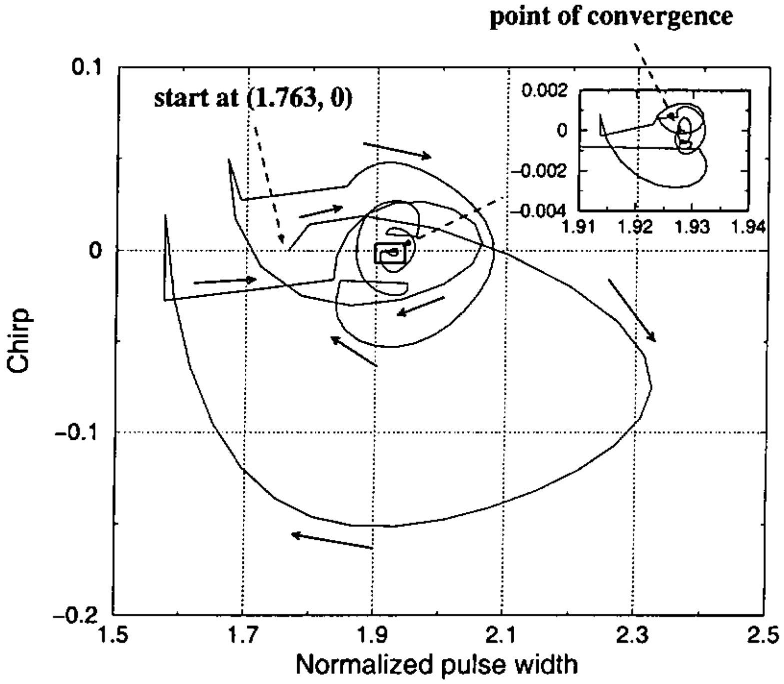

Figure 3.18: Chirp-width dynamics. The chirp and pulse width are taken at the end of each map. The initial pulse is 3.5 sech(t). The averaging distance is 1,000 dispersion maps. The map length is 100 km, the dispersion coefficient of the fiber is -8.1 ps^2/km, and the average dispersion coefficient is -0.1 ps^2/km.

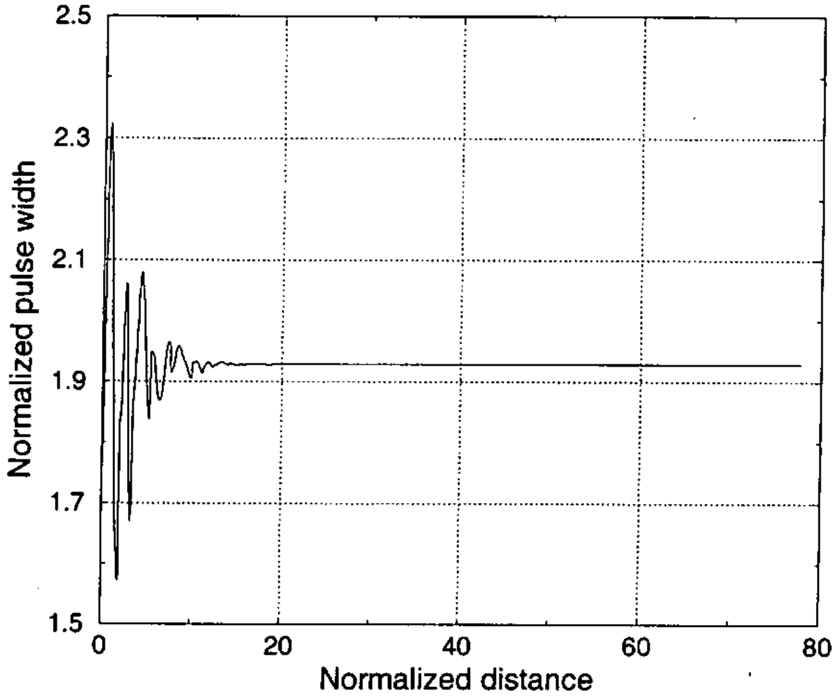

Figure 3.19: FWHM at the end of each map as a function of distance. The parameters are the same as that in Figure 3.18.

normalized pulse width is 4.48571 at the input and output of the grating. The chirp-width dynamics within a dispersion map is shown in Figure 3.20. The crosses represent numerical results. The pulse width variation in 5 dispersion map distance is shown in Figure 3.21.

In Figure 3.20, the evolution starts on the horizontal axis. The chirp as well as the pulse width increases as the pulse propagates along the anomalous dispersion fiber. The grating reverses the sign of the chirp parameter without changing its magnitude. The chirp and the width then return to their initial values along a path that is a mirror image of the first half of its evolution.

The averaging is taken for 1,000 dispersion maps. The pulse is then propagated for 100 dispersion maps to check the stability of the solution. The maximum amplitude difference between the initial pulse and the final pulse is 10^{-9}. The pulse amplitude in the time

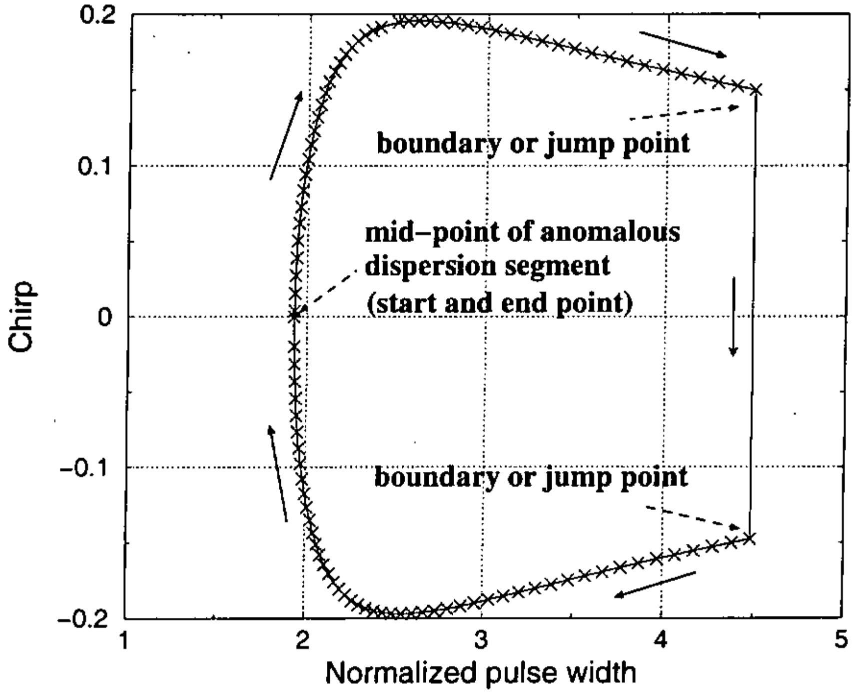

Figure 3.20: Chirp-width dynamics within a dispersion map. The soliton obtained from numerical averaging method is propagated for 100 dispersion maps. The figure shows the variation at the 100th dispersion map. The crosses represent the data point within the map. The parameters are the same as that in Figure 3.18.

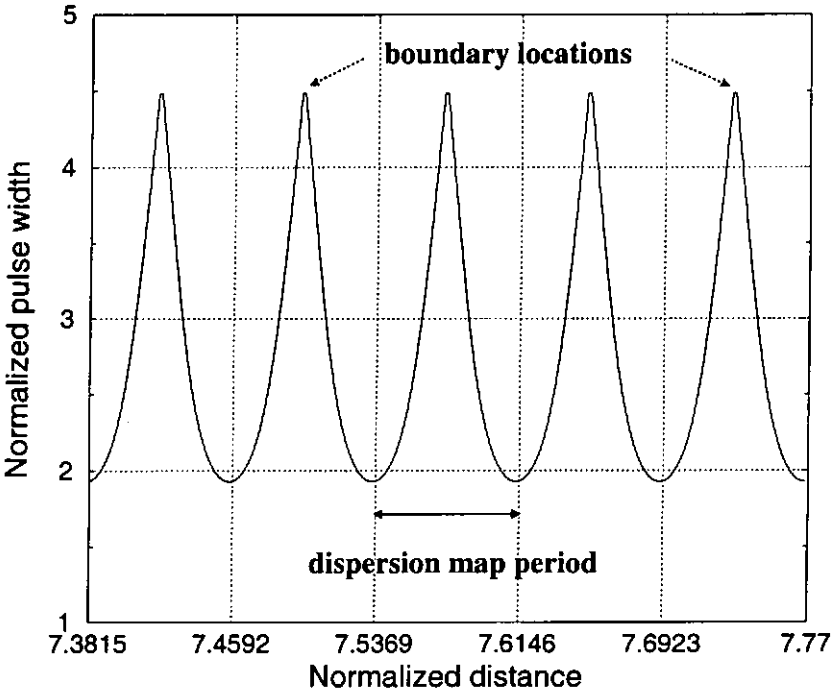

Figure 3.21: Variation of the FWHM of the soliton for 5 dispersion maps. The parameters are the same as that in Figure 3.18.

domain and the frequency domain is shown in Figures 3.22 and 3.23 respectively. The solid line represents the pulse at the mid-point of the anomalous dispersion fiber and the dotted line is taken at boundary location. The spikes of pulse spectrum in Figure 3.23 are due to numerical errors of the split-step Fourier method [39] and it can be reduced by decreasing the step size.

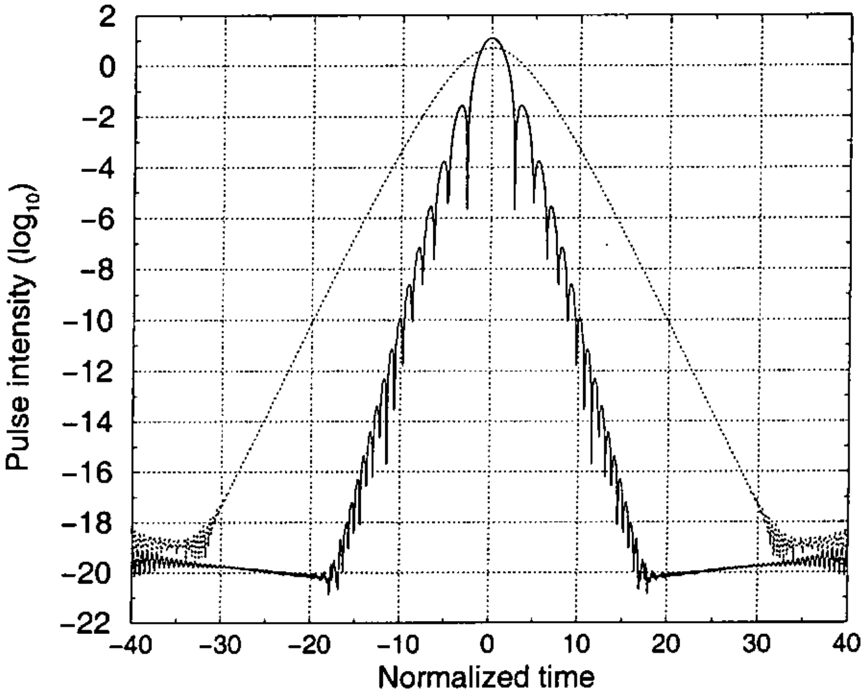

Figure 3.22: Intensity-time plot of the DM soliton. Solid line represents the pulse profile at the mid-point of the anomalous dispersion fiber and dotted line represents that before and after the grating. The parameters are the same as that in Figure 3.18.

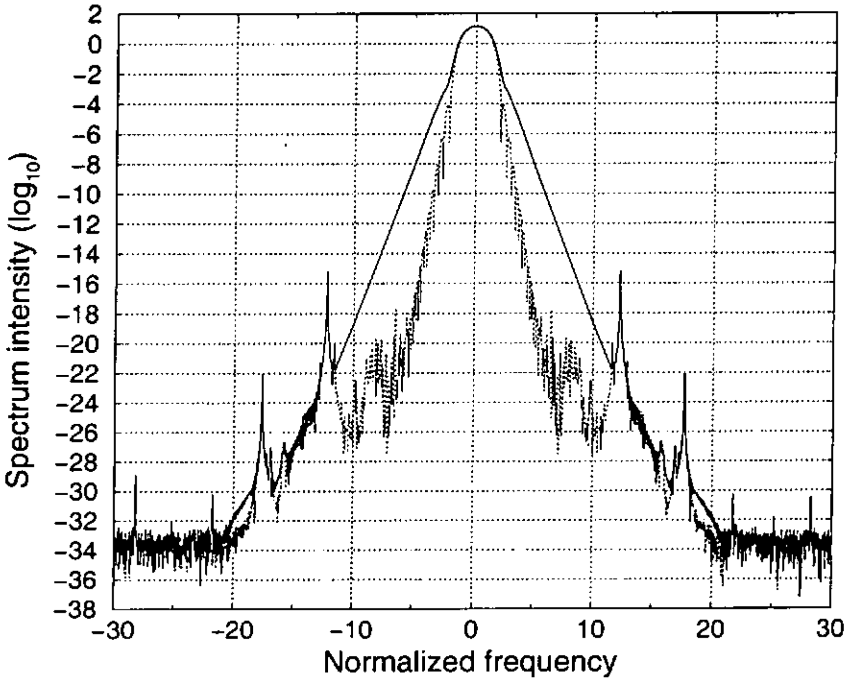

Figure 3.23: The spectra of the DM soliton shown in Figure 3.22.

Chapter 4

Design of Dispersion Maps

4.1 Introduction

In Chapter 2, we discuss dispersion managed soliton systems using dispersion compensating fibers (DCFs). DM solitons have many advantages over conventional solitons, one of which is the energy enhancement. The higher energy required to launch a soliton in a DM system when compared to a conventional soliton system with the same average dispersion and pulse width results in a higher signal-to-noise ratio. In Chapter 3, we discuss DM systems using in-line fiber Bragg gratings (FBGs) for dispersion compensation and we show that solitons can also propagate in these systems. For the purpose of dispersion compensation, a fiber Bragg grating can be considered as a DCF with zero length and a lumped dispersion.

The design of a dispersion map for a dense wavelength division multiplexing system is a multi-parameter optimization problem. The overall performance of the system is determined by the bit error rate (BER) which is affected by a large number of factors including the Gordon-Haus timing jitters [36], collisional induced timing jitters [27], polarization effects [4], *etc.* Energy enhancement is an important property that determines the choice of dispersion managed systems. N. J. Doran *et al.* [11] gave an empirical formula of the energy enhancement as a function of the map strength and map depth for two-step dispersion maps in which the two pieces of fibers are of equal length. There are indications that dispersion maps consist of mostly normal dispersion fibers have higher energy enhancement than that of equal length maps [15]. To our knowledge, a comprehensive study on the dependence of energy enhancement on the ratio of the lengths of the two fiber segments has not been carried out. In Section 4.2, we compare the energy enhancement of dispersion managed systems using DCFs with different fiber length ratio. The average dispersion is chosen to be anomalous. We show that for a dispersion map with a fixed map length, average dispersion, and cumulated absolute dispersion, the energy enhancement increases when the length of the normal dispersion fiber segment increases. The energy enhancement reaches a maximum when the length of the anomalous dispersion segment is zero. Dispersion compensation in this case is carried out by FBGs. On the other hand, if the length of the normal dispersion fiber decreases, the energy enhancement decreases and reaches a minimum when its length becomes zero. In Section 4.3, we repeat the study for DM systems with zero average and normal average dispersion. The results are qualitatively similar to that of Section 4.2. Similar to DCF compensated systems, DM solitons in FBG compensated systems exist for zero average dispersion and normal average dispersion. In Section 4.4, we discuss design issues in DM soliton systems.

4.2 Anomalous Average Dispersion

In a conventional soliton system, the energy of a soliton depends on the GVD coefficient, the Kerr coefficient, and the pulse width. Since the Kerr coefficient does not change in a fiber, when the GVD coefficient and the pulse width are specified, one can determine the energy of the soliton. In a DM system using a two-step dispersion map, the soliton energy depends on the pulse width and the dispersion map parameters, *i.e.*, the dispersion coefficients $\ddot{\beta}_i$ and the lengths l_i, $i = 1, 2$, of each fiber segment. One can characterize a two-step dispersion map using another set of parameters. They are the map length L, the fraction of the first fiber segment length to the map length R, the average dispersion coefficient $\ddot{\beta}_{\mathrm{av}}$, and the cumulated absolute dispersion γ. The relationship between the two sets of parameters are

$$\begin{aligned} L &= l_1 + l_2, \\ R &= l_1/L, \\ \ddot{\beta}_{\mathrm{av}} &= \left(l_1\ddot{\beta}_1 + l_2\ddot{\beta}_2\right)/L, \qquad (4.1) \\ \gamma &= l_1|\ddot{\beta}_1 - \ddot{\beta}_{\mathrm{av}}| + l_2|\ddot{\beta}_2 - \ddot{\beta}_{\mathrm{av}}|. \end{aligned}$$

The energy enhancement for a equal length two-step map DM system, *i.e.*, $l_1 = l_2$, is shown to depend on the map strength $S = \gamma/\tau^2$ and map depth $\delta = (|\ddot{\beta}_1| + |\ddot{\beta}_2|)/|\ddot{\beta}_{\mathrm{av}}|$ [11] only, where τ is the minimum pulse width within a dispersion map. In the following, we study the dependence of the energy enhancement on the length ratio R when the parameters L, $\ddot{\beta}_{\mathrm{av}}$, and γ are fixed. We note that when the lengths of the fiber segments vary, the cumulated absolute deviation from the average dispersion in each segment $l_i|\ddot{\beta}_i - \ddot{\beta}_{\mathrm{av}}| = l_1 l_2|\ddot{\beta}_1 - \ddot{\beta}_2|/L$, $i = 1, 2$, remains constant. For each length ratio R, we find the

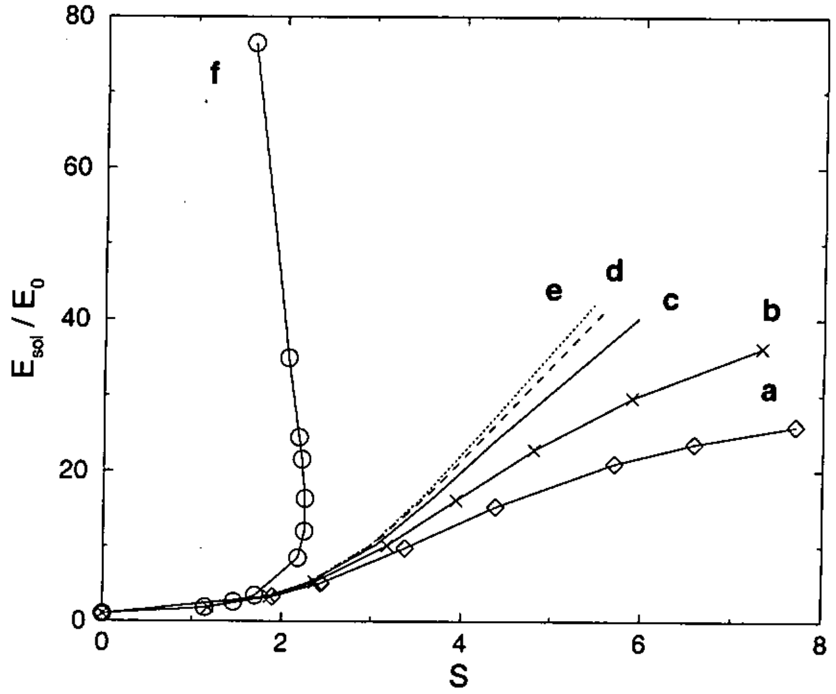

Figure 4.1: Energy enhancement versus map strength S for different values of length ratio R. Curve a (diamonds), b (crosses), c (solid line), d (dashed line), e (dotted line), and f (circles) represent $R = 0, 0.5, 0.8, 0.9, 0.95$, and 1 respectively. Each data point corresponds to a different pulse energy. The map length L is 200 km, the average dispersion $\ddot{\beta}_{\text{av}}$ is -0.1 ps^2/km, and the cumulated absolute dispersion γ is $1,600$ ps^2 in all curves. E_{sol} is the energy of the DM solitons and E_0 is the energy of the fundamental soliton with the same average dispersion and pulse width as the DM soliton.

DM soliton solutions by solving Eqs. (2.1) and (2.2) and applying the numerical averaging technique discussed in Section 2.2.1. Energy enhancement depends on the map strength, γ/τ^2, and the pulse width τ related to pulse energy. We vary the input pulse energy in order to obtain different values of map strength. The process is then repeated for different values of R. The energy enhancement for different values of R are shown in Figure 4.1. The map length L is 200 km, the average dispersion coefficient $\ddot{\beta}_{\text{av}} = -0.1$ ps^2/km and the cumulated absolute dispersion value in a dispersion map γ is 1,600 ps^2. The results are qualitative the same for other choices of the parameters L, γ, and $\ddot{\beta}_{\rm av} < 0$. In the following, we have chosen $\ddot{\beta}_1 > 0$ and $\ddot{\beta}_2 < 0$. Therefore, l_1 is the length of the normal dispersion fiber segment and l_2 is the length of the anomalous dispersion fiber segment. The length ratio R varies from 0 to 1 corresponding to DM systems with only anomalous dispersion fibers and only normal dispersion fibers respectively. The results shown in Figure 4.1 are obtained using the following numerical parameters: $\Delta z = 7.8 \times 10^{-4}$, number of points in time axis = 4,096 or 8,192, computation window size = 1,800 ps or 6,500 ps. The propagation distance is 100,000 km (500 dispersion maps). The numerical error in the pulse amplitude in the time domain is 10^{-8} to 10^{-6}. The initial pulse width is 20 ps.

In Figure 4.1, the curves labeled a (diamonds), b (crosses), c (solid line), d (dashed line), e (dotted line), and f (circles) correspond to R = 0, 0.5, 0.8, 0.9, 0.95, and 1 respectively. We observed that the energy enhancement versus map strength curve for R = 1, *i.e.,* a dispersion map consisting of normal dispersion fibers and a FBG for dispersion compensation, is different from that of other values of R. Recall that the minimum pulse width in a dispersion map is used in the calculation of the energy enhancement and the map strength. For a DM soliton, the pulse width reaches the minimum at the mid-point of the anomalous dispersion fiber and the maximum at the junction of the two fibers as shown in Figure 2.4. In other words, the pulse width changes from the minimum value to maximum the value and back to the minimum value when it propagates through the anomalous dispersion fiber segment. As R increases from 0 to 1, the length of the anomalous dispersion segment decreases but the GVD coefficient increases such that the absolute cumulated deviation from the average dispersion, $l_2|\ddot{\beta}_2 - \ddot{\beta}_{\rm av}|$, in that segment remains constant. The pulse goes through similar variations from the minimum value to the maximum value and back to the minimum value inside the shortening anomalous dispersion fiber. When a fiber grating is used in place of the DCF for the $R = 1$ case, the pulse width inside the anomalous dispersion portion of the map is not available. Only the pulse widths before and after the fiber grating can be measured as shown in Figure 3.21. The grating reverses the sign of the chirp coefficient but does not affect the pulse width. As a result, in a grating compensated dispersion map, the apparent minimum pulse width is at the mid-point of the normal dispersion fiber. If this pulse width is used to calculate the energy enhancement and map strength, we obtain curve f in Figure 4.1. The apparent "shift" of the energy enhancement versus map strength curve at $R = 1$ when compared to that of other values of R is therefore due to the change in the location where the minimum pulse width is measured, *i.e.*, from the mid-point of the anomalous dispersion fiber to the mid-point of the normal dispersion fiber. As seen in Figure 4.2, the shift cannot be removed by plotting DM soliton energy instead of the energy enhancement because the map strength also depends on the pulse width. If the pulse width at the mid-point of the normal dispersion fiber is used, the curves converge smoothly to the $R = 1$ case as seen in Figure 4.3. There are two energy enhancement for the same map strength in Figure 4.3 because two DM solitons with different energy can have the same pulse width at the mid-point of the normal dispersion fiber as shown in Figure 4.4. However, the $R = 0$ case is not defined then. The ambiguity lies in the definition of the pulse width inside a zero length fiber segment, *i.e.*, the fiber grating. For discussion purpose, it is better to use the limit of the minimum pulse widths of DCF compensated DM systems when the length of the anomalous dispersion fiber segment decreases to zero as the minimum pulse width of

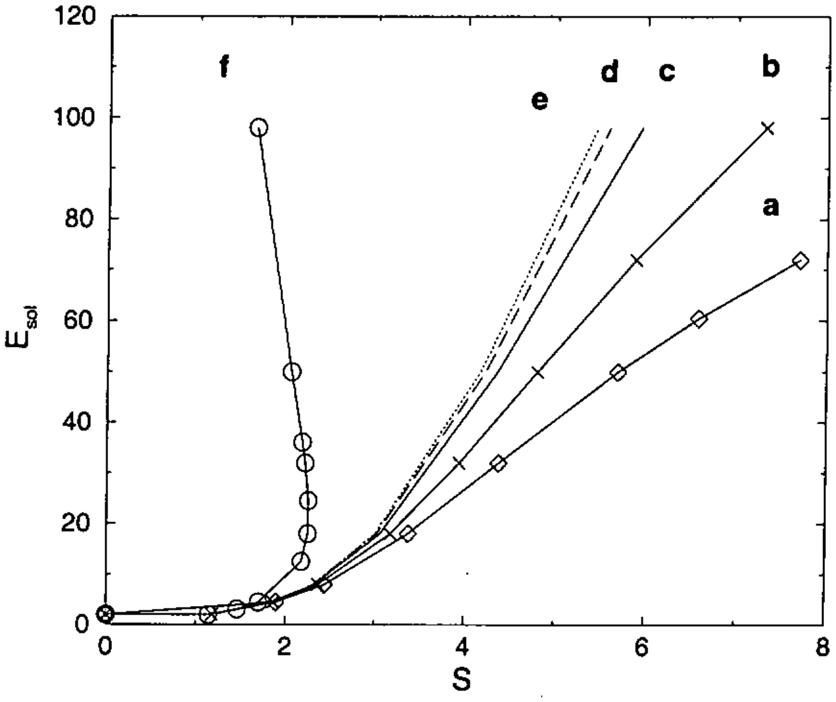

Figure 4.2: Normalized pulse energy E_{sol} versus map strength S for different values of length ratio R. The parameters and notation are the same as that in Figure 4.1.

grating compensated DM systems.

Figure 4.1 shows that the energy enhancement for different values of R increases as the map strength increases. For $S < 3$, the energy enhancement are almost the same for all values of length ratio. When the map strength increases beyond 3, the energy enhancement for dispersion maps with larger proportion of normal dispersion fiber increases faster. Figure 4.5 shows the dependence of the DM soliton energy as a function of R for different values of the map strength. As γ is fixed, each map strength corresponds to a pulse width. So, the fundamental soliton energy E_0 is the same in each of the curve in Figure 4.5. In all cases, the energy enhancement is minimum at $R = 0$ and maximum at $R = 1$. That is, grating compensated DM systems form the upper and lower limit of the energy enhancement when L, $\ddot{\beta}_{\text{av}}$, and γ are fixed. For $S = 3$, the increase in DM soliton energy is very small, but for $S = 5$, the DM soliton energy of a DM map made up

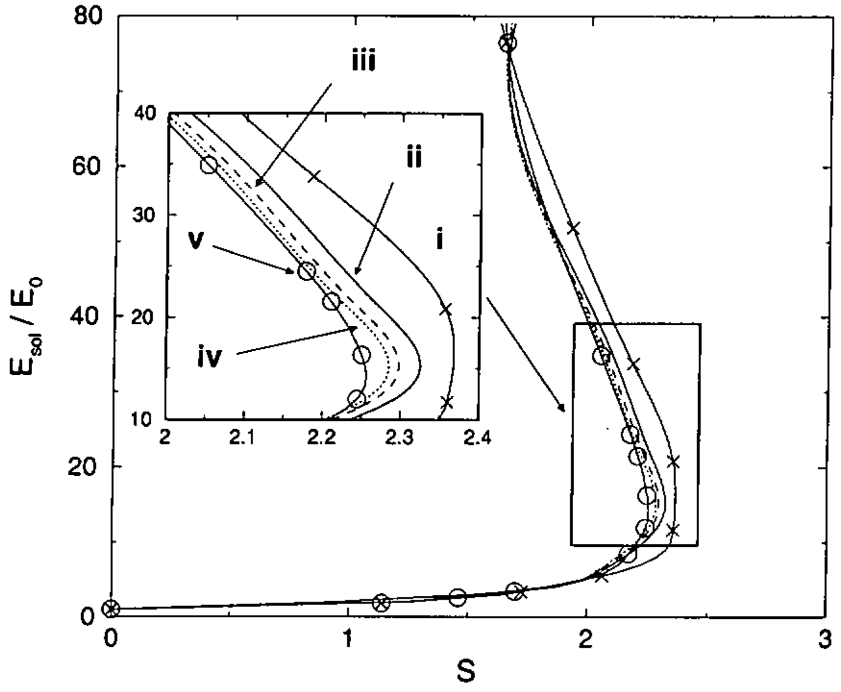

Figure 4.3: Energy enhancement versus map strength S. The pulse width is measured at the mid-point of the normal dispersion fiber segment. Curve i (crosses), ii (solid line), iii (dashed line), iv (dotted line), and v (circles) correspond to R = 0.5, 0.8, 0.9, 0.95, and 1 respectively. The map parameters are the same as that in Figure 4.1.

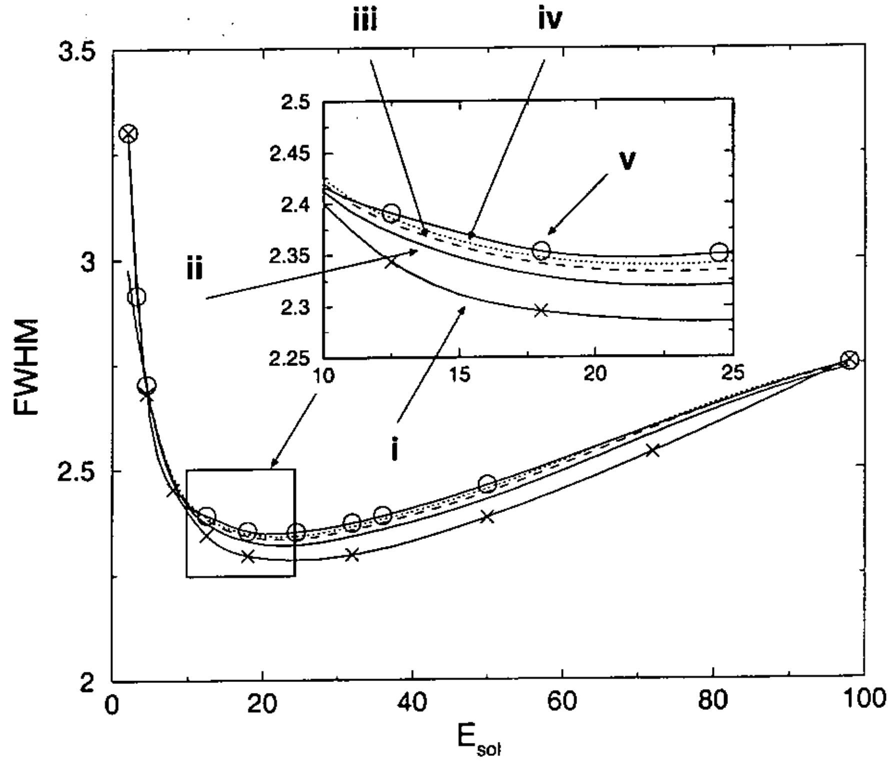

Figure 4.4: Normalized FWHM at the mid-point of the normal dispersion fiber segment versus normalized pulse energy E_{sol}. The parameters and notation are the same as that in Figure 4.3.

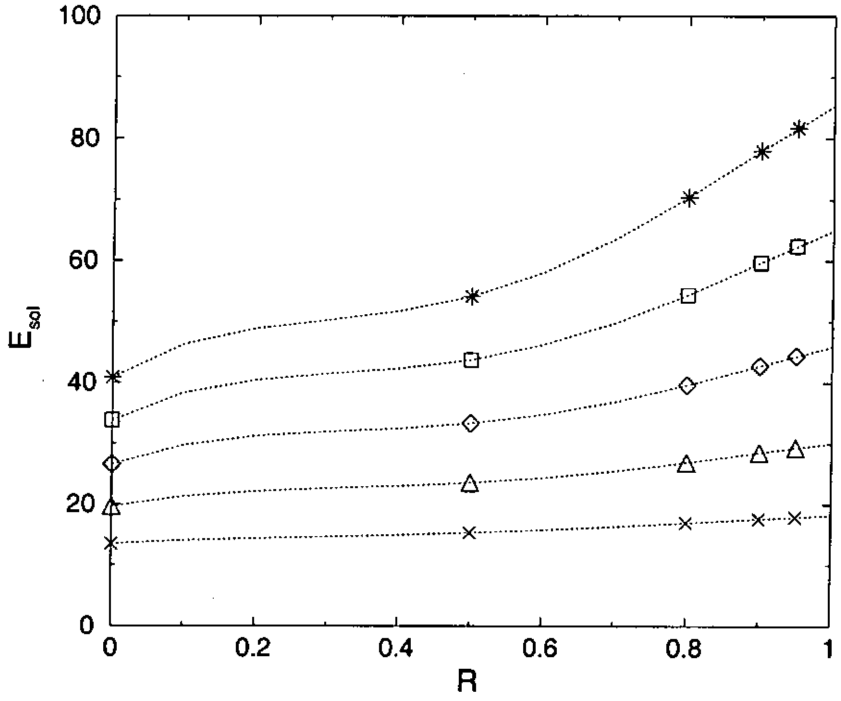

Figure 4.5: Normalized pulse energy E_{sol} versus length ratio R at map strength $S = 3$ (crosses), 3.5 (triangles), 4 (diamonds), 4.5 (squares), and 5 (asterisks). The parameters of the dispersion map are the same as that in Figure 4.1.

of all normal dispersion fibers is about 2 times larger than that of a DM map made up of all anomalous dispersion fibers.

Figure 4.6 plots the variation of the pulse width with R for a normalized energy of 50. The pulse widths at the mid-point of the anomalous dispersion fiber (solid line), the mid-point of the normal dispersion fiber (dashed line), and the junction of the two fibers (dotted line) are shown. The crosses represent actual simulation results. The pulse width at the mid-points of the fiber segments remain nearly constant when R increase from 0 to 1 but the maximum pulse width increases by almost 50%. Figure 4.7 plots the pulse width stretching factor, *i.e.,* the difference between the maximum pulse width and the minimum pulse width, of the DM solitons as a function of R. We observed that the DM solitons stretch more as R increases. As a result, the nonlinear effect is weakened

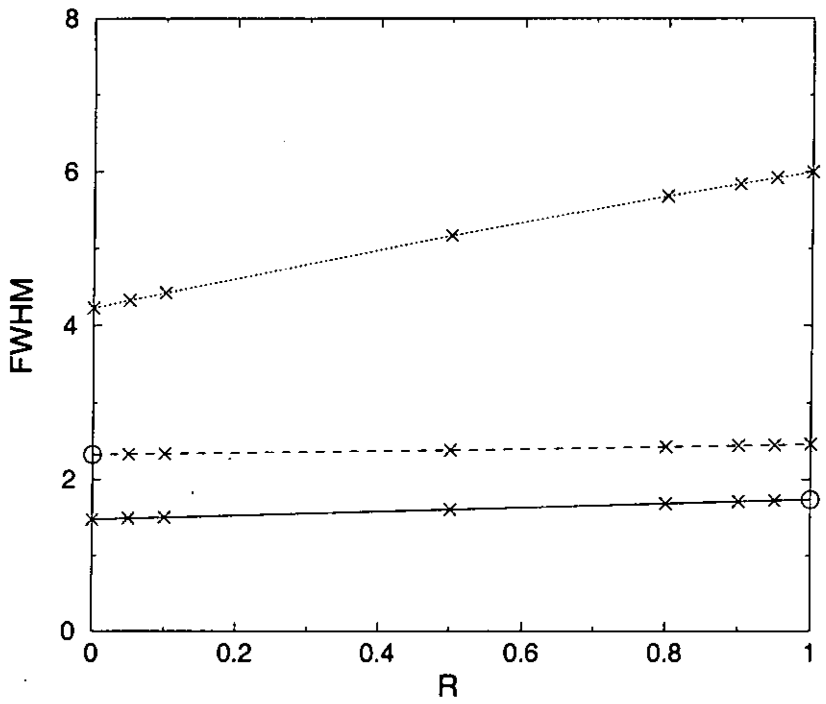

Figure 4.6: Normalized pulse width as a function of the length ratio R at the mid-point of the anomalous dispersion fiber (solid line), the mid-point of the normal dispersion fiber (dashed line), and the junction of the two fibers (dotted line). The normalized pulse energy is 50. The map parameters are the same as that in Figure 4.1.

when the length of the normal dispersion fiber increases. For the same pulse width, more energy is therefore needed to launch a DM soliton. This explains why energy enhancement increases when R increases. Figure 4.8 plots the maximum chirp coefficient (solid line) and the chirp coefficient at the junction of the two fibers (dashed line) as a function of R. In both cases, the chirp coefficients increase slightly when R increases.

4.3 Zero and Normal Average Dispersion

In this Section, we study the effect of the relative proportion of the normal dispersion fiber segment in a two-step dispersion map on the soliton energy for zero average and

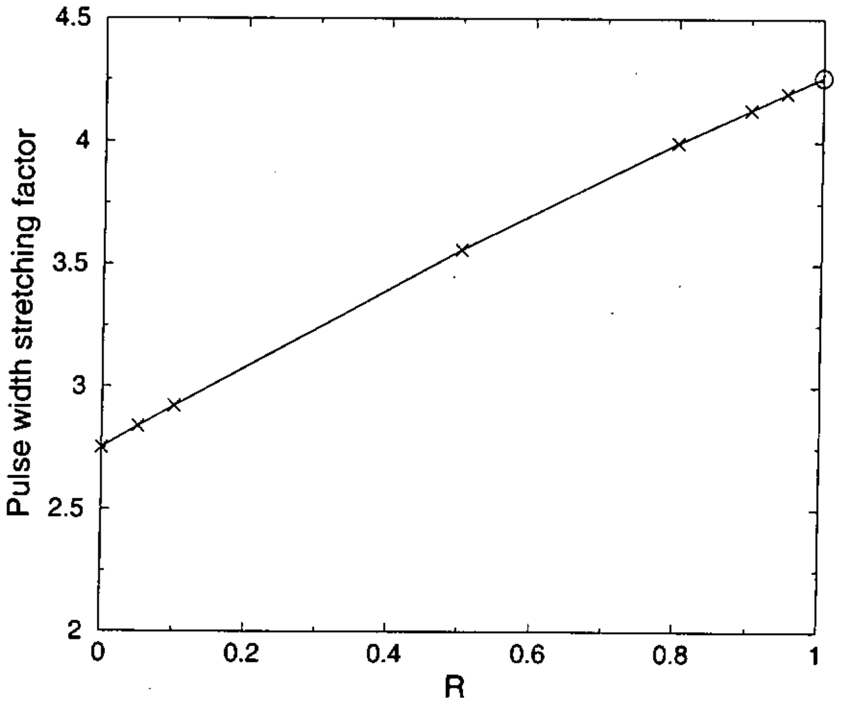

Figure 4.7: The pulse width stretching factor as a function of the length ratio R. The parameters of the dispersion map are the same as that in Figure 4.1.

normal average dispersion systems, *i.e.*, $\ddot{\beta}_{\text{av}} \geq 0$. As conventional solitons do not exist for these dispersion values, energy enhancement are not applicable here. For comparison with the results in the previous Section, the map length L is set to 200 km and the cumulated absolute dispersion is 1,600 ps^2. Similar to DM systems using DCFs, we found that soliton solutions exist for DM systems using FBG for both zero and normal average dispersion.

The results from zero average dispersion is qualitatively the same as that of anomalous average dispersion. Figure 4.9 plots the DM soliton energy versus map strength. The curves labeled a (diamonds), b (crosses), c (solid line), d (dashed line), e (dotted line), and f (circles) correspond to length ratio R = 0, 0.5, 0.8, 0.9, 0.95, and 1. The numerical parameters used in obtaining the results are $\Delta z = 7.8 \times 10^{-4}$, number of points in the time domain = 4,096, and computation window size = 2,000 ps. The propagation distance is

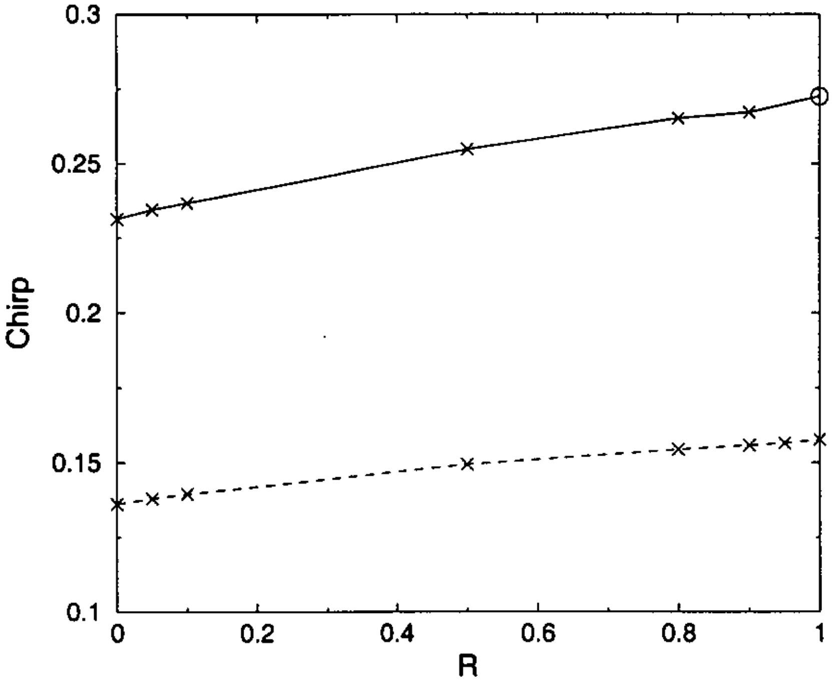

Figure 4.8: The maximum chirp coefficient (solid line) and the chirp coefficient at the segment boundary (dashed line) as a function of the length ratio R. The circle is the maximum chirp coefficient at $R = 1$. The dispersion map parameters are the same as that in Figure 4.1.

100,000 km (500 dispersion maps) or 200,000 km (1,000 dispersion maps). The maximum numerical error in the temporal pulse amplitude is 10^{-8}. The initial pulse width is 20 ps. The curves are plotted using the minimum pulse widths in the dispersion maps, *i.e.*, from the mid-point of the anomalous dispersion fiber in curves a to e, but from the mid-point of the normal dispersion fiber for curve f, the all normal dispersion fiber case. In Figure 4.10, the pulse widths at the mid-point of the normal dispersion fiber is used in all cases. Similar to anomalous average dispersion systems, the shift in curve f of Figure 4.9 is due to the change in the location at which the minimum pulse width is measured. From Figure 4.9, the threshold map strength for soliton solutions are about 3.8 for all values of R. Figure 4.11 shows the normalized DM soliton energy versus the length ratio for $S = 4$ (diamonds), 4.5 (squares), 5 (asterisks), 5.5 (pluses), and 6 (inverted triangles). While the soliton energy is about the same for all values of R when $S = 4$, there is a factor of 2 difference between the soliton energy at $R = 0$ and that at $R = 1$ for $S = 6$. The effect of the length ratio is larger for stronger map strength. We note that for the same map strength, it takes less energy to launch a DM soliton in DM systems with zero average dispersion than that with anomalous average dispersion. Figures 4.12 and 4.13 show the pulse width and the pulse width stretching factor at the normalized energy of 50 respectively. For the same energy, DM solitons with zero average dispersion are stretched more as R increases from 0 to 1 when compared to that with anomalous average dispersion. As a result, the relative increase in DM soliton energy is also larger. The maximum chirp coefficient (solid line) and the chirp coefficient at the boundary of the two fiber segments (dashed line) are plotted in Figure 4.14. In both cases, the chirp coefficients increase slightly when R increases.

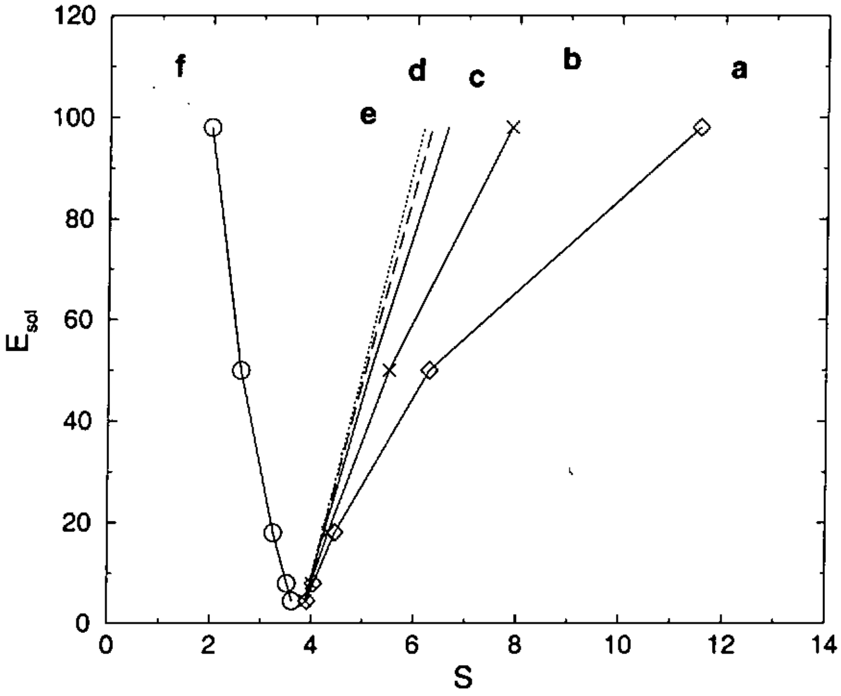

Figure 4.9: Normalized pulse energy $E_{\rm sol}$ as a function of map strength S in zero average dispersion DM systems. The minimum pulse width in the dispersion map is used in S. The curve a (diamonds), b (crosses), c (solid line), d (dashed line), e (dotted line), and f (circles) correspond to length ratio $R = 0$, 0.5, 0.8, 0.9, 0.95, and 1 respectively. The map length is 200 km and the cumulated absolute dispersion over a map is 1,600 ps^2.

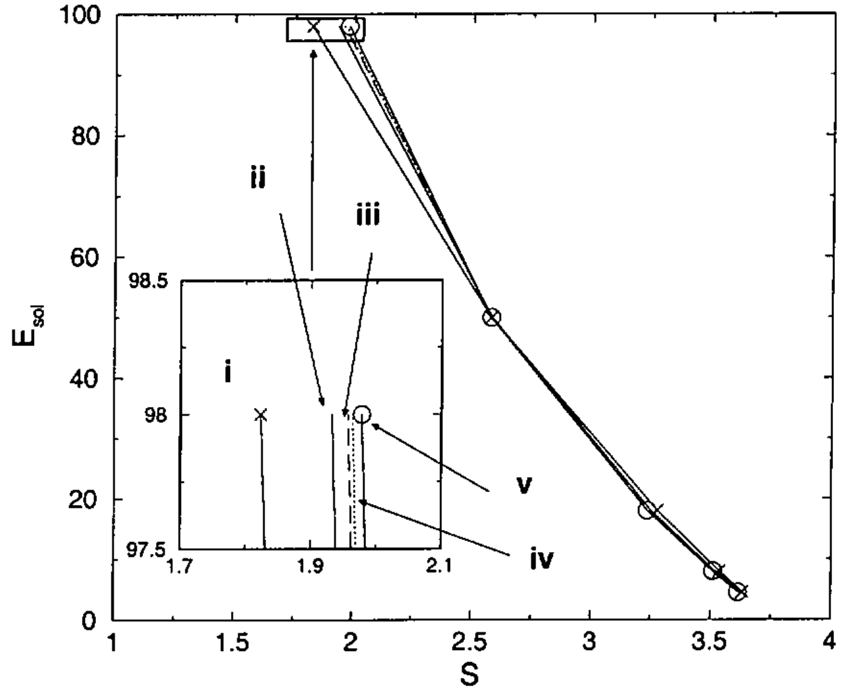

Figure 4.10: Normalized pulse energy $E_{\rm sol}$ as a function of map strength S. The pulse width is measured at the mid-point of the normal dispersion fibers. Curve i (crosses), ii (solid line), iii (dashed line), iv (dotted line), and v (circles) correspond to $R = 0.5$, 0.8, 0.9, 0.95, and 1 respectively.

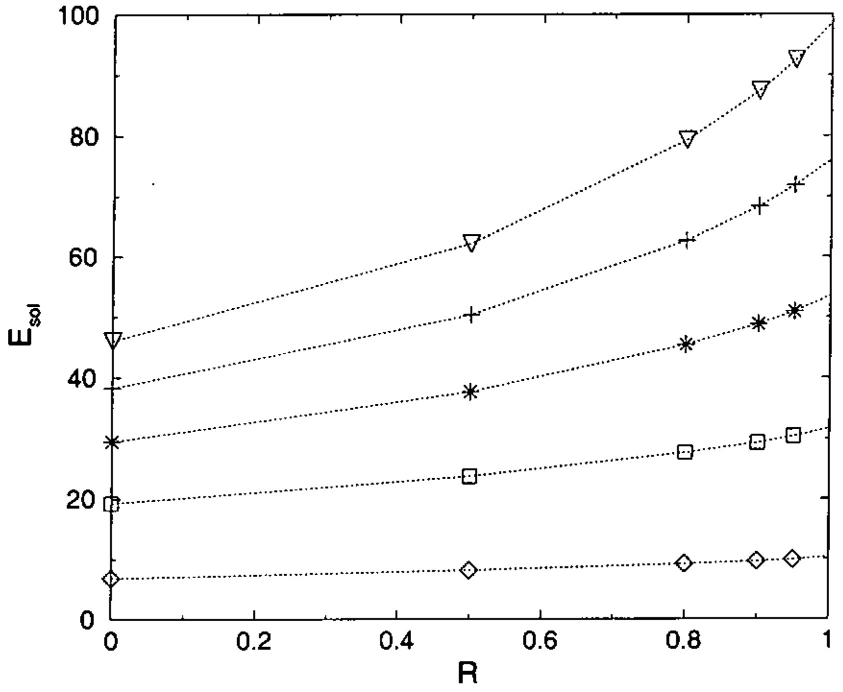

Figure 4.11: Normalized pulse energy E_{sol} as a function of the length ratio R at map strength $S = 4$ (diamonds), 4.5 (squares), 5 (asterisks), 5.5 (pluses), and 6 (inverted triangles). The parameters are the same as that in Figure 4.9.

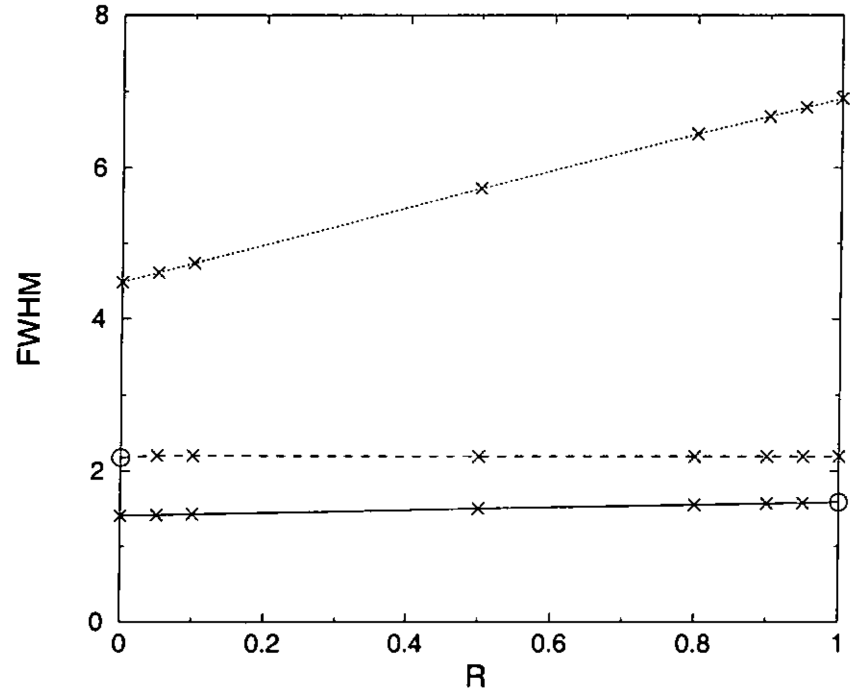

Figure 4.12: Normalized pulse width (FWHM) as a function of the length ratio R for zero average dispersion systems. Solid line represents the pulse widths measured at the mid-point of the anomalous dispersion fiber, dashed line at the mid-point of the normal dispersion fiber, and dotted line at the segment boundary. The normalized pulse energy is 50. The map length L is 200 km, and the cumulated absolute dispersion in a dispersion map is 1,600 ps^2.

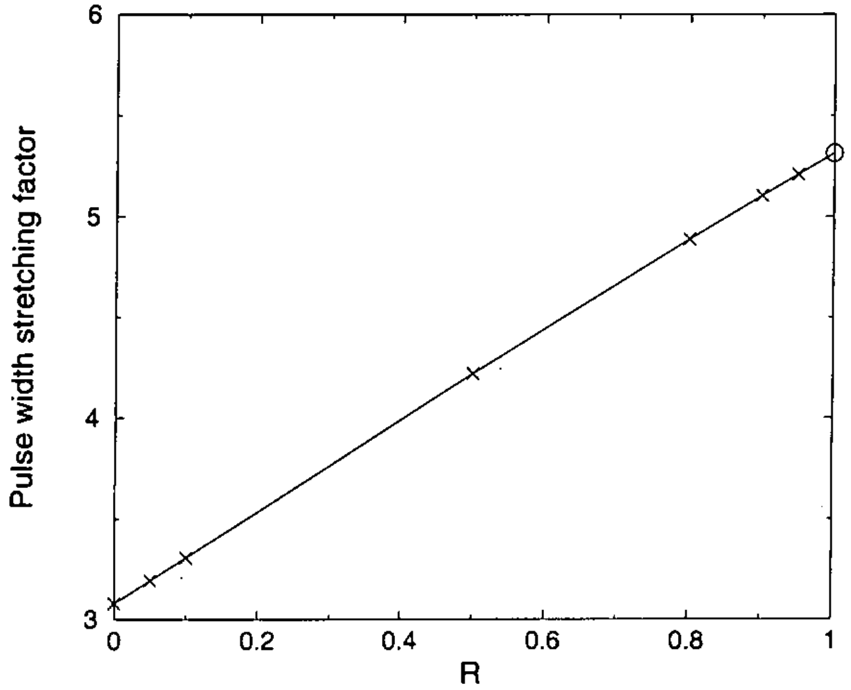

Figure 4.13: Pulse width stretching factor as a function of the length ratio R. The circle represents the result at $R = 1$. The parameters of the DM systems are the same as that in Figure 4.12.

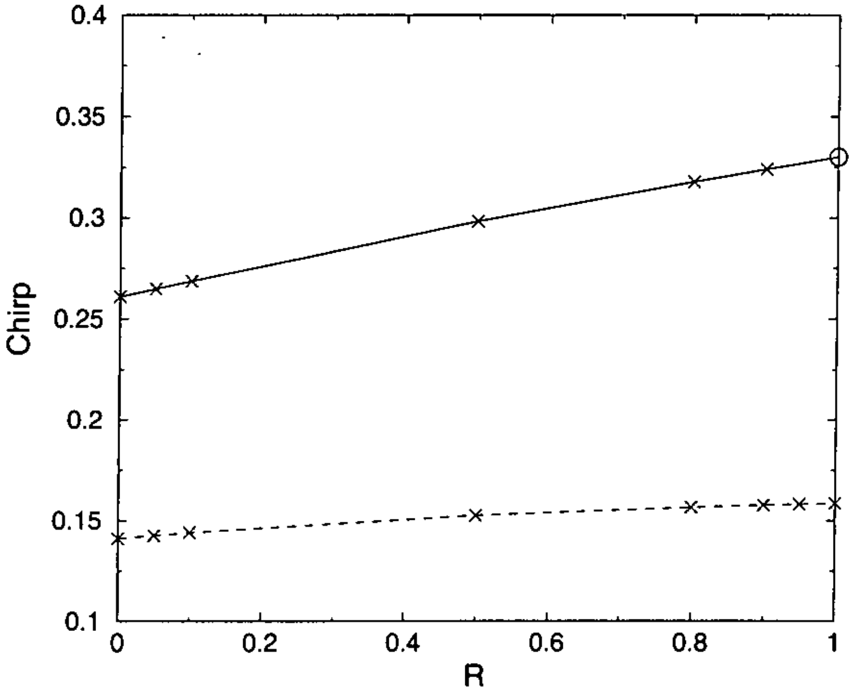

Figure 4.14: Chirp coefficient as a function of the length ratio R. Solid line represents the maximum chirp coefficient and dashed line represents the chirp coefficient at the boundary of the fiber segment. The parameters of the DM systems are the same as that in Figure 4.12.

For DM systems with normal average dispersion, solitons exist but only for a narrow range of dispersion values. We have tried $\ddot{\beta}_{\mathrm{av}} = 0.1$ ps^2/km. We found that very high energies are needed to form the solitons; the normalized energy must be larger than 170. At this or higher energy, numerical errors are significant and appear as large spikes in the frequency spectrum. The numerical errors of the pulse amplitudes in the time domain is 10^{-4} to 10^{-3} after 200,000 km of propagation using the numerical averaging technique. Further propagation does not improve the accuracy of the solutions. Recall that the numerical error of typical soliton solutions for anomalous average and zero average DM systems are 10^{-8} to 10^{-6}. The numerical step size Δz is 7.8×10^{-5}, the length of the computation window is 2,000 ps, and 4,096 points are used for the FFT algorithm. The numerical error can be reduced by reducing the numerical step size at the expense of computation time. The computational time required in the above example is already 6 CPU hours in a PIII 500 MHz personal computer. Also as the map strength increases, the DM soliton energies increase further, thus the numerical errors increase. We therefore choose a smaller average dispersion value $\ddot{\beta}_{\mathrm{av}} = 0.01$ ps^2/km in Figure 4.15. The error for the pulse amplitudes in the time domain is 10^{-4}, 10^{-5}, 10^{-6}, and 10^{-7} for the four data points at all values of R in order of increasing pulse energy. The solutions at lower energy are therefore not very reliable.

Figure 4.15 plots the DM soliton energies versus the map strength for different length ratio R. The map length is 200 km, and the cumulated dispersion is 1,600 ps^2/km. The curves a (diamonds), b (crosses), c (solid line), d (dashed line), and e (dotted line) correspond to $R = 0$, 0.5, 0.8, 0.9, and 0.95 respectively. The pulse width is measured at the mid-point of the anomalous dispersion fiber. We observed that DM solitons exist for

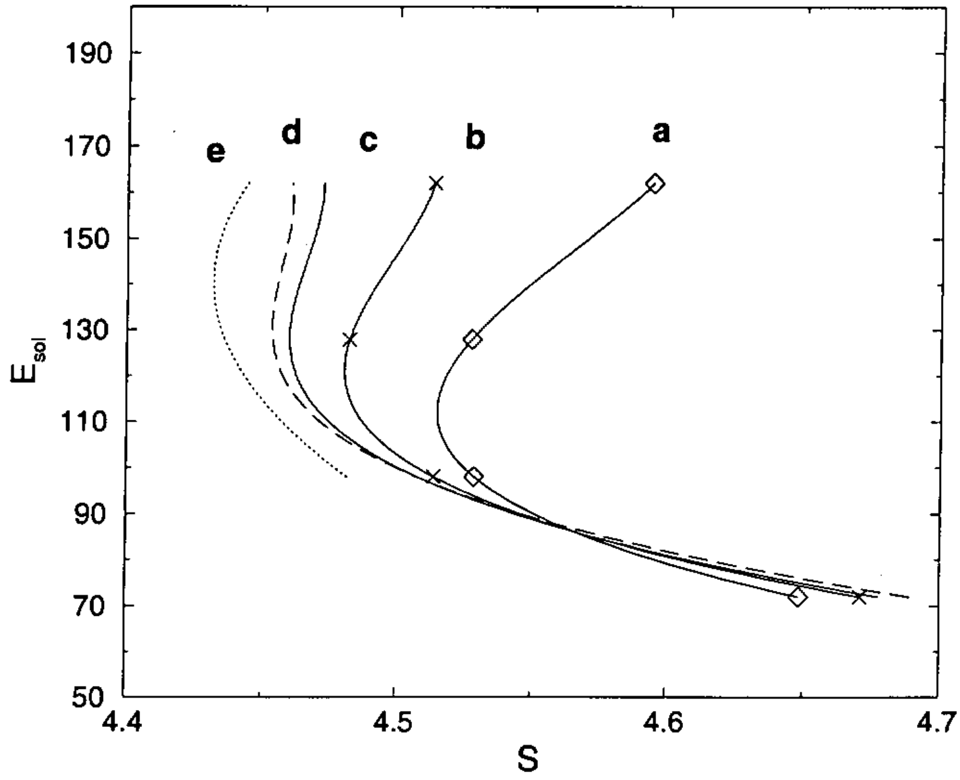

Figure 4.15: Normalized pulse energy E_{sol} as a function of map strength in normal average dispersion systems. Curve a (diamonds), b (crosses), c (solid line), d (dashed line), and e (dotted line) correspond to $R = 0$, 0.5, 0.8, 0.9, and 0.95 respectively. The average dispersion is 0.01 $\mathrm{ps}^2/\mathrm{km}$, the map length is 200 km, and the cumulated absolute dispersion is $1,600$ ps^2.

a narrow range of map strength only; from about 4.4 to 4.7. The soliton energies vary rapidly in this range, changing from a normalized value of 70 to 170. The threshold map strength for DM solitons varies with R. For example, at a map strength equals to 4.5, the all anomalous dispersion fiber case ($R = 0$) does not have DM solitons but the equal map length systems $R = 0.5$ do. But at map strength about 4.48, the equal map length systems also do not have solition solutions. Also contrary to DM systems with anomalous average or zero average dispersion, there can be two DM solitons with different energies at a given map strength.

It is difficult to draw quantitative conclusion because the solutions at low energies are not reliable. But we observed that DM systems using FBGs still have the maximum ($R = 1$) and the minimum ($R = 0$) energy when R varies. The increase in energy between $R = 0$ and $R = 1$ can be larger than a factor of 2. Figures 4.16 and 4.17 plot the pulse width and the pulse width stretching ratio as a function of R for a pulse energy of 128. We found that the change in both the pulse width and the stretch ratio is very small. The variations in the chirp coefficients are also small as seen in Figure 4.18.

4.4 Discussions

From previous sections, we find that the relative proportion of normal dispersion fiber to anomalous dispersion fiber in a two-step dispersion map affects the DM soliton properties in anomalous average, zero average, and normal average dispersion systems. The total map length, average dispersion, and cumulated absolute dispersion are kept constant. We found that the DM solitons have the highest energy when the map is made up of all normal dispersion fibers and a fiber Bragg grating. The solitons have the lowest energy

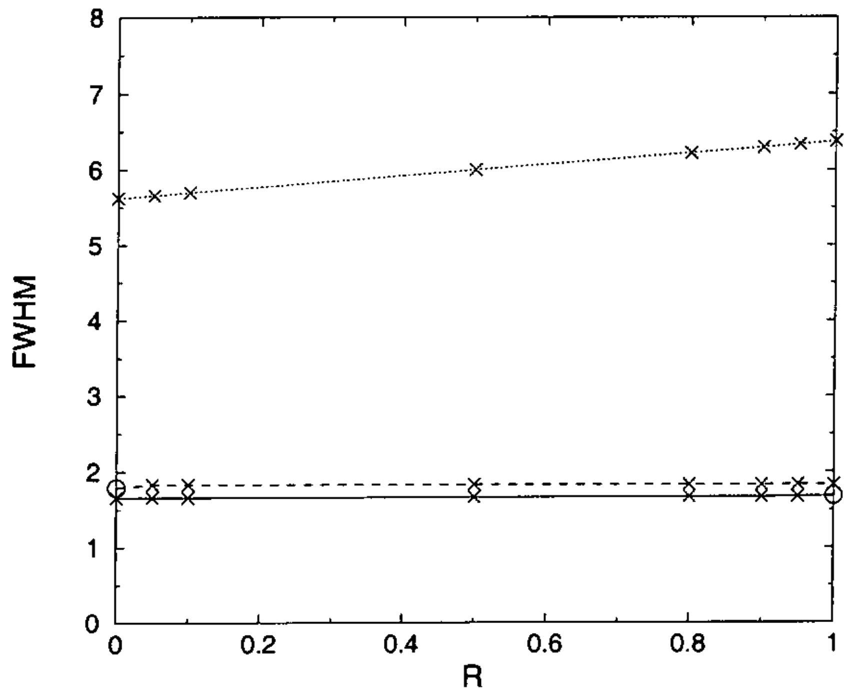

Figure 4.16: Normalized pulse width at the mid-point of the anomalous dispersion fiber segment (solid line), the mid-point of the normal dispersion fiber segment (dashed line), and the boundary between the fiber segments (dotted line), as a function of the length ratio R. The normalized pulse energy is 128. The map parameters are the same as that in Figure 4.15.

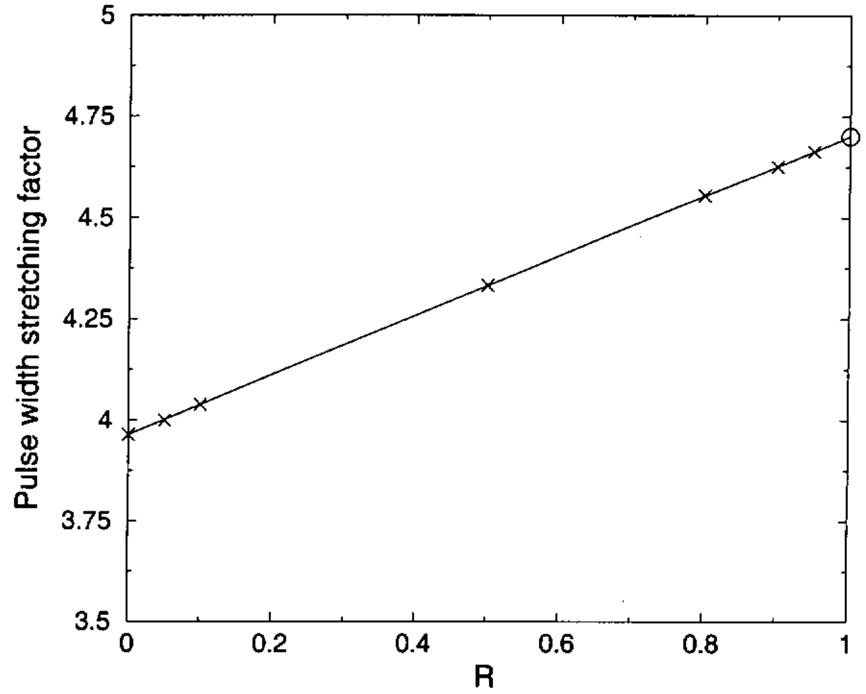

Figure 4.17: Pulse width stretching factor as a function of length ratio R. The map parameters are the same as that in Figure 4.15.

when the map is made up of all anomalous dispersion fibers and a fiber Bragg grating. The ratio of the highest to the lowest energy can be 2 or higher. The minimum pulse width increases only slightly when the normal dispersion fiber length to map length R varies from 0 to 1. However, the maximum pulse width can increase by more than 50%. In other words, the DM solitons spread out more as the proportion of normal dispersion fiber increases, which explains why more energy is needed to form a soliton.

If the objective is to have the highest soliton energy in each wavelength in order to maximum the signal-to-noise ratio (SNR), DM systems consist of all normal dispersion fibers and FBGs are clearly the solution. However, since the pulse spread more, the bit window in such systems may have to be increased in order to avoid interactions between solitons in adjacent bit windows. How the DM soliton interaction depends on the length ratio has yet to be determined. In any case, it may not be advantageous to use pulses

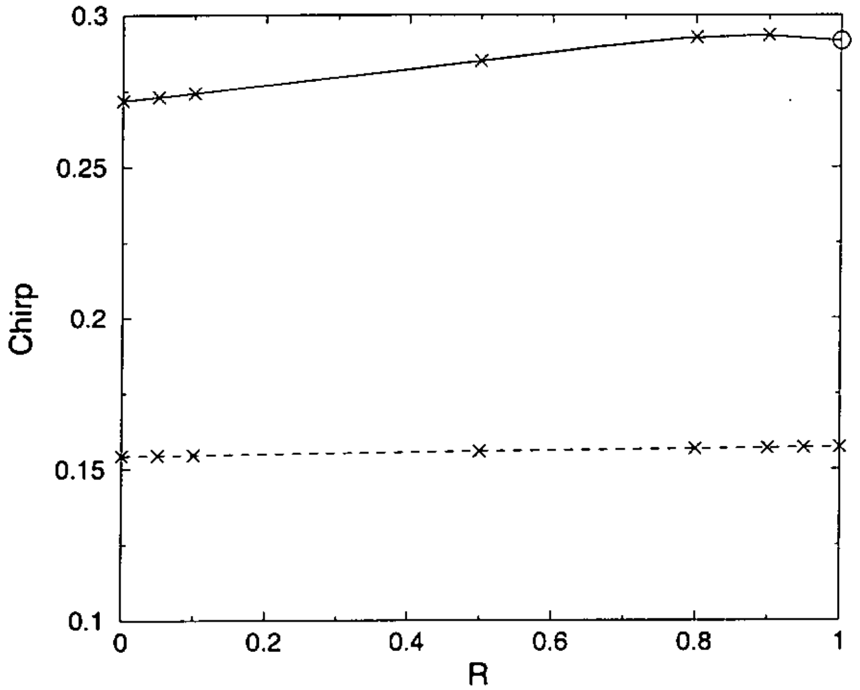

Figure 4.18: Chirp coefficient as a function of the length ratio R. The solid line represents the maximum chirp coefficient and the dashed line represents the chirp coefficient at the boundary between the two fiber segments. The map parameters are the same as that in Figure 4.15.

that are too strong in the wavelength channels because the nonlinear effects in a fiber also depend on the total energy in fiber. Indeed, recent 1 tera bits per second transmission experiments were achieved by using specially made fibers with large effective core area to reduce the overall energy density in the fiber [1].

From our simulations, DM systems with average normal dispersion are not very attractive for communication systems. First the energy required to launch these solitons may be too high. Second, these solitons are very sensitivity to map parameters and the pulse width. Slight deviation of the pulse width from the required value, due to source fluctuations, may cause significant pulse distortion during transmission. Therefore, we expect that DM soliton systems will use dispersion maps with average anomalous dispersion.

Chapter 5

Conclusion

The performance of an optical communication system is measured by the bandwidth distance product for error free transmission, *i.e.*, a BER of 10^{-9} or less. The BER depends on a large number of factors including chromatic dispersion, polarization mode dispersion, gain flatness, amplifier noises, nonlinear effects, *etc.* In this thesis, we review a number of methods that alleviate the effect of chromatic dispersion. We focus on the combination of dispersion management technique and soliton propagation format. Two-step dispersion maps made up of equal length fiber segments are well studied in the literature. An empirical formula for energy enhancement was derived which depends on only two parameters; the map strength and the map depth. Although there are indications that two-step dispersion maps made up of mostly normal dispersion fibers have higher energy enhancement, there is no comprehensive study on the subject.

We investigate the properties of DM solitons in a two-step dispersion map made up of unequal length fiber segments for average anomalous, average zero, and average normal dispersion systems. In particular, we study how the soliton energy depends on the proportion of the normal dispersion fiber in a dispersion map when the total map length, average dispersion, and cumulated absolute dispersion are fixed. In all cases studied, dispersion maps made up of normal dispersion fibers and fiber Bragg gratings have the maximum soliton energy. Dispersion maps made up of anomalous dispersion fibers and fiber Bragg gratings have the minimum soliton energy. The ratio of the maximum to the minimum soliton energy can be more than a factor of two when the map strength is large. We also observed that while the minimum pulse width of the DM solitons do not change significantly when the proportion of the normal dispersion fiber changes, the maximum pulse width can increase by more than 50%. Whether this increase in the maximum pulse width results in larger soliton-soliton interaction has yet to be investigated, but this observation does raise the possibility that the increase in soliton energy may come at the expense of a larger bit window thus a decrease in the maximum transmission rate. Also in a wavelength division multiplexing system, one do not want to single-mindedly increase the energy of the signals in each wavelength channel in order to reduce the SNR. Increase in the average energy of the fiber will give rise to scores of nonlinear effects that will eventually degrade the BER.

The complex relationship between the soliton properties and dispersion map parameters highlights the difficulties in finding the optimal dispersion map. Even in a two-step dispersion map, the energy and pulse width of a DM soliton in general depends on four parameters. In this investigation, we fix three of them to study the effect of the fourth. A comprehensive study requires one to vary the other three parameters as well which is a computationally intensive task. Analytical techniques such as Lagrangian method give a qualitative understanding of the system at best but they are not useful for choosing the parameters for real systems. Even when the above simulations are carried out, the results may be of limited use because other factors such as amplifier spacing, amplifier noises, and the presence of other channels may have significant impacts on the system design parameters. This is not to say that studies like the current one is not useful. They allow one to build an understanding of the systems by studying the effects of the many parameters at a time. The process is painfully slow but it complements the massive system simulations that are favored by some researchers. System simulations are in effect numerical experiments. They are certainly much cheaper to carry out than real experiments but a system contains so many variables that it is difficult to understand the relationship among them. An optical communication system is so complex that no single method is sufficient to determine the optimum design parameters. One will have to use every means available including analytical analysis, numerical simulations of idealized systems, and full system simulations to tackle the problem.

Appendix A

A.1 Solution of dispersion equation

We apply Fourier transform to Eq. (1.1),

$$\begin{aligned} i\frac{\partial q}{\partial z} - \left[\frac{\ddot{\beta}(z)}{2}\right]\frac{\partial^2 q}{\partial t^2} &= 0,\text{(A.1)} \\ \frac{i}{2\pi}\int_{-\infty}^{\infty}\frac{\partial \tilde{q}(z,\omega)}{\partial z}\exp(-i\omega t)\,d\omega - \left[\frac{\ddot{\beta}(z)}{4\pi}\right]\int_{-\infty}^{\infty}(-i\omega)^2\tilde{q}(z,\omega)\exp(-i\omega t)\,d\omega &= 0,\text{(A.2)} \end{aligned}$$

where $\tilde{q}(z,\omega)$ is the spectrum of the pulse $q(z,t)$. Eq. (A.2) can be rewritten as,

$$\int_{-\infty}^{\infty}\left\{i\frac{\partial \tilde{q}(z,\omega)}{\partial z} + \left[\frac{\ddot{\beta}(z)\omega^2}{2}\right]\tilde{q}(z,\omega)\right\}\exp(-i\omega t)\,d\omega = 0.$$

Hence

$$\begin{aligned} i\frac{\partial \tilde{q}(z,\omega)}{\partial z} + \left[\frac{\ddot{\beta}(z)\omega^2}{2}\right]\tilde{q}(z,\omega) &= 0, \\ \tilde{q}(L,\omega) &= \tilde{q}(0,\omega)\exp\left[\frac{i\omega^2}{2}\int_0^L \ddot{\beta}(z)\,dz\right]. \end{aligned}$$

A.2 Evolution of a Gaussian pulse

For an initial Gaussian pulse,

$$q(0,t) = \exp\left(\frac{-t^2}{2T_0^2}\right),$$

$$\tilde{q}(0,\omega) = \int_{-\infty}^{\infty} \exp\left(\frac{-t^2}{2T_0^2} + i\omega t\right) dt.$$

By completing square and using $\int_{-\infty}^{\infty} \exp\left(-ax^2\right) dx = \sqrt{\pi/a}$, we have

$$\begin{aligned}\tilde{q}(0,\omega) &= \int_{-\infty}^{\infty} \exp\left[\frac{-1}{2T_0^2}\left(t - i\omega T_0^2\right)^2 - \frac{\omega^2 T_0^2}{2}\right] dt, \\ &= \sqrt{2\pi} T_0 \exp\left(\frac{-\omega^2 T_0^2}{2}\right).\end{aligned}$$

From Appendix A.1, the solution of Eq. (1.1) at distance L is,

$$\begin{aligned}\tilde{q}(L,\omega) &= \sqrt{2\pi} T_0 \exp\left[\frac{-T_0^2\omega^2}{2} + \frac{i\omega^2}{2}\int_0^L \ddot{\beta}(z)\, dz\right], \\ q(L,t) &= \frac{T_0}{\sqrt{2\pi}} \int_{-\infty}^{\infty} \exp\left\{\left[\frac{-T_0^2}{2} + \frac{i}{2}\int_0^L \ddot{\beta}(z)\, dz\right]\omega^2 - i\omega t\right\} d\omega.\end{aligned}$$

Let $a = -[T_0^2 - i\int_0^L \ddot{\beta}(z)\, dz]/2$, we have

$$\begin{aligned}q(L,t) &= \frac{T_0}{\sqrt{2\pi}} \int_{-\infty}^{\infty} \exp\left[a\omega^2 - i\omega t\right] d\omega, \\ &= \frac{T_0}{\sqrt{2\pi}} \int_{-\infty}^{\infty} \exp\left[a\left(\omega - \frac{it}{2a}\right)^2 + \frac{t^2}{4a}\right] d\omega, \\ &= \frac{T_0}{\sqrt{2\pi}} \exp\left(\frac{t^2}{4a}\right)\sqrt{\frac{\pi}{-a}}, \\ &= \frac{T_0}{\sqrt{2\pi}} \exp\left\{\frac{-t^2}{2[T_0^2 - i\int_0^L \ddot{\beta}(z)\, dz]}\right\}\sqrt{\frac{2\pi}{T_0^2 - i\int_0^L \ddot{\beta}(z)\, dz}}, \\ &= \frac{T_0}{\sqrt{T_0^2 - i\int_0^L \ddot{\beta}(z)\, dz}} \exp\left\{\frac{-t^2}{2[T_0^2 - i\int_0^L \ddot{\beta}(z)\, dz]}\right\}.\end{aligned}$$

The intensity of the pulse $q(L,t)$ is,

$$\begin{aligned}|q(L,t)|^2 &= q(L,t) \times q^*(L,t), \\ &= \left\{\frac{T_0^2}{\sqrt{T_0^4 + [\int_0^L \ddot{\beta}(z)\, dz]^2}}\right\} \exp\left\{\frac{-t^2}{2[T_0^2 - i\int_0^L \ddot{\beta}(z)\, dz]} - \frac{t^2}{2[T_0^2 + i\int_0^L \ddot{\beta}(z)\, dz]}\right\}.\end{aligned}$$

When $\ddot{\beta}(z)$ is a constant value,

$$|q(L,t)|^2 = \left\{\frac{T_0^2}{\sqrt{T_0^4 + (\ddot{\beta}L)^2}}\right\} \exp\left[\frac{-t^2 T_0^2}{T_0^4 + (\ddot{\beta}L)^2}\right].$$

Full width at exp(−1) normalized intensity $= 2T_0\sqrt{1 + (\ddot{\beta}L/T_0^2)^2}$.

A.3 Relationship between GVD and group velocity

The group velocity delay $\dot{\beta}$ is defined as

$$\dot{\beta} = \frac{d\beta}{d\omega} = \frac{1}{v_{\mathrm{g}}},$$

where β is the propagation constant, ω is the angular frequency, and v_{g} is the group velocity. Therefore, the group velocity dispersion $\ddot{\beta}$ is

$$\begin{aligned} \ddot{\beta} &= \frac{d\dot{\beta}}{d\omega}, \\ &= \frac{d}{d\omega}\left(\frac{1}{v_{\mathrm{g}}}\right), \\ &= -\frac{1}{v_{\mathrm{g}}^2}\left(\frac{dv_{\mathrm{g}}}{d\omega}\right). \end{aligned}$$

For negative dispersion, *i.e.*, $\ddot{\beta} < 0$, so $dv_{\mathrm{g}}/d\omega > 0$, the velocity increases as the frequency increases.

A.4 The solution of SPM equation

Before solving Eq. (1.6), we show that $|q|^2$ is independent of z.

$$q^*\left(i\frac{\partial q}{\partial z} + |q|^2 q\right) = 0, \tag{A.3}$$

$$\left[q^*\left(i\frac{\partial q}{\partial z} + |q|^2 q\right)\right]^* = 0. \tag{A.4}$$

Subtracting Eqs. (A.3) from (A.4), we have

$$\begin{aligned} \left(iq^*\frac{\partial q}{\partial z} + |q|^4\right) - \left[-iq\left(\frac{\partial q}{\partial z}\right)^* + |q|^4\right] &= 0, \\ q^*\frac{\partial q}{\partial z} + q\frac{\partial q^*}{\partial z} &= 0, \\ \frac{\partial}{\partial z}\left(q^* q\right) &= 0, \\ \frac{\partial(|q|^2)}{\partial z} &= 0. \end{aligned}$$

Hence, $|q|^2$ is constant. Eq. (1.6) can then be solved directly, we have

$$\begin{aligned}
i\frac{\partial q}{\partial z} + |q|^2 q &= 0, \\
i\int_0^L \frac{1}{q}\left(\frac{\partial q}{\partial z}\,dz\right) &= -\int_0^L |q|^2\,dz, \\
q(L,t) &= q(0,t)\exp(i|q(0,t)|^2 L).
\end{aligned}$$

We use $|q(0,t)|$ in the exponent because $|q|^2$ is unchanged as distance increases.

A.5 Higher order z-derivatives of the solutions of the NLS equation

Assume $q(z,t)$ is continuous and differentiable at z and t.

$$\begin{aligned}
q_z &= i\left(\frac{1}{2}q_{tt} + |q|^2 q\right). \\
q_{zz} &= i\left(\frac{1}{2}q_{ttz} + 2|q|^2 q_z + q^2 q_z^*\right), \\
&= i\frac{1}{2}\frac{\partial}{\partial t}\left(i\frac{1}{2}q_{ttt} + i2|q|^2 q_t + iq^2 q_t^*\right) - |q|^2 q_{tt} - |q|^4 q + \frac{1}{2}q^2 q_{tt}^*, \\
&= -\frac{1}{4}q_{tttt} - 2|q|^2 q_{tt} - 2|q_t|^2 q - q_t^2 q^* - |q|^4 q. \\
q_{zzz} &= i\left(\frac{1}{2}q_{ttz} + 2|q|^2 q_z + q^2 q_z^*\right)_z, \\
&= i\frac{1}{2}q_{zztt} + 2iq_z^2 q^* + 2i|q_z|^2 q + 2i|q|^2 q_{zz} + 2iq|q_z|^2 + iq^2 q_{zz}^*, \\
&= i\frac{1}{2}\left(-\frac{1}{4}q_{tttt} - 2|q|^2 q_{tt} - 2|q_t|^2 q - q_t^2 q^* - |q|^4 q\right)_{tt} + 2i\left[i\left(\frac{1}{2}q_{tt} + |q|^2 q\right)\right]^2 q^* \\
&\quad +2i\left[i\left(\frac{1}{2}q_{tt} + |q|^2 q\right)\right]\left[-i\left(\frac{1}{2}q_{tt}^* + |q|^2 q^*\right)\right] q + 2i|q|^2 \Big(-\frac{1}{4}q_{tttt} - 2|q|^2 q_{tt} - 2|q_t|^2 q \\
&\quad -q_t^2 q^* - |q|^4 q\Big) + 2iq\left[i\left(\frac{1}{2}q_{tt} + |q|^2 q\right)\right]\left[-i\left(\frac{1}{2}q_{tt}^* + |q|^2 q^*\right)\right] + iq^2 \Big[-\frac{1}{4}q_{tttt}^* - 2|q|^2 q_{tt}^* \\
&\quad -2|q_t|^2 q^* - (q_t^*)^2 q - |q|^4 q^*\Big], \\
&= i\frac{1}{2}\Big\{-\frac{1}{4}q_{tttttt} - \left(2q_t q_{tt} q^* + q_t^2 q_t^*\right)_t - (2q_t q^* q_{tt} + 2qq_t^* q_{tt} + 2|q|^* q_{ttt})_t - \Big(2q_t|q_t|^2
\end{aligned}$$

$$
\begin{aligned}
&+2qq_{tt}q_t^* + 2qq_tq_{tt}^*)_t - \left[3q^2q_t\left(q^*\right)^2 + 2q^3q^*q_t^*\right]_t\Big\} - i\frac{1}{2}q_{tt}^2q^* - 2iq_{tt}|q|^4 - 2i|q|^6q \\
&+i\frac{1}{2}|q_{tt}|^2q + i|q|^2q^2q_{tt}^* + i|q|^4q_{tt} + 2i|q|^6q - i\frac{1}{2}|q|^2q_{tttt} - 2i|q|^2q_t^2q^* - 4i|q|^4q_{tt} \\
&-4iq|q|^2|q_t|^2 - 2i|q|^6q + 2iq\left(\frac{1}{4}|q_{tt}|^2 + \frac{1}{2}|q|^2qq_{tt}^* + \frac{1}{2}|q|^2q^*q_{tt} + |q|^6\right) - i\frac{1}{4}q^2q_{tttt}^* \\
&-iq^3\left(q_t^*\right)^2 - 2iq^2|q|^2q_{tt}^* - 2i|q|^2q|q_t|^2 - i|q|^6q, \\
= \;& -i\left[\frac{1}{8}q_{tttttt} + \frac{5}{2}q^*q_{tt}^2 + 3q^*q_tq_{ttt} + 7|q_t|^2q_{tt} + \frac{5}{2}q_t^2q_{tt}^* + 2q|q_{tt}|^2 + 3qq_t^*q_{ttt} + qq_tq_{ttt}^* + |q|^6q\right. \\
&\left.+5|q|^2q^*q_t^2 + \frac{11}{2}|q|^4q_{tt} + \frac{3}{2}|q|^2q_{tttt} + 12|q|^2q|q_t|^2 + 2q^3\left(q_t^*\right)^2 + |q|^2q^2q_{tt}^* + \frac{1}{4}q^2q_{tttt}^*\right].
\end{aligned}
$$

A.6 Numerical Error of the split-step Fourier algorithm

Let $\hat{D}(\Delta z)q = \exp[i(\Delta z/2)\partial^2/\partial t^2]q$ and $\hat{N}(\Delta z)q = \exp(i\Delta z|q|^2)q$. By expanding the exponential series, $\exp(x) = 1 + x + x^2/2! + \cdots$, we have

$$
\exp\left[i\left(\frac{\Delta z}{4}\right)\frac{\partial^2}{\partial t^2}\right]q = q + i\frac{\Delta z}{4}q_{tt} - \frac{(\Delta z)^2}{32}q_{tttt} - i\frac{(\Delta z)^3}{384}q_{tttttt} + \cdots.
$$

Let $\breve{q} = \exp(\Delta z\hat{D}/2)q$. So, $\hat{N}(\Delta z)\hat{D}(\Delta z/2)$ becomes $\exp(i\Delta z|\breve{q}|^2)\breve{q}$, where

$$
\exp(i\Delta z|\breve{q}|^2)\breve{q} = \left[1 + i\Delta z|\breve{q}|^2 - \frac{(\Delta z)^2}{2!}|\breve{q}|^4 - i\frac{(\Delta z)^3}{3!}|\breve{q}|^8 + \cdots\right]\breve{q}.
$$

$$
\begin{aligned}
|\breve{q}|^2 &= |q|^2 - i\frac{\Delta z}{4}qq_{tt}^* - \frac{(\Delta z)^2}{32}qq_{tttt}^* + i\frac{(\Delta z)^3}{384}qq_{tttttt}^* + i\frac{\Delta z}{4}q^*q_{tt} + \frac{(\Delta z)^2}{16}|q_{tt}|^2 \\
&\quad -i\frac{(\Delta z)^3}{128}q_{tt}q_{tttt}^* - \frac{(\Delta z)^2}{32}q^*q_{tttt} + i\frac{(\Delta z)^3}{128}q_{tt}^*q_{tttt} - i\frac{(\Delta z)^3}{384}q^*q_{tttttt} + \cdots. \\
|\breve{q}|^2\breve{q} &= |q|^2q - i\frac{\Delta z}{4}q^2q_{tt}^* - \frac{(\Delta z)^2}{32}q^2q_{tttt}^* + i\frac{\Delta z}{2}|q|^2q_{tt} + \frac{(\Delta z)^2}{8}q|q_{tt}|^2 - \frac{(\Delta z)^2}{16}|q|^2q_{tttt} \\
&\quad -\frac{(\Delta z)^2}{16}q^*q_{tt}^2 + \cdots. \\
|\breve{q}|^4\breve{q} &= |q|^4q - i\frac{\Delta z}{2}q^2|q|^2q_{tt}^* + i\frac{3\Delta z}{4}|q|^4q_{tt} + \cdots. \\
|\breve{q}|^8\breve{q} &= |q|^8q + \cdots.
\end{aligned}
$$

By substituting $|\breve{q}|^2\breve{q}$, $|\breve{q}|^4\breve{q}$, and $|\breve{q}|^8\breve{q}$, we have

$$\begin{aligned}
\exp(i\Delta z|\breve{q}|^2)\breve{q} &= q + i\Delta z\left(|q|^2 q + \frac{1}{4}q_{tt}\right) - (\Delta z)^2\left(\frac{1}{32}q_{tttt} + \frac{1}{2}q_{tt}|q|^2 - \frac{1}{4}q_{tt}^* q^2 + \frac{1}{2}|q|^4 q\right) \\
&\quad + i(\Delta z)^3\left(-\frac{1}{384}q_{tttttt} - \frac{1}{32}q^2 q_{tttt}^* + \frac{1}{8}q|q_{tt}|^2 - \frac{1}{16}|q|^2 q_{tttt} - \frac{1}{16}q^* q_{tt}^2\right. \\
&\quad \left. + \frac{1}{4}q^2|q|^2 q_{tt}^* - \frac{3}{8}|q|^4 q_{tt} - \frac{1}{6}|q|^8 q\right) + \cdots.
\end{aligned}$$

Let $\grave{q} = \hat{N}(\Delta z)\hat{D}(\Delta z/2)q$. Then,

$$\begin{aligned}
\hat{D}(\Delta z/2)\grave{q} &= \left[1 + \frac{\Delta z}{2}\left(\frac{i}{2}\right)\frac{\partial^2}{\partial t^2} + \left(\frac{\Delta z}{2}\right)^2 \frac{1}{2!}\left(\frac{i}{2}\right)^2 \frac{\partial^4}{\partial t^4} + \left(\frac{\Delta z}{2}\right)^3 \frac{1}{3!}\left(\frac{i}{2}\right)^3 \frac{\partial^6}{\partial t^6}\right]\grave{q} + \cdots. \\
\grave{q}_t &= q_t + i\Delta z\left(\frac{1}{4}q_{ttt} + 2|q|^2 q_t + q^2 q_t^*\right) + (\Delta z)^2 \Big[-\frac{1}{32}q_{ttttt} \\
&\quad + \frac{1}{2}q q_t q_{tt}^* + \frac{1}{4}q^2 q_{ttt}^* - \frac{1}{2}q_t q^* q_{tt} - \frac{1}{2}q q_t^* q_{tt} - \frac{1}{2}|q|^2 q_{ttt} - \frac{3}{2}|q|^4 q_t \\
&\quad - |q|^2 q^2 q_t^* \Big) + \cdots. \\
\grave{q}_{tt} &= q_{tt} + i\Delta z\left(\frac{1}{4}q_{tttt} + 2q_t^2 q^* + 4q|q_t|^2 + 2|q|^2 q_{tt} + q^2 q_{tt}^*\right) \\
&\quad + (\Delta z)^2 \Big(-\frac{1}{32}q_{tttttt} + \frac{1}{2}q_t^2 q_{tt}^* + q q_t q_{ttt}^* + \frac{1}{4}q^2 q_{tttt}^* - \frac{1}{2}q^* q_{tt}^2 - |q_t|^2 q_{tt} \\
&\quad - q^* q_t q_{ttt} - q q_t^* q_{ttt} - \frac{1}{2}|q|^2 q_{tttt} - 3|q|^2 q^* q_t^2 - 6|q|^2 q|q_t|^2 - \frac{3}{2}|q|^4 q_{tt} \\
&\quad - q^3(q_t^*)^2 - |q|^2 q^2 q_{tt}^* \Big] + \cdots. \\
\grave{q}_{ttt} &= q_{ttt} + i\Delta z\Big(\frac{1}{4}q_{ttttt} + 6q^* q_t q_{tt} + 6q_t|q_t|^2 + 6q q_t^* q_{tt} + 6q q_t q_{tt}^* + 2|q|^2 q_{ttt} \\
&\quad + q^2 q_{ttt}^*\Big) + \cdots. \\
\grave{q}_{tttt} &= q_{tttt} + i\Delta z\Big(\frac{1}{4}q_{tttttt} + 24|q_t|^2 q_{tt} + 6q^* q_{tt}^2 + 8q^* q_t q_{ttt} + 12q_t^2 q_{tt}^* + 12q|q_{tt}|^2 \\
&\quad + 8q q_t^* q_{ttt} + 8q q_t q_{ttt}^* + 2|q|^2 q_{tttt} + q^2 q_{tttt}^*\Big) + \cdots. \\
\grave{q}_{tttttt} &= q_{tttttt}.
\end{aligned}$$

By substituting $\grave{q}$, $\grave{q}_{tt}$, $\grave{q}_{tttt}$, and $\grave{q}_{tttttt}$, the solution of the split-step Fourier method for propagation of one step Δz is

$$\hat{D}(\Delta z/2)\grave{q} = q + i\Delta z\left(|q|^2 q + \frac{1}{2}q_{tt}\right) - (\Delta z)^2\left(\frac{1}{8}q_{tttt} + |q|^2 q_{tt} + |q_t|^2 q + \frac{1}{2}q_t^2 q^* + \frac{1}{2}|q|^4 q\right)$$

$$-i(\Delta z)^3\left[\frac{1}{48}q_{tttttt}+\frac{1}{4}q|q_{tt}|^2+\frac{1}{4}|q|^2q_{tttt}+\frac{3}{8}q^*q_{tt}^2+\frac{3}{4}|q|^4q_{tt}+\frac{1}{6}|q|^8q\right.$$
$$+\frac{1}{4}q_t^2q_{tt}^*+|q_t|^2q_{tt}+\frac{1}{2}q^*q_tq_{ttt}+\frac{1}{2}qq_t^*q_{ttt}+\frac{3}{4}|q|^2q^*q_t^2+\frac{3}{2}|q|^2q|q_t|^2$$
$$\left.+\frac{1}{4}q^3(q_t^*)^2\right]+\cdots.$$

A.7 Procedures to obtain the local error at Δz^3 of a fundamental solution of NLS

The followings are the procedures in Maple V (Release 4). By substituting the results of q_t, q_{tt}, q_{ttt}, and q_{tttt} into Eq. (1.13). We can plot the coefficient of the $(\Delta z)^3$ term for $q(t) = \mathrm{sech}(t)$.

```
> restart;
```

```
> q:=sech(t);
```

$$q := \mathrm{sech}(t)$$

```
> qt:=diff(q,t);
```

$$qt := -\mathrm{sech}(t)\tanh(t)$$

```
> qtt:=diff(qt,t);
```

$$qtt := \mathrm{sech}(t)\tanh(t)^2 - \mathrm{sech}(t)\,(1-\tanh(t)^2)$$

```
> qttt:=diff(qtt,t);
```

$$qttt := -\mathrm{sech}(t)\tanh(t)^3 + 5\,\mathrm{sech}(t)\tanh(t)\,(1-\tanh(t)^2)$$

```
> qttt:=diff(qttt,t);
```

$$qttt := \mathrm{sech}(t)\tanh(t)^4 - 18\,\mathrm{sech}(t)\tanh(t)^2\,(1-\tanh(t)^2) + 5\,\mathrm{sech}(t)\,(1-\tanh(t)^2)^2$$

```
> qttt:=diff(qtt,t);
```

$$qttt := -\mathrm{sech}(t)\tanh(t)^3 + 5\,\mathrm{sech}(t)\tanh(t)\,(1-\tanh(t)^2)$$

```
> qtttt:=diff(qttt,t);
```

$$qtttt := \mathrm{sech}(t)\tanh(t)^4 - 18\,\mathrm{sech}(t)\tanh(t)^2\,(1-\tanh(t)^2) + 5\,\mathrm{sech}(t)\,(1-\tanh(t)^2)^2$$

```
> err:=I*(-(1/6)*(qt^2)*qtt-(1/12)*q*qtt*qtt-(1/24)*q*qtt*qtt
>       -(1/6)*qt*qt*qtt-(1/6)*q*qt*qttt-(1/24)*q*q*qtttt-(1/6)*(q^4)*qtt
>       -(1/2)*(q^3)*qt*qt-(1/12)*(q^3)*qt*qt-(1/6)*(q^4)*qtt
>       -(1/12)*(q^3)*qt*qt-(1/6)*(q^7)+(1/6)*(q^9));
```

$$\begin{aligned}
err := I(&-\frac{1}{3}\operatorname{sech}(t)^2\tanh(t)^2\,\%1 - \frac{1}{8}\operatorname{sech}(t)\,\%1^2\\
&+\frac{1}{6}\operatorname{sech}(t)^2\tanh(t)\,(-\operatorname{sech}(t)\tanh(t)^3 + 5\operatorname{sech}(t)\tanh(t)\,(1-\tanh(t)^2)) -\\
&\frac{1}{24}\operatorname{sech}(t)^2\,(\operatorname{sech}(t)\tanh(t)^4 - 18\operatorname{sech}(t)\tanh(t)^2\,(1-\tanh(t)^2) + 5\operatorname{sech}(t)\,(1-\tanh(t)^2)^2)\\
&-\frac{1}{3}\operatorname{sech}(t)^4\,\%1 - \frac{2}{3}\operatorname{sech}(t)^5\tanh(t)^2 - \frac{1}{6}\operatorname{sech}(t)^7 + \frac{1}{6}\operatorname{sech}(t)^9)\\
&\%1 := \operatorname{sech}(t)\tanh(t)^2 - \operatorname{sech}(t)\,(1-\tanh(t)^2)
\end{aligned}$$

```
> p:=plot(abs(err),t=-5..5):
```

A.8 Solution of the couple mode equations for uniform Bragg gratings

From Eq. (3.1), we set $d\phi(z)/dz = 0$ for gratings with constant period,

$$\begin{aligned}
S &= \left(\frac{1}{i\kappa_{\mathrm{ac}}}\right)\frac{dR}{dz} - \left(\frac{1}{\kappa_{\mathrm{ac}}}\right)\left[\kappa_{\mathrm{dc}} + \frac{1}{2}(\Delta\beta)\right]R, \\
\frac{dS}{dz} &= \left(\frac{1}{i\kappa_{\mathrm{ac}}}\right)\frac{d^2R}{dz^2} - \left(\frac{1}{\kappa_{\mathrm{ac}}}\right)\left[\kappa_{\mathrm{dc}} + \frac{1}{2}(\Delta\beta)\right]\frac{dR}{dz}.
\end{aligned} \tag{A.5}$$

Substitution of Eq. (A.5) into Eq. (3.2), we have

$$\frac{d^2R}{dz^2} + \left[\left(\kappa_{\mathrm{dc}} + \frac{\Delta\beta}{2}\right)^2 - |\kappa_{\mathrm{ac}}|^2\right]R = 0. \tag{A.6}$$

Let $\exp(\lambda z)$ be a solution of Eq. (A.6) and given that $\delta = \kappa_{\mathrm{dc}} + (1/2)[\Delta\beta - d\phi(z)/dz]$.

$$\begin{aligned}
\lambda^2 + \left[\left(\kappa_{\mathrm{dc}} + \frac{\Delta\beta}{2}\right)^2 - |\kappa_{\mathrm{ac}}|^2\right] &= 0, \\
\lambda^2 &= |\kappa_{\mathrm{ac}}|^2 - \delta^2, \\
\lambda_{1,2} &= \pm\sqrt{|\kappa_{\mathrm{ac}}|^2 - \delta^2}.
\end{aligned}$$

Let $\alpha = \sqrt{|\kappa_{\mathrm{ac}}|^2 - \delta^2}$. The general solution of $R(z)$ is :

$$\begin{aligned} R(z) &= C_1 \exp(\lambda_1 z) + C_2 \exp(\lambda_2 z), \\ &= C_1 \exp(\alpha z) + C_2 \exp(-\alpha z). \end{aligned}$$

Substitution of $R(z)$ into Eq. (A.5), we have

$$\begin{aligned} S &= \left(\frac{1}{i\kappa_{\mathrm{ac}}}\right)\left[C_1 \alpha \exp(\alpha z) - C_2 \alpha \exp(-\alpha z)\right] - \left(\frac{1}{\kappa_{\mathrm{ac}}}\right)\left(\kappa_{\mathrm{dc}} + \frac{\Delta\beta}{2}\right)\left[C_1 \exp(\alpha z)\right. \\ &\quad \left. + C_2 \exp(-\alpha z)\right], \\ &= \left[\left(\frac{-i\alpha}{\kappa_{\mathrm{ac}}}\right)\exp(\alpha z) - \left(\frac{\delta}{\kappa_{\mathrm{ac}}}\right)\exp(\alpha z)\right] C_1 - \left[\left(\frac{-i\alpha}{\kappa_{\mathrm{ac}}}\right)\exp(-\alpha z) + \left(\frac{\delta}{\kappa_{\mathrm{ac}}}\right)\exp(-\alpha z)\right] C_2. \end{aligned}$$

At $z = L$, the equations become

$$\begin{aligned} \begin{pmatrix} R(L) \\ S(L) \end{pmatrix} &= \begin{pmatrix} \exp(\alpha L) & \exp(-\alpha L) \\ \left[-i\alpha \exp(\alpha L) - \delta \exp(\alpha L)\right]/\kappa_{\mathrm{ac}} & -\left[-i\alpha \exp(-\alpha L) + \delta \exp(-\alpha L)\right]/\kappa_{\mathrm{ac}} \end{pmatrix} \\ &\quad \times \begin{pmatrix} C_1 \\ C_2 \end{pmatrix}, \end{aligned}$$

$$\begin{aligned} \begin{pmatrix} C_1 \\ C_2 \end{pmatrix} &= \begin{pmatrix} \exp(\alpha L) & \exp(-\alpha L) \\ \left[-i\alpha \exp(\alpha L) - \delta \exp(\alpha L)\right]/\kappa_{\mathrm{ac}} & -\left[-i\alpha \exp(-\alpha L) + \delta \exp(-\alpha L)\right]/\kappa_{\mathrm{ac}} \end{pmatrix}^{-1} \\ &\quad \times \begin{pmatrix} R(L) \\ S(L) \end{pmatrix}. \end{aligned}$$

At $z = 0$, we have

$$\begin{aligned} \begin{pmatrix} R(0) \\ S(0) \end{pmatrix} &= \begin{pmatrix} 1 & 1 \\ (-i\alpha - \delta)/\kappa_{\mathrm{ac}} & -(-i\alpha + \delta)/\kappa_{\mathrm{ac}} \end{pmatrix} \begin{pmatrix} C_1 \\ C_2 \end{pmatrix}, \\ &= \begin{pmatrix} 1 & 1 \\ (-i\alpha - \delta)/\kappa_{\mathrm{ac}} & -(-i\alpha + \delta)/\kappa_{\mathrm{ac}} \end{pmatrix} \times \end{aligned}$$

$$\begin{pmatrix} \exp(\alpha L) & \exp(-\alpha L) \\ \left[-i\alpha\exp(\alpha L) - \delta\exp(\alpha L)\right]/\kappa_{\mathrm{ac}} & -\left[-i\alpha\exp(-\alpha L) + \delta\exp(-\alpha L)\right]/\kappa_{\mathrm{ac}} \end{pmatrix}^{-1}$$

$$\times \begin{pmatrix} R(L) \\ S(L) \end{pmatrix}.$$

Therefore, the transfer matrix $[T]$ in Eq. (3.7) is :

$$\begin{aligned} [T] &= \left(\frac{\kappa_{\mathrm{ac}}}{2i\alpha}\right) \begin{pmatrix} 1 & 1 \\ (-i\alpha - \delta)/\kappa_{\mathrm{ac}} & -(-i\alpha + \delta)/\kappa_{\mathrm{ac}} \end{pmatrix} \\ &\quad \times \begin{pmatrix} -\left[-i\alpha\exp(-\alpha L) + \delta\exp(-\alpha L)\right]/\kappa_{\mathrm{ac}} & -\exp(-\alpha L) \\ \left[i\alpha\exp(\alpha L) + \delta\exp(\alpha L)\right]/\kappa_{\mathrm{ac}} & \exp(\alpha L) \end{pmatrix}, \\ &= \begin{bmatrix} T_{11} & T_{12} \\ T_{21} & T_{22} \end{bmatrix}, \end{aligned}$$

where

$$\begin{aligned} T_{11} &= \frac{\exp(-\alpha L) + \exp(\alpha L)}{2} - \left(\frac{i\delta}{\alpha}\right)\left[\frac{\exp(\alpha L) - \exp(-\alpha L)}{2}\right], \\ &= \cosh(\alpha L) - i\delta\sinh(\alpha L)/\alpha. \\ T_{12} &= \left(\frac{-\kappa_{\mathrm{ac}}}{2i\alpha}\right)\left[-\exp(-\alpha L) + \exp(\alpha L)\right], \\ &= -i\kappa_{\mathrm{ac}}\sinh(\alpha L)/\alpha. \\ T_{21} &= \left(\frac{1}{2i\alpha\kappa_{\mathrm{ac}}}\right)\{(i\alpha + \delta)\left[-i\alpha\exp(-\alpha L) + \delta\exp(-\alpha L)\right] + (i\alpha - \delta)\left[i\alpha\exp(\alpha L) + \right. \\ &\quad \left. \delta\exp(\alpha L)\right]\}, \\ &= i\left(\frac{\alpha^2 + \delta^2}{\alpha\kappa_{\mathrm{ac}}}\right)\sinh(\alpha L), \\ &= i\kappa_{\mathrm{ac}}^{*}\sinh(\alpha L)/\alpha. \\ T_{22} &= \left(\frac{1}{2i\alpha}\right)\left[\delta\exp(-\alpha L) + i\alpha\exp(-\alpha L) + i\alpha\exp(\alpha L) - \delta\exp(\alpha L)\right], \\ &= \cosh(\alpha L) + i\delta\sinh(\alpha L)/\alpha. \end{aligned}$$

A.9 Concatenation of two uniform Bragg gratings

Assume that a uniform Bragg grating has two sections with length z_1 and z_2, where $z_1 \neq z_2$. Let $[T_1]$, $[T_2]$, and $[T]$ be the transfer matrices of first section, second section, and the whole grating respectively.

$$\begin{bmatrix} R(0) \\ S(0) \end{bmatrix} = [T_1] \begin{bmatrix} R(z_1) \\ S(z_1) \end{bmatrix},$$

$$\begin{bmatrix} R(z_1) \\ S(z_1) \end{bmatrix} = [T_2] \begin{bmatrix} R(z) \\ S(z) \end{bmatrix},$$

$$\begin{bmatrix} R(0) \\ S(0) \end{bmatrix} = [T_1]\,[T_2] \begin{bmatrix} R(z) \\ S(z) \end{bmatrix}.$$

$$\begin{aligned} [T_1]\,[T_2] &= \begin{bmatrix} \cosh(\alpha z_1) - i\delta\sinh(\alpha z_1)/\alpha & -i\kappa_{\mathrm{ac}}\sinh(\alpha z_1)/\alpha \\ i\kappa_{\mathrm{ac}}^{*}\sinh(\alpha z_1)/\alpha & \cosh(\alpha z_1) + i\delta\sinh(\alpha z_1)/\alpha \end{bmatrix} \\ &\times \begin{bmatrix} \cosh(\alpha z_2) - i\delta\sinh(\alpha z_2)/\alpha & -i\kappa_{\mathrm{ac}}\sinh(\alpha z_2)/\alpha \\ i\kappa_{\mathrm{ac}}^{*}\sinh(\alpha z_2)/\alpha & \cosh(\alpha z_2) + i\delta\sinh(\alpha z_2)/\alpha \end{bmatrix}. \end{aligned}$$

Because,

$$\begin{aligned} T_{11} &= \cosh(\alpha z_1)\cosh(\alpha z_2) + \sinh(\alpha z_1)\sinh(\alpha z_2) - i(\delta/\alpha)[\sinh(\alpha z_1)\cosh(\alpha z_2) \\ &\quad + \sinh(\alpha z_2)\cosh(\alpha z_1)], \\ &= \cosh[\alpha(z_1+z_2)] - i\delta\sinh[\alpha(z_1+z_2)]/\alpha. \\ T_{12} &= (-\kappa_{\mathrm{ac}}/\alpha)[i\sinh(\alpha z_2)\cosh(\alpha z_1) + \delta\sinh(\alpha z_1)\sinh(\alpha z_2)/\alpha + i\sinh(\alpha z_1)\cosh(\alpha z_2) \\ &\quad -\delta\sinh(\alpha z_1)\sinh(\alpha z_2)/\alpha], \\ &= -i\kappa_{\mathrm{ac}}\sinh[\alpha(z_1+z_2)]/\alpha. \\ T_{21} &= i\kappa_{\mathrm{ac}}^{*}[\sinh(\alpha z_1)\cosh(\alpha z_2) + \sinh(\alpha z_2)\cosh(\alpha z_1)]/\alpha, \end{aligned}$$

$$= i\kappa_{\mathrm{ac}}^{*} \sinh[\alpha(z_1 + z_2)]/\alpha.$$

$$\begin{aligned} T_{22} &= (|\kappa_{\mathrm{ac}}|^2 - \delta^2)[\sinh(\alpha z_1)\sinh(\alpha z_2) + \cosh(\alpha z_1)\cosh(\alpha z_2)]/\alpha^2 + i\delta[\sinh(\alpha z_1)\cosh(\alpha z_2) \\ &\quad + \cosh(\alpha z_1)\sinh(\alpha z_2)]/\alpha, \\ &= \cosh[\alpha(z_1 + z_2)] + i\delta \sinh[\alpha(z_1 + z_2)]/\alpha. \end{aligned}$$

Therefore, $[T_1]\,[T_2] = [T]$.

Bibliography

[1] Y. Yamada, S. I. Nakagawa, K. Takashina, T. Kawazawa, H. Taga, and K. Goto, "25 GHz spacing ultra-dense WDM transmission experiment of 1 Tb/s (100WDM × 10 Gb/s) over 7,300 km using non pre-chirped RZ format," *Electron. Lett.*, vol. 35, pp. 2212-2213 (1999)

[2] G. P. Agrawal, *Nonlinear fiber optics*, 2nd Ed., Academic Press, San Diego, Ch. 1-5 (1995)

[3] I. P. Kaminow and T. L. Koch, Eds, *Optical fiber Telecommunications IIIA*, Academic Press, San Diego, Ch. 6-8, 12 (1997)

[4] P. K. A. Wai, W. L. Kath, C. R. Menyuk, and J. W. Zhang, "Nonlinear polarization-mode dispersion in optical fibers with randomly varying birefringence," *J. Opt. Soc. Amer. B*, vol. 14, pp. 2967-2979 (1997)

[5] M. Shtaif and A. Mecozzi, "Study of the frequency autocorrelation of the differential group delay in fibers with polarization mode dispersion," *Opt. Lett.*, vol. 25, pp. 707-709 (2000)

[6] M. Shtaif, A. Mecozzi, M. Tur, and J. A. Nagel, "A compensator for the effects of high-order polarization mode dispersion in optical fibers," *IEEE Photon. Technol. Lett.*, vol. 12, pp. 434-436 (2000)

[7] M. Rochette, S. LaRochelle, P. Y. Cortes, M. Guy, and J. Lauzon, "Polarization mode dispersion compensation of chirped Bragg gratings used as chromatic dispersion compensators," *Electron. Lett.*, vol. 36, pp. 342-343 (2000)

[8] A. Hasegawa and F. D. Tapper, "Transmission of stationary nonlinear optical pulses in dispersive dielectric fibers. I. Anomalous dispersion," *App. Phys. Lett.*, vol. 23, pp. 142-144 (1973)

[9] N. J. Smith, F. M. Knox, N. J. Doran, K. J. Blow, and I. Bennion, "Enhanced power solitons in optical fibres with periodic dispersion management," *Electron. Lett.*, vol. 32, pp. 54-55 (1996)

[10] A. Hasegawa, S. Kumar, and Y. Kodama, "Reduction of collision-induced time jitters in dispersion-managed soliton transmission systems," *Opt. Lett.*, vol. 21, pp. 39-41 (1996)

[11] N. J. Doran, W. Forysiak, J. H. B. Nijhof, A. M. Niculae, and A. Berntson, "Remarkable features of DM solitons: implications for high speed and WDM systems," *New trends in optical soliton transmission systems : proceedings of the symposium held in Kyoto*, Japan, 18-21 November, pp. 303-316 (1997)

[12] J. N. Kutz and P. K. A. Wai, "Gordon-Haus timing jitter reduction in dispersion-managed soliton communications," *IEEE Photon. Technol. Lett.*, vol. 10, pp. 702-704 (1998)

[13] N. J. Smith, N. J. Doran, F. M. Knox, and W. Forysiak, "Energy-scaling characteristics of solitons in strongly dispersion-managed fibers," *Opt. Lett.*, vol. 21, pp. 1981-1983 (1996)

[14] J. H. B. Nijhof, N. J. Doran, W. Forysiak, and A. Berntson, "Energy enhancement of dispersion-managed solitons and WDM," *Electron. Lett.*, vol. 34, pp. 481-482 (1998)

[15] S. Chi, J. C. Dung, and S. C. Lin, "Energy enhancement of dispersion managed soliton transmission system using mostly normal dispersion fiber," *IEEE Photon. Technol. Lett.*, vol. 11, pp. 1605-1607 (1999)

[16] R. Kashyap, *Fiber Bragg gratings*, Academic Press, San Diego, Ch. 3-5, 7-8 (1999)

[17] S. K. Turitsyn and V. K. Mezentsev, "Chirped solitons with strong confinement in transmission links with in-line fiber Bragg gratings," *Opt. Lett.*, vol. 23, pp. 600-602 (1998)

[18] J. D. Ania-Castañón, P. García-Fernández, and J. M. Soto-Crespo, "Stable multi-soliton pulses in dispersion management with fiber Bragg gratings," *Opt. Lett.*, vol. 25, pp. 159-161 (2000)

[19] T. Imai, T. Komukai, and M. Nakazawa, "Second- and third-order dispersion compensation of picosecond pulses achieved by combining two nonlinearly chirped fiber Bragg gratings," *Electron. Lett.*, vol. 34, pp. 2422-2423 (1998)

[20] J. H. B. Nijhof, N. J. Doran, W. Forysiak, and F. M. Knox, "Stable soliton-like propagation in dispersion managed systems with net anomalous, zero and normal dispersion," *Electron. Lett.*, vol. 33, pp. 1726-1727 (1997)

[21] A. Berntson, N. J. Doran, W. Forysiak, and J. H. B. Nijhof, "Power dependence of dispersion-managed solitons for anomalous, zero, and normal path-average dispersion," *Opt. Lett.*, vol. 23, pp. 900-902 (1998)

[22] J. H. B. Nijhof, W. Forysiak, and N. J. Doran, "The averaging method for finding exactly periodic dispersion-managed solitons," *IEEE J. Selected Topics Quantum Electron.*, vol. 6, pp. 330-336 (2000)

[23] G. P. Agrawal, *Fiber-optic communication systems*, 2nd Ed., John Wiley & Sons, Inc., New York, Ch. 2, 7, 9-10 (1997)

[24] L. F. Mollenauer, R. H. Stolen, and J. P. Gordon, "Experimental observation of picosecond pulse narrowing and solitons in optical fibers," *Phys. Rev. Lett.*, vol. 45, pp. 1095-1098 (1980)

[25] V. E. Zakharov and A. B. Shabat, "Exact theory of two-dimensional self-focusing and one-dimentional self-modulation of waves in nonlinear media," *Sov. Phys. JETP*, vol. 34, pp. 62-69 (1972)

[26] E. Iannone, F. Matera, A. Mecozzi, and M. Settembre, *Nonlinear Optical Communication Networks*, John Wiley & Sons, Inc., New York, Ch. 5 (1998)

[27] L. F. Mollenauer, S. G. Evangelides, and J. P. Gordon, "WDM with solitons in ultra-long distance transmission using lumped amplifiers," *J. Lightwave Technol.*, vol. 9, pp. 362-367 (1991)

[28] K. Tajima, "Compensation of soliton broadening in nonlinear optical fibers with loss," *Opt. Lett.*, vol. 12, pp. 54-56 (1987)

[29] W. Forysiak, F. M. Knox, and N. J. Doran, "Average soliton propagation in periodically amplified systems with stepwise dispersion-profiled fiber," *Opt. Lett.*, vol. 19, pp. 174-176 (1994)

[30] E. Kolltveit, J. P. Hamaide, and O. Andouin, "Optimum two-step dispersion management in WDM soliton systems," *Electron. Lett.*, vol. 32, pp. 1858-1859 (1996)

[31] J. F. L. Devaney, W. Forysiak, A. M. Niculae, and N. J. Doran, "Soliton collisions in dispersion-managed WDM systems," *Opt. Lett.*, vol. 22, pp. 1695-1697 (1997)

[32] H. Sugahara, A. Maruta, and Y. Kodama, "Optimal allocation of amplifiers in a dispersion-managed line for a WDM soliton transmission system," *Opt. Lett.*, vol. 24, pp.145-147 (1999)

[33] E. A. Golovchenko, A. N. Pilipetskii, and C. R. Menyuk, "Collision-induced timing jitter reduction by periodic dispersion management in soliton WDM transmission," *Electron. Lett.*, vol. 33, pp. 735-737 (1997)

[34] L. F. Mollenauer, J. P. Gordon, and M. N. Islam, "Soliton propagation in long fibers with periodically compensated loss," *IEEE J. Quantum Electron.*, vol. 22, pp. 157-173 (1986)

[35] G. Vareille, F. Pitel, R. Uhel, G. Bassier, J. P. Collet, G. Bourret, and J. F. Marcerou, "340 Gb/s (34 × 10 Gb/s, 50 GHz spacing DWDM) straight line transmission over 6,380 km with full system implementation assessment," *Optical Fiber Communication Conference: technical digest*, San Diego, Feb. 21-26, 1999, PD18 (1999)

[36] J. P. Gordon and H. A. Haus, "Random walk of coherently amplified solitons in optical fiber transmission," *Opt. Lett.*, vol. 11, pp. 665-667 (1986)

[37] N. J. Smith, W. Forysiak, and N. J. Doran, "Reduced Gordon-Haus jitter due to enhanced power solitons in strongly dispersion managed systems," *Electron. Lett.*, vol. 32, pp. 2085-2086 (1996)

[38] J. N. Kutz and P. K. A. Wai, "Ideal amplifier spacing for reduction of Gordon-Haus jitter in dispersion-managed soliton communications", *Electron. Lett.*, vol. 34, pp. 522-523 (1998)

[39] G. Bosco, A. Carena, V. Curri, R. Gaudino, and P. Poggiolini, "Suppression of spurious tones in fiber system simulations based on the split-step method," *LEOS '99 IEEE Lasers and Electro-Optics Society 1999 12th Annual Meeting*, vol. 2, pp. 455-456 (1999)

[40] "Special Issue on Fiber Gratings, Photosensitivity, and Poling: special issue papers," *J. Lightwave Technol.*, vol. 15, pp. 1263-1512 (1997)

[41] N. Bergano and C. R. Davidson, "Wavelength division multiplexing in long-haul transmission systems," *J. Lightwave Technol.*, vol. 14, pp. 1299-1308 (1996)

[42] A. Othonos and K. Kalli, *Fiber Bragg gratings: fundamentals and applications in telecommunications and sensing*, Artech House, Boston, Ch. 6 (1999)

[43] L. D. Garrett, A. H. Gnauck, R. W. Tkach, B. Agogliati, L. Arcangeli, D. Scarano, V. Gusmeroli, C. Tosetti, G. D. Maio, and F. Forghieri, "Ultra-wideband WDM transmission using cascaded chirped fiber grating," *Optical Fiber Communication Conference: technical digest*, San Diego, Feb. 21-26, 1999, PD15 (1999)

[44] M. P. Rouard, "Etudes des proprietes optiques des lames metalliques tres minces," *Annal. Phys. II*, vol. 7, (1937)

[45] L. A. Weller-Brophy and D. G. Hall, "Analysis of waveguide gratings: application of Rouard's method," *J. Opt. Soc. Amer. B*, vol. 2, pp. 863-871 (1985)

[46] M. Yamada and K. Sakuda, "Analysis of almost-periodic distributed feedback slab waveguides via a fundamental matrix approach," *App. Opt.*, vol. 26, pp. 3474-3478 (1987)

[47] K. A. Winick, "Effective-index method and coupled-mode theory for almost-periodic waveguide gratings: a comparison," *App. Opt.*, vol. 31, pp. 757-764 (1992)

[48] T. Erdogan, "Fiber grating spectra,", *J. Lightwave Technol.*, vol. 15, pp. 1277-1294 (1997)

[49] D. Pastor, J. Capmany, D. Ortega, V. Tatay, and J. Martí, "Design of apodized linearly chirped fiber gratings for dispersion compensation," *J. Lightwave Technol.*, vol. 14, pp. 2581-2588 (1996)

[50] M. Durkin, M. Ibsen, M. J. Cole, and R. I. Laming, "1m long continuously-written fiber Bragg gratings for combined second- and third-order dispersion compensation," *Electron. Lett.*, vol. 33, pp. 1891-1893 (1997)

[51] S. G. Evangelides Jr., N. S. Bergano, and C. R. Davidson, "Intersymbol interference induced by delay ripples in fiber Bragg gratings," *Optical Fiber Communication Conference: Technical Digest*, San Diego, Feb. 21-26, 1999, vol. 4, pp. 5-7 (1999)

[52] C. Scheerer, C. Glingener, G. Fischer, M. Bohn, and W. Rosenkranz, "System impact of ripples in grating group delay," *International Conference on Transparent Optical Networks 1999*, Kielce, Poland, June 9-11, 1999, pp. 33-36 (1999)